UNIVERSITY OF TRENTO

Department of Industrial Engineering

Doctoral School in Materials, Mechatronics and Systems Engineering
XXXIII *Cycle*

Analysis of the in-Flight Performance of a Critical Space Mechanism

The LISA Pathfinder Release Mechanism

Supervisor:
Prof. Daniele Bortoluzzi

PhD Candidate:
Davide Vignotto

Co-Supervisor:
Prof. Francesco Biral

December 2021

Abstract

Gravitational waves detection is a challenging scientific objective, faced by scientist in the last 100 years, when Einstein theorized their existence. Despite multiple attempts, it was only in 2016 that the first observation of a gravitational wave was officially announced. The observation, worth a Nobel Prize, was made possible thanks to a worldwide collaboration of three large ground-based detectors.

When detecting gravitational waves from ground, the noisy environment limits the frequency bandwidth of the measurement. Thus, the type of cosmic events that are observable is also limited. For this reason, scientists are developing the first gravitational waves detector based in space, which is a much quieter environment, especially in the sub-Hertz bandwidth. The space-based detector is named laser interferometer space antenna (LISA) and its launch is planned for 2034. Due to the extreme complexity of the mission, involving several new technologies, a demonstrator of LISA was launched and operated between 2015 and 2017.

The demonstrator mission, called LISA Pathfinder (LPF), had the objective to show the feasibility of the gravitational waves observation directly from space, by characterizing the noise affecting the relative acceleration of two free falling bodies in the milli-Hertz bandwidth. The mission was a success, proving the expected noise level is well below the minimum requirement.

The free-falling bodies of LPF, called test masses (TMs), were hosted inside dedicated electrode housings (EH), located approximately 30 cm apart inside the spacecraft. When free falling, each TM stays approximately in the center of the EH, thus having milli-meter wide gaps within the housing walls. Due to the presence of such large gaps, the TMs were mechanically constrained by dedicated mechanisms (named CVM and GPRM) in order to avoid damaging the payload during the launch phase and were released into free fall once the spacecraft was in orbit.

Prior to the start of the science phase, the injection procedure of the TMs into free-fall was started. Such a procedure brought each TM from being mechanically constrained to a state where it was electro-statically controlled in the center of the EH.

Surprisingly, the mechanical separation of the release mechanism from the TM caused unexpected residual velocities, which were not controllable by the electrostatic control force responsible for capturing the TM once released. Therefore, both the TMs collided with either the surrounding housing walls or the release mechanism end effectors. It was possible to start the science phase by manually controlling the release mechanism adopting non-nominal injection strategies, which should not be applicable in LISA, due to the larger time lag.

So, since any release mechanism malfunctioning may preclude the initialization of LISA science phase, the GPRM was extensively tested at the end of LPF, by means of a dedicated campaign of releases, involving several modifications to the nominal injection procedure. The data of the extended campaign are analyzed in this work and the main conclusion is that no optimal automated release strategy is found for the GPRM flight model as-built

configuration that works reliably for both the TMs producing a nominal injection procedure.
The analysis of the in-flight data is difficult since the gravitational reference sensor of LPF is not designed for such type of analysis. In particular, the low sampling frequency (i.e., 10 Hz) constitutes a limiting factor when detecting instantaneous events such as collisions of the TM.
Despite the difficulties of extracting useful information on the TM residual velocity from the in-flight data, it is found that the main cause of the uncontrollable state of the released TM is the collision of the TM with the plunger, i.e., one of the end-effectors of the GPRM. It is shown that the impact is caused by the oscillation of the plunger or by the elastic relaxation of the initial preload force that holds the TM. At the end of the analysis, some improvements to the design of the release mechanism are briefly discussed, aimed at maximizing the probability of performing a successful injection procedure for the six TMs that will be used as sensing bodies in the LISA experiment.

Contents

List of Abbreviations

AY	apparent yield
CAD	computer aided design
CCU	caging control unit
CI	confidence interval
CMS	charge management system
COM	center of mass
CVM	caging and vent mechanism
DE	dielectric elastomeric
DET	DE transducer
EH	electrode housing
EQM	engineering qualifying model
ESA	European space agency
FE	finite element
FEE	front-end electronic
FEM	finite element model
FM	flight model
GPRM	grabbing positioning and release mechanism
GRS	gravitational reference sensor
GW	gravitational waves
HW	hardware
IIS	internal interface structure
LISA	laser interferometer space antenna
LIGO	laser interferometer gravitational-wave observer
LPF	LISA Pathfinder
LTP	LISA technology package
PSD	power spectral density
QM	qualifying model
RF	reference frame
RSS	root square sum
SC	spacecraft
SNR	signal to noise ratio
TM	test mass

Chapter 1

Introduction

This thesis deals with the analysis of an electro-mechanical release mechanism developed for a space mission. As a starting point, this Chapter begins with an overview of the mission main goal, introducing the reader to the concept of gravitational waves detection. The Chapter continues with the description of the mission instrumentation which is closely related to the release mechanism focus of this manuscript.

1.1 Gravitational waves detection

The detection of gravitational waves (GWs) is an extremely challenging scientific objective. Physicists have been trying to observe such phenomena for decades. In fact, Albert Einstein published the *general theory of relativity* in 1916, in which he theorized the existence of gravitational waves, but the first direct observation of GWs was announced only in 2016, one hundred years after their theorization. According to Einstein's general relativity, what is commonly known as *gravity* is in fact a deformation of the space-time, the four-dimensional structure of the Universe. Such a deformation can travel through space-time in the form of a wave, propagating at the speed of light. GWs are defined as ripples in space-time, that are generated by cosmic processes, involving acceleration of large masses and huge amounts of energy. When a gravitational wave passes in a certain region of space, it affects the motion of the masses present in that region.
Gravitational waves exist in a wide range of frequencies, and each wave carries with it information on the source that generated it. For this reason, studying GWs allows the scientific community to obtain useful information about the nature of the Universe, information that cannot be gathered from the analysis of the light spectrum of cosmic objects, which is how the Universe was mainly studied so far.
The detection of gravitational waves is extremely difficult because they are generated by cosmic events many light-years away from Earth and they produce an extraordinarily small distortion of space-time once they get to the solar system. Scientists predicted that the differential motion of two masses on Earth, located kilometers apart from each other, produced by the passage of a GW is in the order of 10^{-19} m ([1]), which is comparable to the dimension of an electron.

The first indirect confirmation of the existence of gravitational waves was published in 1981, when astrophysicists Joseph Taylor, Joel Weisberg and Lee Fowler measured the rate at which the orbital period of a binary pair of neutron stars decreased and verified that it was in exact agreement with Einstein's predictions ([2]).

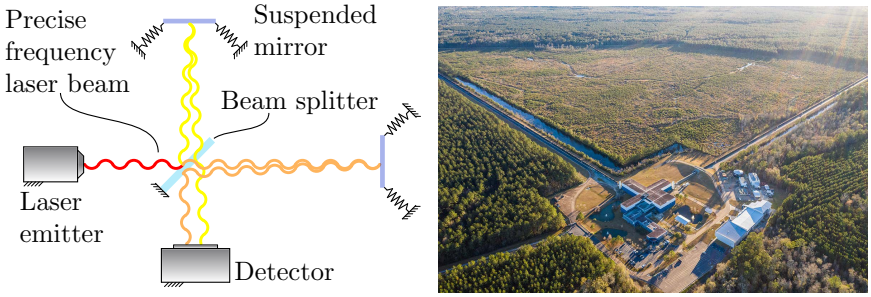

(a) (b)

Figure 1.1: On the left, schematic illustration of the Michelson interferometer. The laser beam (red) is divided into two different beams (yellow and orange), which are sent back to the detector thanks to two suspended mirrors. On the right, aerial photo of one of the two LIGO observers, in particular the one located in Livingston.

Since the 1960s, scientists built different kind of gravitational waves observers, located on ground, with the aim to obtain a direct measure of the GWs. The most recent observers are based on the Michelson interferometer ([3] and [4], see Figure 1.1a), where a highly stabilized laser beam is divided into two beams, following two different paths, namely the arms of the interferometer, and then sent back to a detector thanks to two mirrors. The gravitational measurement is possible by observing tiny changes in the relative phase of the two beams, since the passage of a GW affects the length of the arms.
In the most advanced GW detectors, the sensitivity is enhanced by adopting kilometer long arms, placed at a 90° angle, and using suspended (which means isolated from structure vibrations) mirrors. The advanced laser interferometer gravitational-wave observatory (Advanced LIGO, see Figure 1.1b) is composed of two large-scale (4 km arm-length) observatories based in the U.S. and nowadays is the most sensitive GW detector ever built. Using the Advanced LIGO, in collaboration with Virgo interferometer, based in Italy, scientists built a world-wide network of detectors. This collaboration led to the first direct measure of a gravitational wave in late 2015, that was officially announced in 2016 as previously mentioned.
One of the limiting factors affecting the sensitivity of the ground-based detectors is the presence of a relatively high background noise, due to the Earth environment. The utilization of widely separated detectors enhances the sensitivity, allowing the distinction of intrinsic noise transients, which are local, from the gravitational signal. The main noise sources are earthquakes, traffic and electrical storms and their presence limits the frequency bandwidth of the ground-based gravitational measurement to the 1×10^1 Hz to 1×10^3 Hz range approximately ([5]).
For this reason, physicists are developing new technologies to perform the first

gravitational waves measurement from space. Thanks to the outer space being a much less noisy environment with respect to Earth, it should be possible to build a detector which is capable of measuring GWs in the mHz range, thus widening the overall measurement range and increasing the number and typology of the detectable sources (see Figure 1.2).

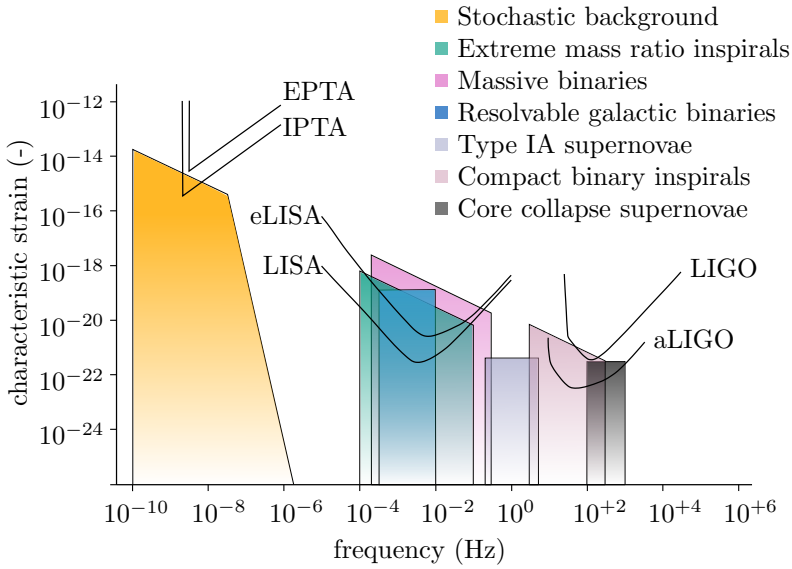

Figure 1.2: Expected characteristic strain on space-time structure produced by a gravitational wave as function of its frequency. GWs are grouped according to their sources. Ground based observers (on the right) are capable of measuring GWs from limited sources, while space-based observers (in the middle) will be able to detect GWs from more sources. Other experiments, the International and the European pulsar timing array (IPTA and EPTA), exploit the predictability of the time of arrival of pulses generated by millisecond pulsars to detect GWs ([6]).

To date, there is no space gravitational waves observatory, however for several years scientists have been developing what will be the first space-based GW detector, named laser interferometer space antenna (LISA, [7]), whose launch is scheduled for 2034. As the acronym suggests, LISA will still rely on the laser technology to perform the gravitational measurement. The main advantages with respect to ground-based detectors are the low-noise environment, as previously stated, and the absence of constraints on the maximum laser path length (interferometer arms), which are obviously present on Earth.
LISA mission is quite complex since it will be composed of three different spacecraft (SC) whose relative position and orientation need to be controlled and synchronized. The spacecraft will be located at the vertices of an equilateral triangle with approximately 2.5×10^6 km side-length, following the Earth along its orbit with a 20° offset. The sides of the triangle play the role of the arms in the Michelson interferometer. Laser beams will be used to measure the relative displacement of the spacecraft and the displacement of dedicated test masses (TMs), constituting

the sensing bodies of the experiment, relative to the hosting SC. Each satellite will contain two test masses, for a total of six (see Figure 1.3 for a schematic view of the LISA constellation). The TMs play the role of the suspended mirrors in the Michelson interferometer.
The test masses, during the science phase, are floating in a free fall state along the measurement direction inside the spacecraft, which acts as a shield for most of the external disturbances (such as galactic rays, charged particles and solar radiation pressure). According to Einstein's physical relativity theory, in the absence of noise, the free-falling test masses should follow a perfect geodesic trajectory. The concept of geodesic trajectory is the generalization of the notion of a"straight line" applied to the curved space-time, so it represents the trajectory that any mass follows when subjected only to gravitational forces.
LISA mission is quite ambitious, involving several complex mechanisms, whose correct functioning is pivotal to the start of the science phase, and having an incredibly strict requirement of approximately $3 \times 10^{-15}\,\mathrm{m\,s^{-2}\,Hz^{-1/2}}$ on the acceleration noise level affecting the TMs relative motion in the measurement bandwidth $1 \times 10^{-3}\,\mathrm{Hz}$ to $1 \times 10^{-2}\,\mathrm{Hz}$. To test many of the mechanisms that will be implemented in LISA, and to verify the feasibility of the gravitational measurement with the desired level of noise, a dedicated mission named LISA Pathfinder (LPF), precursor of LISA, was flown from 2015 to 2017.

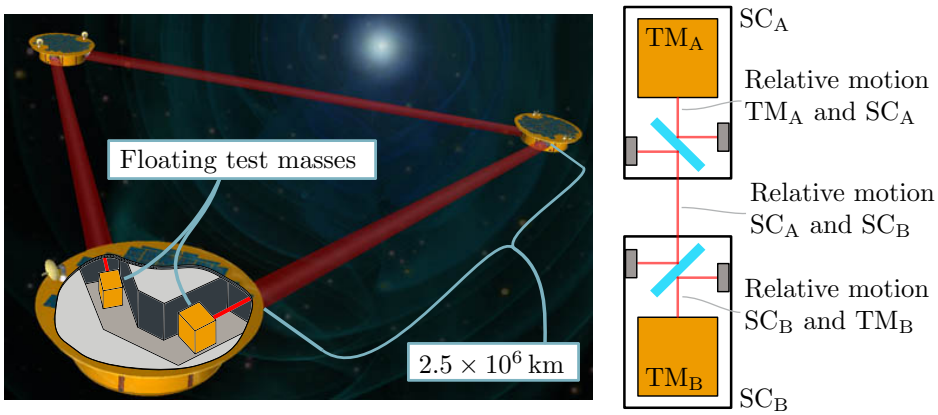

Figure 1.3: On the left, sketch of the LISA spacecraft deployed at the vertices of an equilateral triangle. The inside of one spacecraft is depicted, qualitatively, showing the test masses floating freely. On the right, scheme showing the laser beams used to measure I) the relative displacements of each TM with respect to the hosting spacecraft and II) the relative displacement between couples of spacecraft. Three decoupled interferometric measurements are performed to estimate the relative motion of two TMs.

1.2 LISA Pathfinder mission

LISA Pathfinder launch took place on the 3rd of December 2015, and the satellite remained operative until the 30th of June 2017. After a brief extended mission

phase, ended on the 18th of July 2017, the satellite transponder was switched off. LISA Pathfinder was a single spacecraft mission, representing a simplified version of LISA, but still allowing the scientists to open the path to the Gravitational Universe, returning important results and showing the feasibility of the gravitational measurement from space ([8] and [9]). It was developed to demonstrate the functioning of some key mechanisms that will be implemented in LISA, rather than directly measuring GWs. The key idea behind LPF development is to shrink one of the million kilometers long arms of LISA to approximately 30 cm, so that it can fit inside a single spacecraft. The LISA technology package (LTP), the technological core of the mission, included as its main component two gravitational reference sensors (GRSs) and an optical bench located in between (see Figures 1.4a and 1.4b).

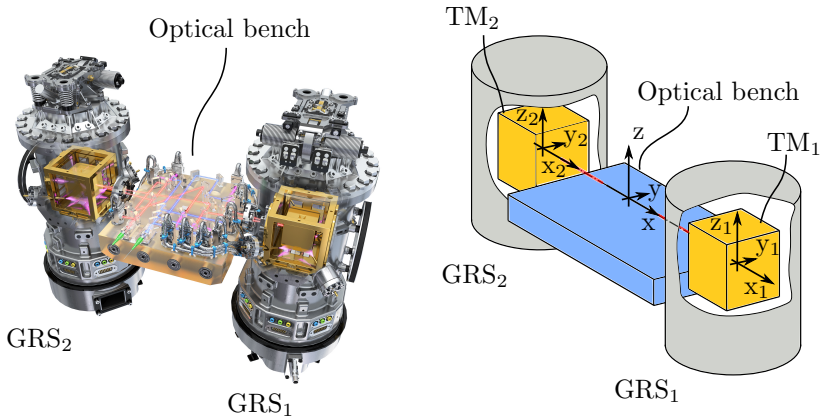

Figure 1.4: On the left, rendering of the LISA technology package. The optical bench for the laser is located in between the two GRSs, each one hosting a TM. On the right, schematic view of the LTP, where the main reference frames of the mission are depicted, showing that the laser measurement is taken along x-axis.

A laser beam traveled across the optical bench and was used to measure the relative acceleration of two free-floating TMs along one direction, similarly to how laser beams of LISA mission will work. The TMs, part of the GRSs, constitute the sensing bodies of the experiment. Apart from the TM, each GRS includes several components, such as the mechanisms and electronics needed to release the TM into free-fall (i.e., physically detach the TM from any other body) and to monitor its position and attitude. In LPF such operations were managed by the caging control unit (CCU), which elaborates the sensors information and was used to operate the GRS mechanisms. Details on the GRS will be discussed later in this Chapter, explaining its general working principle and describing some of the mechanisms it included.
The scientific requirement of LISA Pathfinder was to set the two TMs into a nearly pure free-fall state, so that the noise affecting their relative acceleration stayed below $3 \times 10^{-14}\,\mathrm{m\,s^{-2}\,Hz^{-1/2}}$ at 1 mHz, which corresponds to approximately one

order of magnitude relaxation with respect to the requirement set for LISA. As shown in Figure 1.5, the latest LPF results are well beyond expectations. After instrumentation calibration, the in-flight data analysis of the relative acceleration of the TMs shows that not only the main requirement was met, but also the 10 times more stringent requirement of LISA was fulfilled. Thus, the mission can unquestionably be considered a success, even if some problems had to be faced, especially during the injection of the test masses into free-fall, which is discussed in this work. Understanding what caused the mentioned problems during the TMs injection is extremely important in view of the forthcoming LISA mission, because the mechanisms involved in that phase will be used also in LISA, where six test masses need to be released into a geodesic. For a better comprehension of what happened in flight, an extensive description of the GRS and its main components will be presented in the following, along with the description of the steps of the procedure adopted to release the TMs into free-fall.

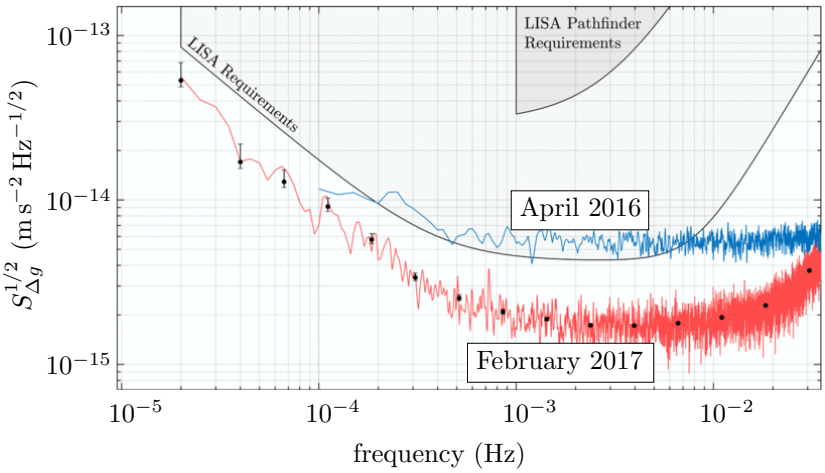

Figure 1.5: Residual relative acceleration of the two test masses on board of LISA Pathfinder spacecraft, in the frequency domain. Both curves (blue and red) widely fulfill the LPF requirement, dark grey shaded area, and the red curve also met the LISA requirement, light grey shaded area.

1.2.1 The GRS

The two gravitational reference sensors on board of LPF mission, named GRS_1 and GRS_2, are the technological cores of the LTP. Each GRS unit includes a dedicated TM (TM_1 and TM_2) along with several instrumentations, used mainly to monitor and to control the position of the TM during every phase of the mission. Each TM is a cubic shaped rigid body, made of a gold-platinum alloy, with a side-length of 46 mm and a weight of approximately 2 kg (details are reported in Table 1.1 and an image is shown in Figure 1.6a). The TM position and attitude are expressed in the GRS reference frame (RF), depicted in Figure 1.4b).
During the science phase, in order to perform the desired measurements, the TMs

are set into a free-fall state, i.e., their relative motion along x is affected by the gravitational force uniquely. The complex sequence of operations performed to set the TM into free-fall state is named injection procedure.

Table 1.1: Physical properties and geometrical details of the test mass, sensing body of the experiment on board of the LISA Pathfinder mission.

Param.	Value	Unit	Description
Material	73% Au - 23% Pt	(-)	Gold platinum alloy
Mass	1.98	kg	
Coating	1	µm	Gold and Titanium
Yield strength	186.8	MPa	
Tensile strength	334.7	MPa	
Young's modulus	107.0	MPa	
Poisson ratio	0.41	(-)	
Density	19 910.1	$kg\,m^{-3}$	
Volume	96 835.3	mm^3	
Geometry	(-)	(-)	Cubic-shaped
Dimension	46	mm	Side-length

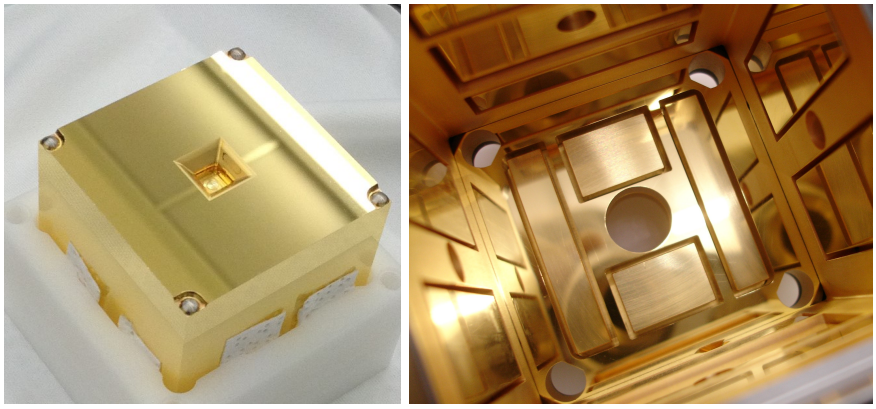

(a) (b)

Figure 1.6: On the left, photo of the flight model of LISA Pathfinder test mass during on-ground verifications. On the right, photo of the inner surfaces of the electrode housing of LISA Pathfinder. The holes necessary to accommodate release mechanism end effectors are visible. Every surface facing the TM is gold coated.

The electrode housing (EH), that hosts the TM, is basically a cubic-like box, slightly bigger than the TM, with 18 rectangular electrodes attached to its inner walls, facing the TM (see Figure 1.6b). Those electrodes are recessed by few hundred microns with respect to the EH envelope, to prevent damages due to undesired

impacts with the TM.

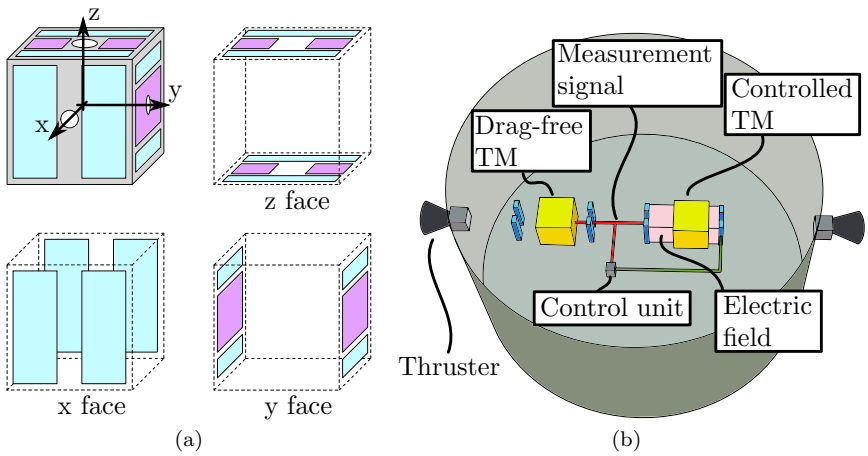

Figure 1.7: On the left, sketch of electrodes configuration attached to the EH chassis. Purple areas represent injection electrodes, cyan areas represent sensing electrodes. The configuration is symmetric along x, y and z directions. On the right, scheme showing the implementation of the drag free technology in LPF. Along the measurement direction, one TM is actually in drag-free state, the other is electro-statically suspended.

The electrodes configuration is represented in Figure 1.7a, showing that there are two types of electrodes, which are injection and sensing ones. The injection electrodes are used to inject a 100 kHz oscillating electrical voltage to the TM, so that its position and attitude can be estimated from the capacitance measurement provided by the sensing electrodes. The position and attitude of the TM measured with the EH electrodes, are used as an input for the drag-free control loop ([8]). The sensing electrodes are also used to generate the electrostatic forces that control the TM position and attitude. Electrodes are charged with a desired electric potential, so that an electrostatic force is generated, accelerating the TM. During the science phase, one of the TM is free-falling along x direction, while the other degrees of freedom (DOFs) are controlled with the electrostatic force. The second TM is electro-statically actuated on all its six DOFs, at low frequencies, in order to follow the first TM, as schematized in Figure 1.7b. To guarantee that the GRS and the drag-free technology are sufficiently precise, to fulfill the strict mission requirement, three main design choices were made. The first was to adopt a heavy TM (2 kg is among the heaviest floating mass ever released for an outer space experiment), since in physics any mass behaves like a low pass filter, as shown in Equation 1.1, which means that high frequency disturbance is filtered out.

$$m\ddot{x} = F \overset{\mathcal{L}}{\Rightarrow} ms^2\tilde{x} = \tilde{F} \Rightarrow \tilde{x} = \frac{1}{ms^2}\tilde{F} \tag{1.1}$$

where m is the mass, $\ddot{x}$ the second derivative of the position x over time, F is an external disturbance and $\mathcal{L}$ indicates the Laplace transform that goes from time

domain t to the complex domain s (the relation between the Laplace and the Fourier domains is $s = \iota\omega$, where ω represents the frequency). The transformed functions are distinguishable by a $\sim$ symbol on top.
The second strategy was to have large gaps between the TM and the surrounding walls, in the range from 3 mm to 4 mm approximately. This was done to minimize the effect of force noise sources such as out-gassing of the surfaces, or local electric fields due to non-ideal surface uniformity. The third strategy adopted was to gold-coat both the TM and any other surface that is directly facing it. Indeed, thanks to its excellent conductivity, gold is ideal to reduce the presence of electric charge patches on the surfaces, guaranteeing uniform electric fields are generated inside the EH.
The three design choices discussed present some drawbacks. Having a heavy TM, separated from the EH by large gaps, requires to mechanically constrain it with respect to the satellite chassis during non-science phases, to prevent any damage on the GRS due to undesired impacts of the TM with the surroundings. The combination of a heavy TM with large gaps makes LISA Pathfinder the mission with the higher impact coefficient ([10], see Figure 1.8), defined as the product of the mass by the available free motion distance, in the hypothesis that different launchers have roughly the same acceleration. This fact underlines why LPF is an important case of study in the frame of drag-free space missions. The heavier the TM, the greater the force required to lock it in place, and the greater will be the adhesion generated at the mechanical interfaces. Furthermore, with the TM gold coated, the adhesive bonds will be strong even at low contact pressure ([11]).

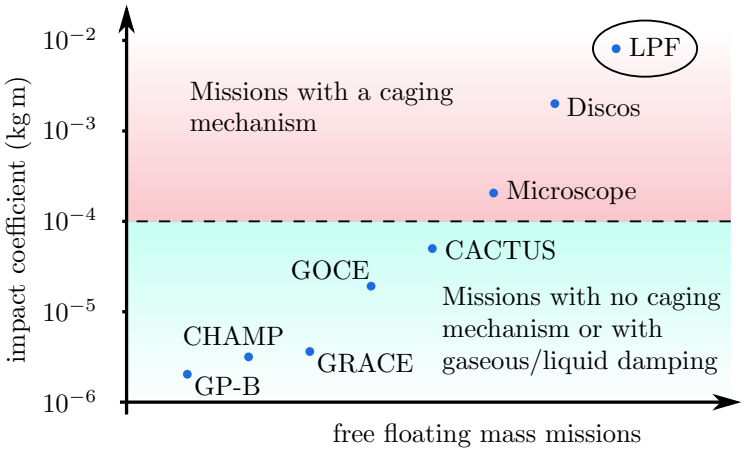

Figure 1.8: Impact coefficient for different space experiments based on free floating mass/masses, defined as the product of the free motion distance and the mass of the floating body ([10]). LISA Pathfinder is the mission with the highest coefficient so far. Above a threshold of approximately 1×10^{-4} kg m, a caging mechanism is required.

The large gaps between the TM and the EH walls present the drawback of limiting the control force authority since the force generated by an electrode is inversely

proportional to the square of the distance of the TM surface facing it. As a consequence, the maximum control force and torque are limited to the 1 µN and 1 pN m orders of magnitude (the torque exerted by a couple of electrodes is proportional to their distance, which is in the order of 3 cm)).
The limited control force authority carries with itself two more problems. The first problem is the fact that a static release of the TM is not possible, i.e., the control force is not sufficient to break the strong adhesive bonds. In fact, in [12] it is shown that for clean gold specimens the adhesive force is approximately 10 times greater than the contact load, which is in the order of 1 mN in LPF. This implies that the release of the TM must be performed dynamically, with a dedicated mechanism, exploiting its inertia to overcome the adhesive bonds.
The second problem is that the limited force/torque authority makes it necessary to introduce a strict requirement on the TM state once it has been released into free-fall, listed in Table 1.2. Such a requirement is introduced to guarantee that the limited authority electrostatic control force is capable of controlling and stabilizing the TM in the center of the EH, avoiding impacts with the surroundings, once the adhesive bonds have been broken.
For the listed reasons, the GRS is provided with two dedicated mechanisms that are responsible, respectively, for constraining the TM during the initial mission phases and for releasing it into free-fall fulfilling the mentioned requirement.

Table 1.2: Requirement defining the limits of the TM state at the release, imposed to guarantee that the limited authority electrostatic actuation force is capable of controlling and stabilizing it. Translations and rotations are expressed relatively to the GRS reference frame.

	Value	Unit
Translations	±200	µm
Rotations	±2000	µrad
Linear velocities	±5	$\mu m\,s^{-1}$
Angular velocities	±100	$\mu rad\,s^{-1}$

1.2.2 Caging and release mechanisms

As a consequence of the GRS design choices, the handling of the TM of LISA Pathfinder is an extremely challenging engineering problem. To summarize, when designing the mechanisms responsible for this task, the two main goals are the need of high forces to constrain the TM at launch and the necessity to release it with precise position/attitude and extremely low linear/angular velocities. Unfortunately, these two goals are in contradiction with each other. As already explained, having high caging forces creates strong adhesive bonds at any mechanical interface with the TM. As previous studies have shown ([13]), the adhesive force has a low repeatability, and with it being non negligible makes it difficult to accurately predict the release velocity of the TM. In fact, the low repeatability of the adhesion generates asymmetry between nominally equal and opposite contact surfaces, thus a net impulse proportional to the force difference may be transferred to the TM when the

contact is removed. Following these considerations, the design strategy adopted to meet the goals is based on performing the different functions separately, i.e., by independent mechanisms on different mechanical interfaces. Table 1.3 clearly depicts how the functions separation concept is applied to the LPF case. Two systems have been developed, the caging and vent mechanism (CVM) and the grabbing positioning and release mechanism (GPRM), the latter including as a sub-mechanism the actual release mechanism.

Table 1.3: Functions separation design for the LISA Pathfinder GRS. Two main mechanisms are involved in caging the TM, release it and eventually grab it again in case satellite safe mode is activated. On the right column, note the decreasing preload force on the TM as the release is approached ([14]).

Mechanism name	Main function	Mechanism interface	TM interface	Preload force
CVM	Caging the TM during launch and in-orbit phases	Eight cylindrical fingers	TM vertices, properly machined	$\approx 10^3$ N
GPRM	Grabbing the caged/floating TM and repositioning it in the center of the EH	Two coaxial pyramidal/conical plungers	Dedicated pyramidal indents in the centers of the TM −z and +z faces	≈1 N
	Releasing the TM into free-fall	Two small hemispherical-edged tips, protruding from the plunger heads	Two precisely machined flat circular surfaces at the bottom of the TM indents	$\approx 10^{-1}$ N

The CVM is responsible for locking the TM inside the EH from the assembly phase of the GRS, during the mission launch and until the in-orbit phase is reached. Other than firmly locking the TM, the venting function of the CVM consists in opening a vacuum valve, to expose the GRS to free space vacuum ([15]), although this is not discussed in this work.
Following design constraints are imposed on the CVM:

- structure able to lock the TM sustaining the launcher vibrations.
- no magnetic materials, in order to minimize electromagnetic disturbances.
- no liquid lubricants, to avoid possible contamination of the GRS instrumentations.
- single shot mechanism.

The CVM interacts with the TM through eight titanium cylinders (end effectors), parallel to the z axis of the GRS reference frame called caging fingers, that apply a preload force on the TM vertices in the order of 1×10^3 N. The TM vertices are properly machined in order to accommodate the finger heads, so that the TM is mechanically constrained along all its six DOFs (see Figure 1.9).

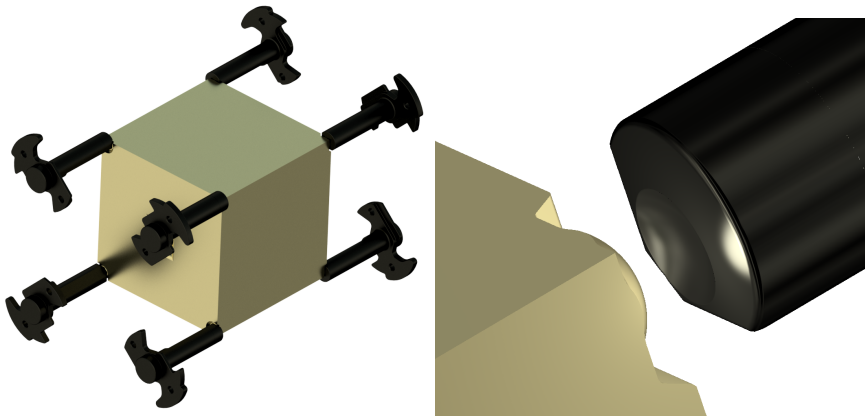

(a) (b)

Figure 1.9: On the left, rendering of the TM caged by the eight end effectors of the CVM (fingers) on its vertices. All the fingers are parallel to the z axis in the GRS reference frame. On the right, magnification around one of the TM vertices. A detached finger is rendered, to better show its geometry. TM vertices and finger heads are precisely machined on the respective mechanical interface.

The second mechanism, the GPRM, will be widely discussed in this thesis, since it plays an active role in the release of the TM. The main functions of the GPRM are the handling of the TM after the in-orbit phase and its actual release into free flight. Handling the TM means to grab it and to reposition it in the center of the electrode housing. Another important function of the GPRM, imposed by the mission requirements, is the re-grabbing of the free-falling TM from any position inside the EH, in case the spacecraft safe mode is activated. So, in contrast with the single shot design of the CVM, the GPRM can be used multiple times, to grab and release the TM whenever is required.
The GPRM is composed of two nearly identical units, located on the +z and −z sides of GRS reference frame. The two halves are referred to as top and bottom units (or up and down units), assuming the z axis is vertical (see Figure 1.10a). Each unit is a complicated mechanism, involving several parts and actuators. The chassis of the GPRM unit is firmly screwed to the internal interface structure (IIS) of the GRS, to which also the EH is firmly attached. The chassis presents a through hole, inside which is inserted a T-shaped component, called linear runner, with a squared cross section along z axis.
On the x−z plane, the linear runner is linked to the chassis by means of a slider/roller linear guide. The slide surface is ceramic coated, and the rollers are pushed against the linear runner thanks to a preloaded spring (see Figure 1.10b).

On the y−z plane the linear runner is kept in position by means of piezo-stacks towers. The piezo-stacks towers can be actuated so that they literally walk on the linear runner surface, moving it along the z axis. Such a mechanism is a custom version of the NEXLINE mechanism manufactured by Physik Instrumente (PI) GmbH & Co (see Figure 1.10c). The range of motion achieved is approximately 30 mm, with a precision in the order of 1 µm.

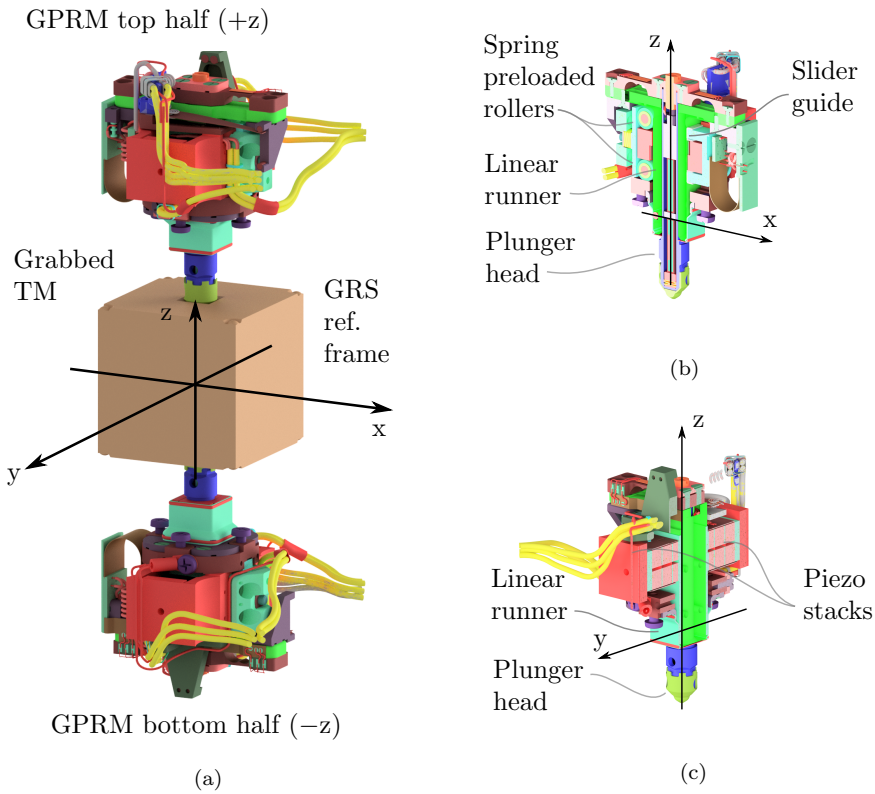

Figure 1.10: On the left, rendering of the two units of the GPRM grabbing the TM along z axis by means of the two plungers. The plunger heads fit in the dedicated indents present on the TM z faces. On the top-right, x−z section view of a single GPRM unit. The T-shaped linear runner (green) is held in position by means of a slider guide and two spring preloaded rollers. On the bottom-right, y−z section view of a single GPRM unit. The linear runner moves along z axis thanks to piezo stacks literally walking on its surface when commanded. Renderings are courtesy of RUAG.

A strain gauge displacement sensor is used to measure the position of the linear runner along the z axis. The sensor presents a dead zone in the middle of the plunger stroke. The T-shaped linear runner is drilled through in the center, along the z axis. Inside the hole, a cylindrical-shaped component, called plunger, is inserted. The plunger is long enough that its head protrudes outside of the envelope of the GPRM chassis, toward the inside of the EH. The plunger is linked to the

linear runner on two points along its main axis. On one side, the plunger is fixed to a deformable component provided with a Wheatstone bridge of strain gauges, used to measure the force acting on the plunger along z direction, and itself screwed to the linear runner. On the other side, approximately at 2/3 of its length, the plunger is kept in position by means of a thin plane, deformable along z direction and rigid along x and y directions (Figure 1.11a and Figure 1.11b).

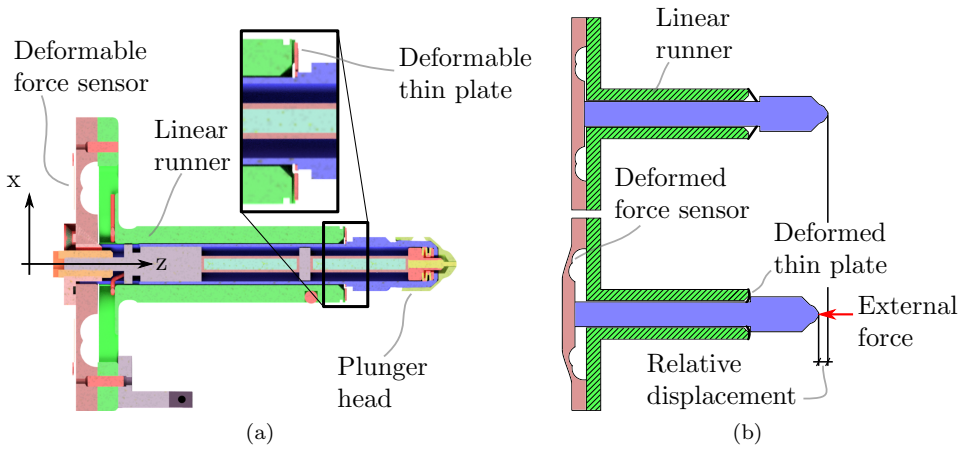

Figure 1.11: On the left, rendering of the section view of the linear runner and the relative plunger. The deformable structure used to measure the force and the thin plane holding the plunger are visible. On the right, sketch of the nominal mechanism deformation when the plunger is subjected to a force along z direction, not to scale.

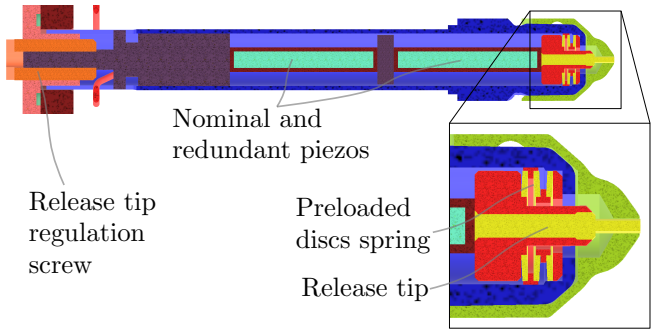

Figure 1.12: Rendering of the release sub-mechanism of a GPRM unit. Inside the plunger body (blue), a series of piezo stacks actuates the release tip along z direction. A discs spring maintains the system pre-loaded.

Inside the plunger, a series of two piezo stacks is inserted. The two piezo stacks are the actuators (one is the nominal, the other the redundant) of the sub-mechanism

responsible of the TM release (Figure 1.12). This sub-mechanism is composed by a small golden tip (end effector), sliding along z direction coaxially to the plunger. A preloaded discs spring pushes the tip onto the piezo stacks, which are used to move the tip with micro-metric precision relatively to the plunger. The tip protrudes from the plunger head, which is drilled in the center to accommodate it. According to the data sheet, the nominal maximum tip range of motion is very small, approximately 18 ± 3.6 µm. It is important to notice that both the plunger heads and the tips are made of gold alloy, a choice made to maximize the GRS performance reducing stray electric fields, as they directly face the TM.

1.2.3 The nominal release procedure

This section describes the sequence of steps performed in flight to release the TM, which is referred to as the nominal release procedure. The high preload force of the CVM makes it impossible to release the TM fulfilling the requirement of Table 1.2 by simply retracting the eight fingers. For this reason, from the end of the in-orbit mission phase, the handling of the TM is entrusted to the GPRM. The transition from the CVM to the GPRM is named pass-over. During the pass-over, the two linear runners of the GPRM are moved towards the TM, while it is locked in position by the fingers of the CVM. The linear runners, moved by means of the NEXLINE linear actuators, carry with them the respective plungers. The motion stops when the plunger heads fit into dedicated nearly pyramidal indents machined on the TM z faces (Figure 1.13a), with a preload of approximately 1 N. At this point, the eight end effectors of the CVM are retracted, so the TM is suspended by means of the two plunger heads, which are capable of locking all the six DOFs of the TM thanks to the form fit generated by the shape of their head.

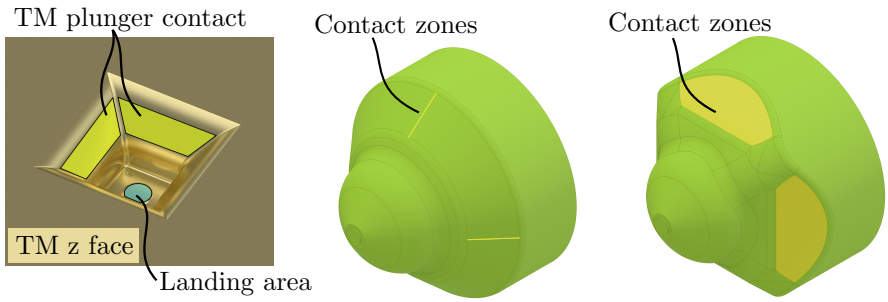

Figure 1.13: On the left, rendering of the indent geometry on the TM z faces, where plunger heads fit when the TM is grabbed. The surfaces working as interfaces with the plungers and the tip are highlighted in yellow and blue respectively. In the center and on the right, geometry of the plunger heads, conical (top/up) and pyramidal (bottom/down) respectively (images are taken from [14]). Nominal contact zones with the TM are highlighted. The conical head does not constrain the TM rotation about z axis.

In this regard, the main difference of the two GPRM unit is the shape of the plunger heads. The top unit has a conical head, while the bottom unit has a pyramidal head. This design choice is made not to over-constrain the TM rotation about the z axis (φ angle) and to define it only through the form-fit with the bottom unit (Figures 1.13b and 1.13c).
The next phase of the release procedure is the transition from the plungers to the release tips, called hand-over. The first step of the handover is the extension of the tips, which is performed applying an increasing voltage to the nominal piezo actuator of the release sub-mechanism. The tips move toward the bottom of the TM indents, where the dedicated interface, called landing area, is present (Figure 1.13a). When the TM is grabbed, the tips cover a nominal 4 µm distance before reaching the landing area (Figure 1.14a). At this point, while the tips extension continues, the plungers are retracted from the TM, maintaining an ideally constant pre-load force of approximately 10^{-1} N, monitored by the on-board electronic control loop. When the tips are fully extended (voltage approximately 120 V), the nominal TM-plunger distance along z direction is limited, approximately 14 µm, due to the small range of motion of the release tips actuators (Figure 1.14b).

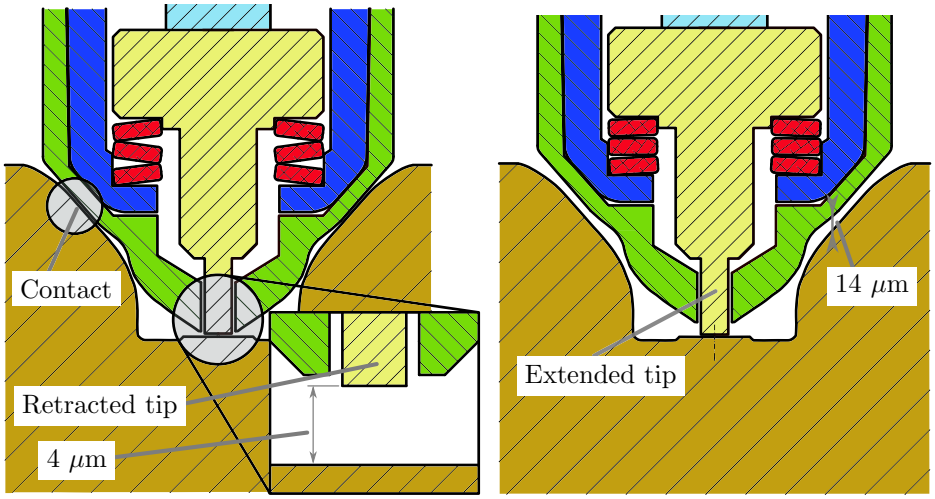

Figure 1.14: On the left, section view of the TM indent and plunger head grabbing it, nominal geometry. The gap between the retracted tip and the landing area is 4 µm. On the right, same section view depicted at the end of the handover step, with the tip fully extended (gaps not to scale).

After the hand-over, the TM is ready to be released into free-fall. The actual release is performed by quickly and simultaneously retracting the two tips, which are pushed backward by the preload of the discs spring when the powering voltage is removed. Ideally, the forces developing at the TM-tip interfaces cancel out and the TM remains still. In reality, the forces arising at the release are not symmetric, so the TM will acquire a residual velocity, directed along z. Immediately after the

tips retraction, the electrostatic control force is activated, and the TM is captured in the center of the electrode housing, so that the science phase can start.
To summarize, according to the nominal release procedure, the TM is released by the simultaneous quick retraction of the two tips, which are the only bodies mechanically holding it prior to the actual release, and no contacts between the TM and other GRS components takes place after the release. Such nominal conditions are achieved if the two plungers of the GPRM are aligned with the z axis with sufficient accuracy.
According to the mission documentation, the alignment procedure of the GPRM was performed by MAGNA Steyr on a dummy IIS and reproduced by OHB when integrating the mechanism into the flight model IIS. The achieved alignment level fulfilled the requirements imposed in the designing phases (in particular on the position and attitude of the grabbed TM, details in Chapter 2).
However, aligning the GPRM units to the IIS is not trivial, since the plungers are relatively small and with few plane surfaces, moreover the NEXLINE linear actuation has a relatively low motion accuracy, which will be discussed in Section 3.1.5.

1.3 GPRM ground testing

The criticality of the release phase in LPF, which is instrumental to the start of the science phase and governed by strict requirements on the released TM state, made it necessary to accurately characterize the performance of the release mechanism with dedicated on-ground experiments. Particular attention was given to the characterization of the forces arising at the mechanical interfaces between the TM and the tips, since according to the nominal release procedure described in Section 1.2.3, their behaviour determines the residual velocity of the TM.

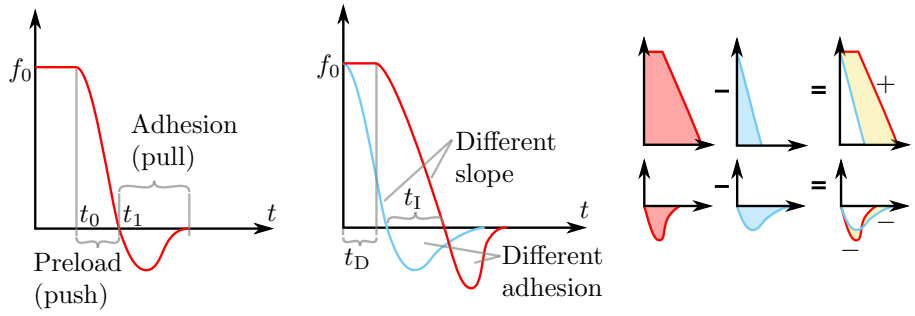

Figure 1.15: On the left, TM-tip force as a function of time at the release. The preload force is f_0, the tip retraction starts at t_0, and the adhesive pull starts at t_1. On the right, two different forces acting on opposite landing areas. The area difference is responsible of the TM residual velocity and is caused by the time delay t_D, the different retraction velocity (slope) and the different adhesive pull.

The force the TM and the tip exchange at the release starts with a positive value, equal to the pre-load after the handover. When the tip is being retracted, the force decreases down to zero, and after that instant, it becomes negative due to the adhesion phenomena, returning to zero when the actual detachment of the two bodies is reached (Figure 1.15a). Considering possible time delay and asymmetry between the motions of the two opposite release tips, the impulse given to the TM at the release can be estimated computing the difference between the areas under the curves represented in Figure 1.15b. In this way, three main contributions to the final velocity of the TM can be distinguished, namely I) the time delay in the retraction of the tips, II) the different slope of the linear decrease and III) the effect of the adhesion, which is heightened by the design choices applied to improve the GRS performance, as discussed in Section 1.2.1.
The estimation of the TM linear momentum at the release is expressed in Equation 1.2. To derive the formula, two simplifications are made, that are I) the preload force remains constant during t_{D}, approximating a cosine near zero as a constant, and II) the force decreases linearly from f_0 to 0.

$$m_{\mathrm{TM}} v_z = t_{\mathrm{D}} f_0 + \frac{1}{2} f_0 t_{\mathrm{I}} + \Delta\iota_{\mathrm{adh}} \tag{1.2}$$

Where m_{TM} is the mass of the TM, v_z the linear component of the TM residual velocity along z (assuming release forces are aligned with z axis), t_{D} the retraction lag between the two mechanisms, t_{I} the time delay at which forces reach zero while decreasing, $\Delta\iota_{\mathrm{adh}}$ the area difference due to adhesive contributions. Among the three contributions to the TM linear momentum, the most critical one was the adhesive impulse. Adhesion is difficult to predict with reasonable accuracy, and models present in the literature are not sufficient to obtain a reliable prediction. For this reason, at the University of Trento, a dedicated experiment facility was designed to estimate the effect of adhesion in the GPRM release force budget. The experimental setup includes an anti-vibration platform, on which a vacuum chamber is mounted to reproduce the outer space environment. Inside the chamber, a single unit of a GPRM engineering qualifying model (EQM) was placed. The tip of the GPRM unit applies a preload force to a wire suspended mock-up mass, of approximately 100 g. The mock-up surface reproduces the actual landing area. Extensive analyses have been carried out, characterizing the adhesive pull generated by the TM-tip interaction. The latest results confirmed that the adhesive pull, albeit not constituting a negligible contribution, should not produce out-of-requirement residual velocity, thus guaranteeing a compliant release in the 96% or more of the cases ([16], [17], [13] and [18]). In this regard, the estimated probability distribution of the residual velocity is depicted in Figure 1.16.
Apart from the adhesion testing, also other GPRM functionalities have been tested on ground. In [19], the GPRM handover and release functionality were tested, checking the MACROs implemented in the CCU for the injection procedure. The results of the testing campaign were positive. Of course, a full release with 6 DOFs TM could not be reproduced on Earth, due to the non-zero gravity environment.
To summarize, the GPRM functionality was extensively tested prior to the mission and the performed test results show that, when working under nominal conditions, the GPRM is able to release the TM fulfilling the requirements imposed on its initial state with high repeatability.

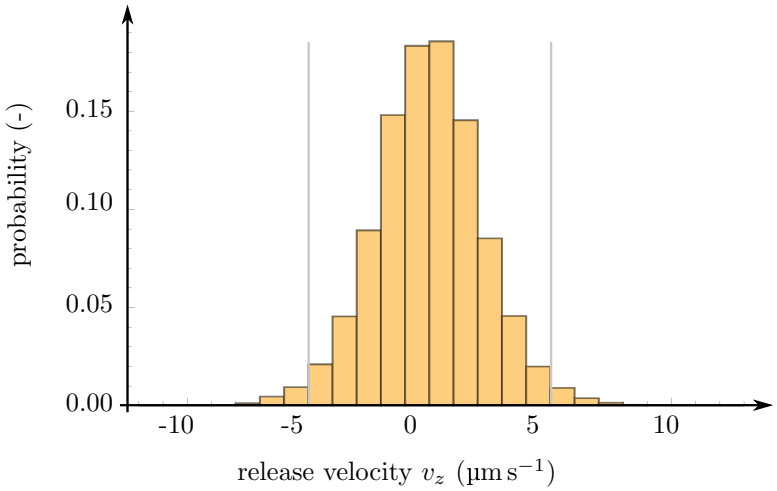

Figure 1.16: Probability distribution of the v_z residual velocity of the TM from the ground testing (from [18]). The gray vertical lines represent the mission requirements.

Chapter 2

GPRM in-flight performance and testing

This Chapter deals with the in-flight releases performed on board of LISA Pathfinder spacecraft during the nominal and the extended mission phases. Initially, the focus will be on the unpredicted residual velocities that affected the very first releases, which were performed according to the nominal injection procedure.
The releases of the TMs carried out operating the GPRMs according to the nominal injection procedure were non-viable since none of the two mechanisms was able to produce a residual velocity compliant with the requirements.
Later on, the modifications to the nominal procedure, adopted in the following mission releases and for an extended GPRM testing campaign, will be discussed and the in-flight data relative to these operations will be analyzed.
In the end, the limiting factors regarding the analysis of the telemetry data will be described and briefly discussed and the in-flight release performance of the GPRM will be summarized.

2.1 Nominal mission in-flight releases

The LISA Pathfinder success in paving the way for future GWs space observation is undeniable, as already explained in Section 1.2. The science phase results are promising in terms of the feasibility of the gravitational waves measurement from space. Despite the confirmed success of the experiment, some unpredicted phenomena happened during the injection phase of the TMs, prior to the science phase, which started on the 1st of March 2016.
The very first TMs release was performed on the 15th and 16th of February 2016 for TM_2 and TM_1 respectively. For both sensors, the pass-over from the CVM to the GPRM was executed without any problem and was followed by a successful handover to the tips. The GRS telemetry readings (preload force, TM position and attitude) were in accordance with the expectations and the pre-release TM state was compliant with the requirements of Table 1.2.
Unexpectedly, immediately after the tips retraction, which was followed by the

plungers retraction, both the TM_1 and the TM_2 acquired a large residual velocity, presenting two major problems:

- the main component of the TM velocity was not directed along z axis as it is expected given the configuration of the GPRM, which should apply forces to the TM directed mainly along z.

- the linear and angular components of the TM velocity were outside of the requirements, generating an un-controllable TM state (position and velocity).

The notation used to express the TM positions and attitude, as well as the TM linear and angular velocity components in the GRS reference frame are defined in Figure 2.1. The same notation will be used in the entire thesis.
The residual velocities produced by the GPRMs in the first mission releases are listed in Table 2.1. Observing the data, it is clear that, while the release position and attitude of the TMs fulfill the requirements, the velocities of the TMs do not. The velocity components are estimated few seconds after the tips and the plungers retraction applying a linear fit to the signals.

Table 2.1: TMs position and attitude at the release, along with linear and angular release velocities of the first in-flight releases, measured few seconds after the plungers retraction. Comparison between the requirements, the expectations and the actual measurements. Green highlighted values are to within the expectation and the requirements. Blue highlighted values inside the requirements but outside of the expectations. Red highlighted values are outside of the requirements. The relative linear fit uncertainty used to estimate the velocities is below 3% ([14]).

Pos. and vel. component	Requirement (magnitude)	Expectation (magnitude)	TM_1	TM_2	Unit
x	200	< 200	14	0	
y	200	< 200	3	2	µm
z	200	< 200	-18	0	
θ	2000	< 2000	-1111	$+50$	
η	2000	< 2000	-1166	$+314$	µrad
φ	2000	< 2000	-522	-613	
v_x	5	≈ 0	-3	$+12$	
v_y	5	≈ 0	-20	-27	$\mu m\,s^{-1}$
v_z	5	< 5	-57	-16	
ω_θ	100	≈ 0	$+681$	$+1035$	
ω_η	100	≈ 0	-797	-30	$\mu rad\,s^{-1}$
ω_φ	100	≈ 0	-1085	-430	

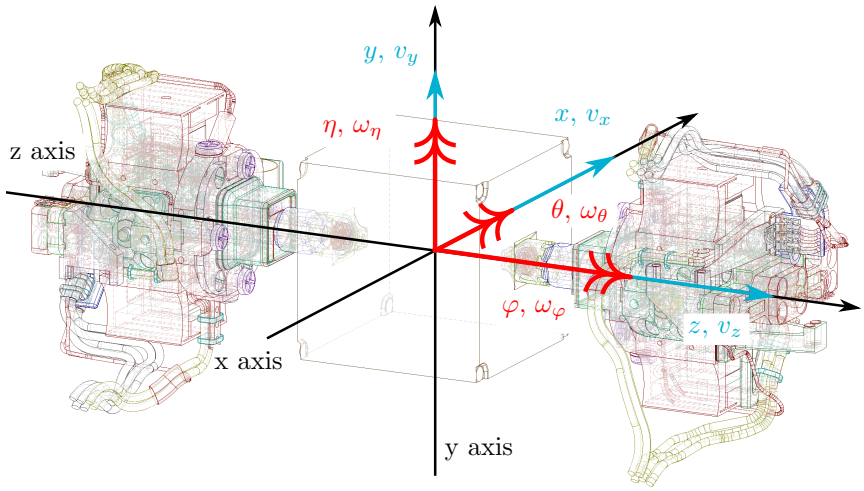

Figure 2.1: Reference frame of the GRS with the linear (light blue) and angular (red) positions and velocities of the TM. The background image is taken from the CAD model of the GRS, courtesy of RUAG.

As a consequence of the large linear and angular release velocity components, the electrostatic control force, activated right after the tips retraction, was not sufficient to capture the TM in the center of the EH immediately after the release. In fact, the TM kinetic energy was damped out to a controllable state only after some impacts with the surroundings took place.
In the case of the GRS_2 (Figures 2.2a and 2.2b), multiple impacts let the TM_2 to be captured by the electrostatic force approximately 1000 s after the tip retraction. In the case of the GRS_1 (Figures 2.3a and 2.3b), things went differently. The TM_1 kinetic energy was damped by some impacts and finally the mass stopped moving. The problem is that it was leaning on the walls of the EH (due to the high φ rotation), so in this case, the electrostatic control force was not able to control it even exploiting the damping effect of the impacts. This is a consequence of the fact that the authority of the control force decreases as the TM moves away from the center of the EH. To un-stick the TM_1, the re-grabbing function of the GPRM was exploited. The TM was nudged by approaching a plunger and the electrostatic control force safely captured it in the center of the EH several minutes after the tips retraction.
To summarize, the injection procedure performed in-flight was not nominal, and the strategy adopted to obtain a captured TM state consisted, substantially, in waiting for impacts to damp its kinetic energy and eventually produce a TM state controllable by the electrostatic actuation force. Only after several minutes, this strategy led to a captured TM state for both GRSs. Albeit being a successful strategy in the end, it is important to notice that it has three main drawbacks:

- Impacts may damage either the TM or the plunger heads surfaces.
- The time required for the capture of the TM is un-predictable since TM-plunger impacts have never been characterized. This fact is demonstrated by

the different behaviour of the two TMs since the very first releases.

- The procedure requires a manual actuation of the involved mechanisms and of the electrostatic control force.

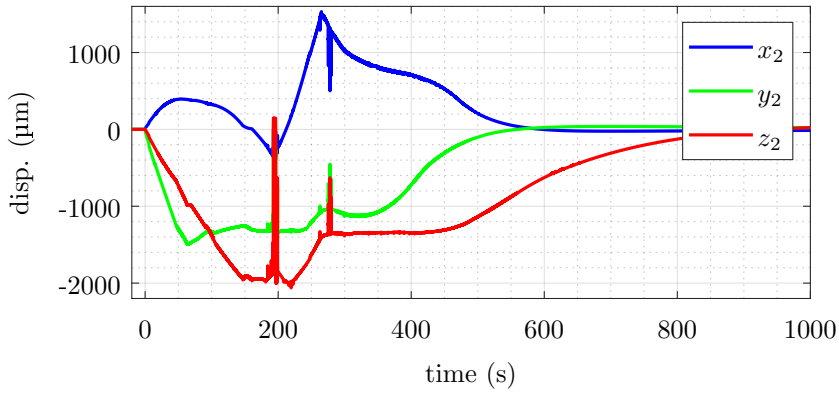

(a)

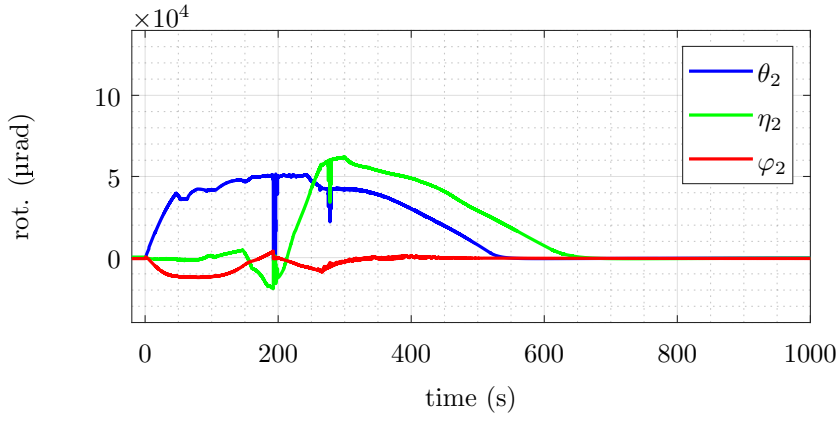

(b)

Figure 2.2: In-flight telemetry data of TM_2 position and attitude during the first release (15th of February 2016). The release instant is approximately at 0 s. Large residual velocities lead to several impacts (sudden slope changes) that slow down the TM to a point where the control force was able to capture it in the center of the EH (after approximately 1000 s). The spikes are caused by the TM grounding, due to contacts with the EH guard-rings or the plungers, that null the readings instantaneously. For a better comparison among the two sensors, axes limits are the same of Figures 2.3a and 2.3b.

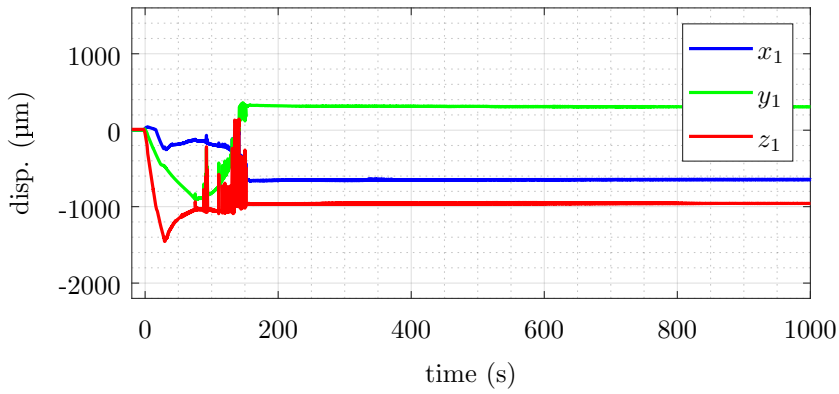

(a)

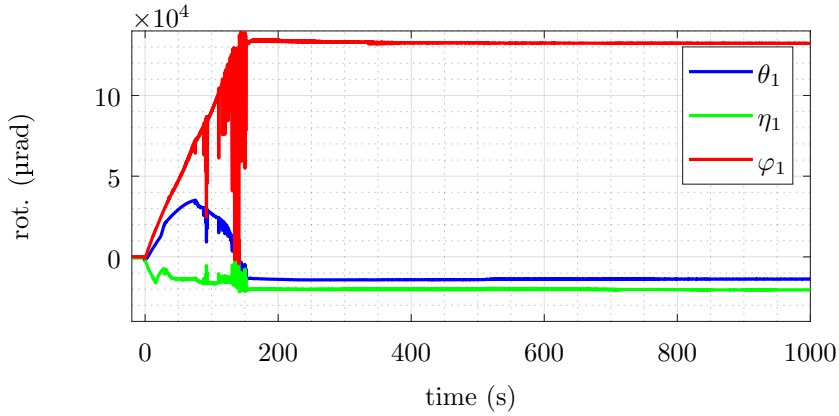

(b)

Figure 2.3: In-flight telemetry data of TM_1 position and attitude during the first release (16th of February 2016). The release instant is approximately at 0 s. Large residual velocities lead to several impacts (sudden slope changes) ending with the TM being stuck on the EH walls, as can be seen from the large deviation of the signals from zero, i.e., the center of the housing. In particular, the rotation φ_1 is critical. The spikes are caused by the TM grounding, due to contacts with the EH guard-rings or the plungers, that null the readings instantaneously. For a better comparison among the two sensors, axes limits are the same of Figures 2.2a and 2.2b.

The release strategy adopted for the subsequent mission injections, for a total of 6 releases for the TM_1 and 5 releases for the TM_2, differed from the nominal procedure. For these releases, the handover from the plunger to the tips was not performed and the TM release was realized by retracting the plungers, rather than the tips, by a small amount (in the order of 10 µm). Retracting the plunger while maintaining them close to the TM made it possible to constrain its motion to a narrow volume around the center of the EH. Of course, the small retraction of the

plungers produced impacts between the TM indents and the plunger heads. After some bounces the TM came to rest in contact with a plunger and/or a wall. It was detached by moving either the closest pin or plunger to set it in motion again in the volume confined by the plungers. At this point, the control was activated manually when the TM crossed the center of the housing. Sometimes the control activation had to be repeated after further bounces, since the electrostatic force/torque authority decreases and the readout noise increases when the TM moves away from the center of the housing.
This simplified release strategy adopted for the other mission releases suffered the same problems reported for the very firsts releases but had the advantage of avoiding impacts of the TM with the EH walls.
To summarize, all the releases performed during the nominal mission suffered from impacts, and generally required multiple interactions with the mechanism end-effectors and manual operations before reaching a successful hand-over of the TM to the electrostatic control. Even if the release strategy here described was successful for LPF case, it is not applicable in the case of LISA. The spacecraft of LISA Pathfinder was on an orbit relatively close to the Earth, so the manual activation of the mission instrumentations was possible (one-way light time of $\approx 5\,\mathrm{s}$). In the case of LISA mission, the distance between the Earth and the spacecraft (approximately $52 \times 10^6\,\mathrm{km}$) produces a high telemetry and telecommand execution time lag (approximately 350 s). Such a time lag precludes the possibility of a manual timely control of the GPRM. Moreover, the strategy of exploiting impact damping effect is unpredictable, as the two sensors of LPF demonstrated behaving differently under similar conditions. Considering that in LISA there will be a total of six TMs, this unpredictability increases the risk of a non-successful injection. In order to investigate the causes of the unexpected release dynamics of the GPRM, a dedicated experimental campaign was planned at the end of the mission.

2.2 Extended mission in-flight releases

After the end of the nominal LPF mission, the extended mission phase started. The mission extension was planned to further test LTP instrumentations and collect data useful for the improvement of the LTP. Given the unexpected behaviour of the GPRM during the fundamental phase of the TM release, it was decided to deeply test its functionality, collecting a large amount of data, in order to understand what happened during the nominal mission in-flight operations.
The test campaign of the GPRM was divided in two main sessions, in which several TM releases were performed. The first session on the 29-30th of June 2017 and the second on the 12-13th July 2017, a few days prior to the satellite transponder switch off. Apart from these dates, in which most of the testing was performed, the repositioning function of the GPRM was tested on the 9th of July 2017. Such a function is crucial since it guarantees that the TM is centered in the EH before the release.
In the first part of the test campaign, several TM releases were performed with both GPRMs in parallel (i.e., the same test was repeated for both TMs), and many modifications to the nominal release procedure were implemented.

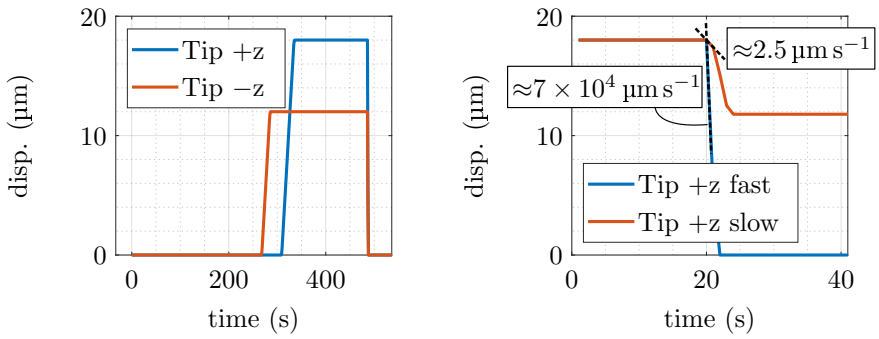

Figure 2.4: On the left, example of a reduced asymmetric tip retraction from a test of the first part of the extended campaign (June). The two tips are extended by a different quantity and simultaneously retracted to 0 µm to release the TM. On the right, comparison between a fast tip retraction and a slow tip retraction from two in-flight tests. In the slow tip retraction test the total tip motion range is reduced, from the nominal 18 µm to only 6 µm.

Minor modifications consist in I) a reduced stroke tips extraction and/or retraction (see Figures 2.4a), applied to a single tip (asymmetric) or to both tips (symmetric) and II) some releases performed using only the plungers, with a fictitious handover to the tips (tips were extended only by 1 µm, see Figure 2.5a).
Major modifications to the injection procedure are listed and accurately described in the following. They are all aimed at reducing the possibility of an undesired TM-plunger interaction at the tip retraction.

- *Hammering manoeuvre .*
  The hammering is performed just before retracting the tips. During the hammering, the bottom plunger is moved back and forth by a few steps (2 µm to 3 µm), hence the name recalling the action of a common hammer. This plunger motion, with the tip extended, should improve the fit of the plunger heads inside the indents present on the TM z faces (Figure 2.6). The idea behind this manoeuvre is that it should maximize the clearance between the TM and the plungers at the release.

- *Slow tip retraction.*
  As the name suggest, this procedure consists in performing the TM release with a slow backward repositioning of the tips. This manoeuvre substitutes the nominal quick tip retraction, performed by removing the voltage provided to the piezo-stack tip actuator. The tip backward repositioning velocity is approximatively 2.5 µm s^{-1} while the nominal retraction velocity, estimated from ground testing, is greater than 7×10^4 µm s^{-1} (see Figure 2.4b). The idea is that, using this release strategy, any preloading force on the TM should be slowly decreased, guaranteeing the symmetry between the two forces produced by the tips pressing onto the landing areas. Moreover, a slow tip

repositioning is expected to limit the vibration of the plunger at the retraction of the tip. The main drawback of the slow tip retraction is that this technique does not exploit the TM inertia to break the adhesive bonds, thus the TM may be dragged by one tip.

- *Slow plunger retraction.*
  According to the nominal release procedure, the tip retraction is immediately followed by the retraction of the plungers, with a velocity of approximately 100 µm s^{-1}. In the modified procedure, the plungers are retracted a few seconds after the tips, with an initial velocity of approximately 20 µm s^{-1} (see Figure 2.5b). The slower retraction of the plungers should guarantee lower oscillations of the plunger heads, reducing the probability of a TM-plunger collision after the release.

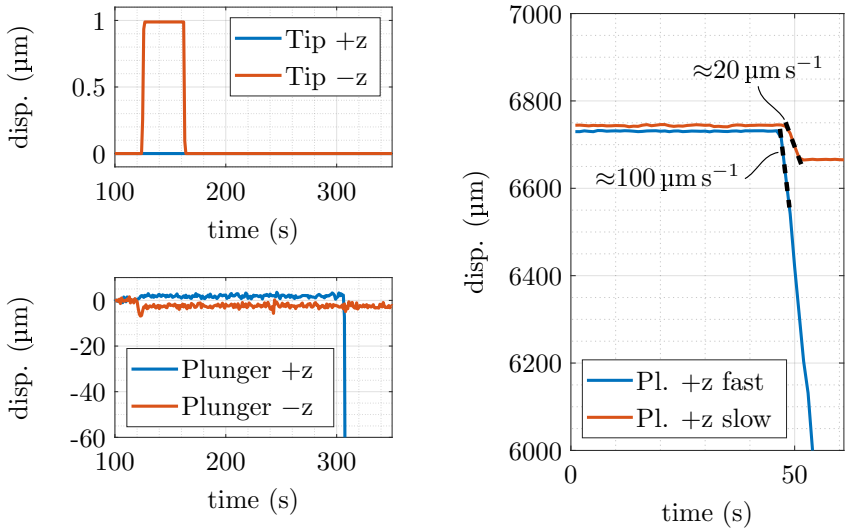

Figure 2.5: On the left, two graphs showing the fictitious handover manoeuvre performed in the test where the TM is released directly by the plungers. The +z tip is extended only by 1 µm and immediately repositioned back (top left). The actual TM release is performed retracting one of the two plungers (bottom left). On the right, difference between the nominal and the slow plunger retraction velocity.

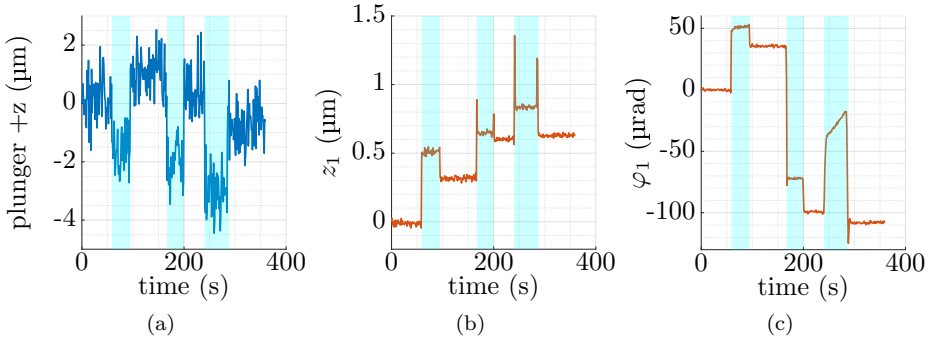

Figure 2.6: Effect of the hammering manoeuvre on the TM_1 in one of the in-flight tests. The conical plunger is moved back and forth (a) by the NEXLINE actuator, producing a settlement of the plunger heads in the TM indents. The TM_1 z_1 (b) and φ_1 (c) degrees of freedom are plotted in the same time interval, showing the effect of the settlement. The cyan areas represent the intervals where the plunger is retracted.

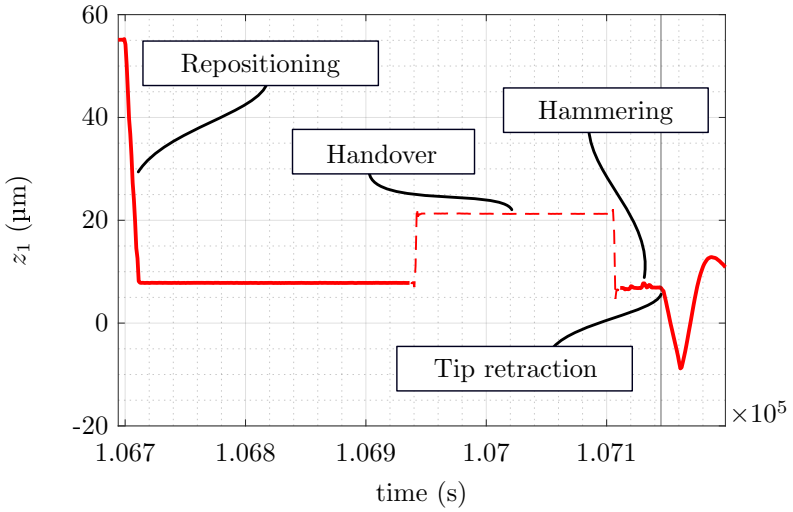

Figure 2.7: Phases of the modified injection procedure on the TM_1 z signal, in one of the automated tests performed in July. At the beginning of the test the TM is grabbed by the plungers and repositioned in the center of the EH. During the handover phase, the readings are not available, since the TM voltage, provided by the contact with the plungers/tip, is momentarily set to 0 V (bias voltage turned off). The hammering is performed right after the handover and it is followed by the tip retraction (slow or fast, alternatively from one test to the other). At this point the TM is released and acquires a residual velocity and then is eventually electro-statically controlled.

The major modifications listed above are the ones that were adopted for the second part of the test campaign, that took place in July. Similarly to the first part of the campaign, also in the second part the tests were performed in parallel on both the TMs. This second set of tests was performed implementing an automated routine on the CCU. According to the implemented routine, each GPRM was programmed to reposition the TM, release it, activate the electro-static control force, eventually capturing the TM in the center of the EH, and re-grab the TM to start the following test within a fixed amount of time and without the human interaction. The release of the TM was performed alternatively with the nominal tip retraction and the slow tip retraction techniques. In Figure 2.7 the z displacement of the TM is shown for one of the automated tests and the main phases of the injection procedure are highlighted.
The automation of the injection procedure is a key aspect of the testing campaign. In fact, it is of particular interest for the forthcoming LISA mission. The satellite constellation of LISA will orbit far away from Earth with respect to LPF spacecraft, thus there will be a commanding delay. For this reason, it is either not possible or excessively time consuming to manually control each step of the injection, especially considering that there is a total of six TMs to be released.
In the following, two Tables describing the in-flight release tests are shown, to provide a reference for the reader. Each Table is applicable to both the TMs, since the same tests are performed in parallel on the two GPRMs. In the Tables, a test index is associated to each test, which uniquely identifies it, depending on the date and time when the release was performed.
The tests reported in the Tables do not include the I) repositioning of the TM (discussed in Section 3.1.5), II) the characterization of the GPRM mechanism stiffness (discussed in Section 3.2) and III) the estimation of the TM-plunger adhesion force (below 5.2 µN). Those experiments are not indexed since their goal was not to perform a TM release.
Table 2.2 contains the list of tests performed in June, in the first part of the extended campaign. The index of those tests goes from 1 to 65. Similar tests are grouped in the same line. As can be seen, the tests are of many different types.
Table 2.3 contains the list of automated tests performed in July, in the second part of the extended campaign. The indexing is from 66 to 111, continuing the enumeration from the last of the June tests. During the automated release campaign, only two types of tests were performed, which differs by the type of tip retraction: fast or slow.
Table 2.4 summarized the results of the automated release. The results shown are preliminary, since the percentages relative to the release compliance with the requirement are only indicative. The estimation of the release velocity was taken some seconds after the actual release and is affected by a large uncertainty is some cases. As can be deduced from the Table, both the fast and slow tip retraction strategies have worked quite well for the TM_1, which was successfully captured, i.e., controlled by the electrostatic actuation force, in 91% of the fast tip tests and 100% of the slow tip tests. The second GPRM behaved worse, the TM_2 was captured 78% of the times in the fast tip tests and 43% of the times in the slow tip tests. In some case, even a non-compliant release could be captured (see TM_2 fast tip), thanks to the presence of some margins in the requirements on the TM initial state

and/or of impacts that decreased the TM velocity dissipating its kinetic energy. On the other hand, some of the compliant releases could not be captured by the control system (see TM_2 slow tip).
Despite of having adopted the improved release strategies, both the TMs were released with linear and rotational velocities different from zero, and in general the velocity along z axis was not the main component of the TM linear velocity. Moreover, impacts took place in most of the tests.

Table 2.2: List of the releases performed in flight during the first part of the extended mission campaign. Some tests are performed using only the plungers, other using the tips with nominal or slow retraction velocity, at different extraction levels.

Test index	Brief description of the type of test	Tip strokes −z, +z (µm)	Plungers velocity
1−8, 30	Nominal release, fully extracted tips	18-0 , 18-0	Nominal
9−14	Quasi-nominal release with tip strokes reduced by 1 µm	17-0 , 17-0	Nominal
15	Release performed retracting the plungers with fully extended tips	18 , 18	Nominal
16−18	Release with tip strokes reduced by 3 µm	15-0 , 15-0	Nominal
19,20	Release with tip strokes reduced by 6 µm	12-0 , 12-0	Nominal
21−23	Release with asymmetric reduced tip strokes	12-0 , 18-0	Nominal
24−26	Release with asymmetric reduced tip strokes	15-0 , 18-0	Nominal
27−29	Release with asymmetric reduced tip strokes	18-0 , 12-0	Nominal
31−33	Release with asymmetric reduced tip strokes	18-0 , 15-0	Nominal
34−36, 60−62	Reduced and slow tip retraction	18-12 , 18-12	Nominal
37−40	Reduced and slow tip retraction	18-6 , 18-6	Nominal
41−44	TM released retracting both plungers, no handover performed	0 , 0	Nominal
45−48	TM released retracting −z plunger, no handover performed	0 , 0	Nominal
49−52	TM released retracting +z plunger, no handover performed	0 , 0	Nominal
53−56	Nominal release preceded by the hammering manoeuvre	18-0 , 18-0	Nominal
57−59	Nominal release, fully extracted tips	18-0 , 18-0	Slow
63, 64	Adhesion test, not an actual release	NaN-NaN	NaN
65	Nominal release preceded by the hammering manoeuvre	18-0 , 18-0	Slow

Table 2.3: List of the automated releases performed in flight during the second part of the extended mission campaign. Tests are subdivided into two sets: slow and nominal tip retraction.

Test index	Brief description of the type of test	Tip strokes −z, +z (µm)	Plungers velocity
66, 68, odd #'s in set (69,111)	Slow and reduced tip retraction, preceded by the hammering manoeuvre	18-12 , 18-12	Slow
67, even #'s in set (69,111)	Nominal release preceded by the hammering manoeuvre	18-0 , 18-0	Slow

Table 2.4: Results of the automated releases performed in July 2017 during the extended mission phase. A release is compliant if the TM velocities after the tip retraction are to within the requirements. The TM is considered successfully captured even if impacts took place, which is the case for almost all of the releases.

	Fast tip		Slow tip	
	Compliant release	Captured TM	Compliant release	Captured TM
TM_1	77%	91%	100%	100%
TM_2	0%	78%	87%	43%

2.3 The telemetry data of LPF

In this Section, the telemetry data of LISA Pathfinder used for the analyses treated in this thesis are described. Some of the signals have already been shown in the Figures of Section 2.2, while discussing the main phases of the injection procedure and its modifications. For each of the experiments/releases performed in-flight during the extended mission campaign, a large amount of data is collected by the GRS sensors, constituting the base material for most of the calculations of this thesis. The data collected are useful to characterize the release performance of the GPRM and to identify the possible causes of its un-expected malfunctioning. The data include:

- The six TM degrees of freedom, named x_i, y_i, z_i, θ_i, η_i, φ_i, where subscript $i \in (1, 2)$ refers to the specific TM. The signals are computed from the capacitance measurement of the TM position and attitude of the sensing electrodes of the EH. The TM position and attitude signals are available at 1 Hz and at 10 Hz. The lower sampling frequency is active for all the time duration of a test, while the 10 Hz is activated only in a specific time interval, covering few phases of the injection procedure. Typically, the time interval goes from few instants prior to the TM release until a few seconds after the plunger retraction. Of course, those data are mandatory to perform any analysis on the GPRM performance, since from them the residual velocity of the TM can be estimated and impacts can be detected.

- The two signals of the preload force acting on the TM, one for each unit of the GPRM. Those two signals provide a redundant measure, because when the TM is still, the preload force on the opposite z faces is the same. The sampling frequency of those signals is 1 Hz. The preload force is one of the controllable parameters of the release mechanism, so its effect on the residual velocity of the TM must be investigated.

- The commanded tip extension for both the +z and −z tips. How much the tip is extended is not a measurable quantity (with the mission instrumentation), so it is estimated by the CCU from the voltage given to the piezo stack actuating the tip. The value of the actual extension of the tip may be different from the estimation provided by these signals. The sampling frequency is 1 Hz. The tip signals are useful to estimate the release time instant with 1 s approximation.

- The measured linear runner (i.e., plunger, unless deformation of the load cell) position along z axis, for both the +z and −z plungers. The motion of the plunger is sampled at 1 Hz and is useful to identify the timing of the injection procedures as well as to check if the plungers are being retracted/extended when an impact on the TM is detected.

- The voltage given to the plunger to permit the capacitance reading of the TM position and attitude before the release. The sampling frequency is 1 Hz.

- The temperature measured in the neighborhood of the GPRM, useful to verify if thermal distortions affect the release performance of the GPRM. The sampling frequency is 1 Hz.

For each signal listed above also the relative time array is available.
An example of the comparison between a 10 Hz signal and a 1 Hz signal of the x TM displacement from one of the automated tests is shown in Figure 2.8.
When downloading data from the mission server, they are formatted in day-long time series, each one containing several different in-flight tests (see Figure 2.9). To ease the post processing, the long time series are subdivided in single tests, which are then saved in separated files. A dedicated algorithm is developed in the software MATLAB for this purpose. Some manual corrections to the outcome of the algorithm need to be applied, since an automatic recognition of when a test starts/ends is difficult in some cases. After the subdivision is completed, all the important telemetry signals of any of the in-flight releases is easily addressed through a script by passing the index of the specific test (from 1 to 111) and the GRS sensor (1 or 2). The data file related to a specific test is saved as a MATLAB structure, containing several fields, part of which are described is Table 2.5.

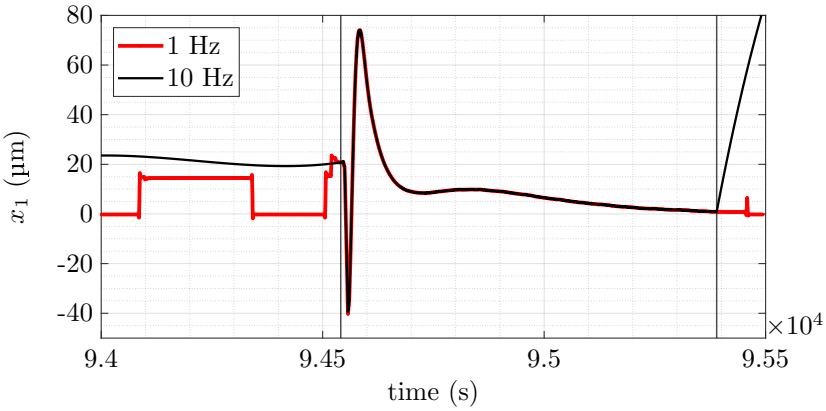

Figure 2.8: Comparison between a 10 Hz and a 1 Hz telemetry signal of the x displacement of the TM_1 (x_1) for one of the automated releases. The former signal is meaningful in the time interval limited by the two black vertical lines (the first vertical line is placed few points before the tip retraction event). In this time interval the two signals overlap since they both measure the same quantity.

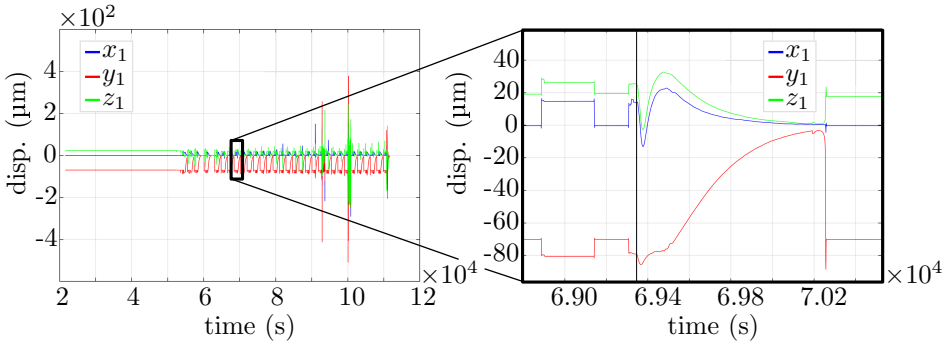

Figure 2.9: On the left, example of the three 24 hours-long time series of the TM_1 positions (time origin 2017-07-12 00:00:00.000). In the shown case, the tests are from the automated releases (July). Clearly, the data array contains several release tests. The signals on the left are magnified on the right in the time interval of a single test. The different phases of the injection procedure are visible, in particular the release instant is highlighted with a vertical line, and is preceded by the hammering manoeuvre, whose effects are barely visible on the TM positions.

Table 2.5: Example of the fields of the MATLAB structure relative to a single test. Not all the fields are listed, for example most of the TM DOFs are not reported.

Structure fields	Unit	Description
tTM_10	s	Time array of 10 Hz DOFs signals
x_10	µm	x DOF 10 Hz signal
tTM_01	s	Time array of 1 Hz DOFs signals
x_01	µm	x DOF 1 Hz signal
tGP	s	Time array of 1 Hz diagnostic signals
plP	µm	Position of the +z plunger
pinP	µm	Extension of the +z tip (commanded)
fP	N	Force applied by the +z GPRM

2.4 Instrument limits in the analysis of the flight data

Before starting the analysis of the in-flight data, it is important to address the limits of the GRS instrumentation related to the release of the TM, that are briefly discussed in this Section. First of all, it should be noticed that the telemetry data of the extended mission phase, which are the base of the GPRM performance analysis of this thesis, are collected outside of the scientific phase of the mission.
Although the release phase is pivotal for starting the science phase, the GRS is not set in science mode when performing the injection of the TM into free-fall. The reason for this is that, at the release, there is the necessity to maximize the control force/torque (such a setting is called *accelerometer mode*). In any case, the GRS is not designed to detect/monitor fast events, like the tip retraction, or the collisions of the TM with the surroundings, which are not expected according to the nominal release procedure nor during the science phase.
The main problem that prevents an accurate analysis of such instantaneous events is the low bandwidth of the telemetry signals. The sampling frequency for most housekeeping data is only 1 Hz, with the exception of the TM position and attitude signals, which are available at 10 Hz sampling frequency. Moreover, no other telemetry data is present about the GPRM dynamics, except for the housekeeping signals described in Section 2.3. No other information on the TM state is either available (e.g., presence of an unpredicted contact with the plungers and/or the tips). Apart from the sampling-frequency related limitations, other effects that limit the accuracy of the analysis are present. Those effects, listed in the following and deepened in dedicated subsections, can be subdivided into two main categories:

- Systematic noise/distortion sources. The signal noise/distortion is produced by known phenomena and is theoretically possible to estimate its influence by developing appropriate models. Among the systematic effects, there are:
  - Capacitive effect distorting the readings.
  - Triboelectric effect accelerating the TM.
  - Solar radiation pressure compensation of the satellite.

- Random noise sources. Unpredictable, essentially due to the intrinsic measurement noise, which is the sum of many noises or phenomena affecting the readings, or to temporary mechanism malfunctioning. In the first case, when possible, it is convenient to describe them by their statistical moments such as the mean and the standard deviation.
  - GRS intrinsic measurement noise.
  - Electrical artifacts in the readings.

It is important to notice that some of the effects described above are related to an actual acceleration of the TM, while other effects are not. The random noise sources, as well as the capacitive effect, do not produce an actual acceleration of the TM relative to the EH, while other effects (tribo-electrification and solar radiation compensation) generate a force on the TM or the spacecraft that produces a TM/SC relative acceleration.

The capacitance reading distortion

The electric capacitance of the GRS is affected by the presence of the plungers, since their heads, when inside the envelope of the EH, modify the geometry of the sensor. In other words, when the plungers are close to the TM, which is the case of interest in this analysis, their presence affect the surrounding electric fields, which is used to read the TM position and attitude. Thus, the voltage of the sensing electrodes changes, and the estimation of the TM position and attitude is affected. This effect creates a fictitious position and orientation of the TM in the readings according to Equation 2.1.

$$\mathbf{p}_{\text{dist}} = \frac{C_0}{C(\mathbf{p})}\mathbf{p} \tag{2.1}$$

Where $\mathbf{p} = \{x, y, z, \theta, \eta, \varphi\}$ is the array containing the actual positions and orientations of the TM, and $\mathbf{p}_{\text{dist}}$ is the array of the distorted positions and orientations of the TM. The distortion depends on the ratio between two capacitances, C_0 and $C(\mathbf{p})$. The former is the capacitance of the TM in science mode, i.e., when the plungers are retracted and the TM is centered in the EH, and corresponds to approximately 35 pF. The latter is the capacitance of the TM when the plungers are close to their indents. This quantity can be estimated from a FEM model of the sensor geometry.

The distortion effect is clearly present in the first mission releases, where a jump in the TM telemetry signals is visible when the plunger bias is activated (a voltage approximately equal to the one of the TM, V_{TM}, is given to the plungers). This event takes place a few seconds after the tip retraction and before it the plungers are grounded (see Figures 2.10 and 2.11). The jump is proportional to the value of the signal in that time instant.

In order to mitigate the distortions and read the TM state at the release instant, the plunger voltage bias was kept on during the releases of the extended mission, thus the electric fields necessary to read the TM position and attitude should not be excessively affected by the presence of the plunger heads.

Theoretically, the best way to estimate how much of the electric field distortion

affect the readings when the plunger bias is turned on, is to build a dedicated finite element model (FEM). A preliminary model was developed exactly for this purpose by the Author, and it was applied only to the very first in-flight releases, when the plunger bias was off. A more accurate model of the GRS electrostatic is currently under development and may be used to tackle this question in the future (see Section 6.3.3).
A more practical approach to this problem is to observe the 10 Hz TM telemetry signals from the in-flight tests in a narrow time interval which includes the tip retraction. In this case, if the capacitance effect is not negligible, a jump in the signals should be present at the tip retraction, when the electrical contact between the TM and the tips is opened, similarly to the jump observed in Figures 2.10 and 2.11. In order to estimate the magnitude of the jump, it is convenient to look for releases presenting two properties:

- The pre-release position and attitude of the TM is not close to zero since the jump should be proportional to the telemetry signal absolute value.
- The velocity of the released TM is low, so that the slope of the signals after the release does not hide the eventual presence of the jump.

For these reasons, the slow tip tests were considered for this analysis. The residual velocity of those tests at the tip retraction is, in general, very low ($<1\,\mu m\,s^{-1}$), thus the presence of a jump should be more visible with respect to other types of tests (fast tip retraction or plunger releases).
After looking at the mentioned data, no significant simultaneous jump, proportional to the TM pre-release state, could be observed on the DOFs signals of any test (an example is presented in Figure 2.12). Thus, as a first approximation, the distortion effect can be neglected in the analysis of the GPRM performance when the bias is on.

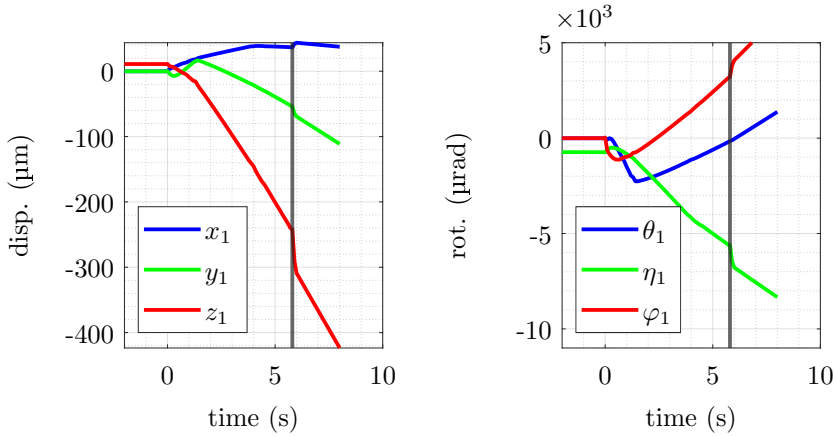

Figure 2.10: TM_1 telemetry signals from the first mission release. The tip retraction takes place at ≈0 s, and the plunger bias is activated at ≈5.8 s (black vertical line). A small jump in the signals is present at that instant.

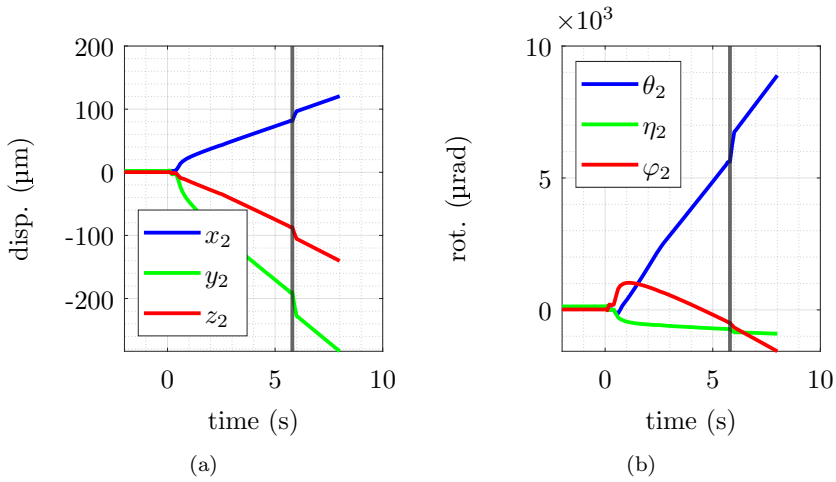

Figure 2.11: TM_2 telemetry signals from the first mission release. The tip retraction takes place at ≈0 s, and the plunger bias is activated at ≈5.8 s (black vertical line). A small jump in the signals is present at that instant.

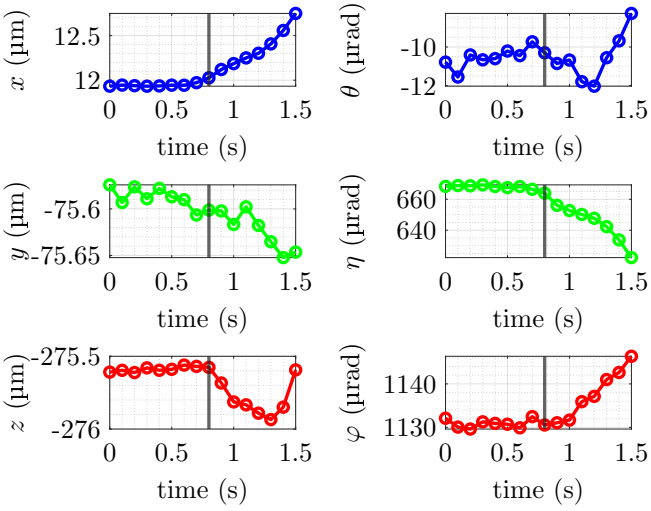

Figure 2.12: TM degrees of freedom in one of the slow tip retraction tests. The black vertical line approximates the beginning of the retraction. As can be seen, no evident jump is present, simultaneously, in the six signals. This means that the distortion due to the capacitive effect is negligible (the relative "jump" is −0.015%, −0.000%, −0.000%, −0.039%, +0.018%, −0.001% for x, y, z, θ, η and φ respectively).

The triboelectric effect

When the TM is in the pre-release phase, it is held in place only by the two tips (or the two plungers, depending on the type of test) engaging the landing areas. Thus, the TM and the GPRM units are electrically in contact. At the release, a net electric charge may remain on the TM due to different work functions between the TM and the GPRM end effectors materials and due to the triboelectric effect. Such a net charge is estimated to be in the order of -1.6×10^{-11} C ([20]).
A simple model, designed to estimate the effect of the tribo-electrification on the TM motion after the release, is built and described in the following. In particular, the model estimates the acceleration of the TM produced by the tribo-electrification in the worst-case scenario, i.e., when one plunger is close to the TM (and the other is far away) and when the voltage difference is high.
The net TM charge at the release, Q_{TM}, is equal and opposite to the sum of the charge of the plunger Q_{pl} and the electrode housing Q_{EH}:

$$Q_{\mathrm{TM}} = -Q_{\mathrm{pl}} - Q_{\mathrm{EH}} \tag{2.2}$$

Which can be rewritten in terms of voltage difference ΔV and capacitances C:

$$Q_{\mathrm{TM}} = -C_{\mathrm{pl}}(\vec{c})\Delta V(\vec{c}) - C_{\mathrm{EH}}(\vec{c})\Delta V(\vec{c}) \tag{2.3}$$

Where $\vec{c}$ represents the vector of the geometrical configuration of the GRS, i.e., it contains the positions and rotations of the TM and the z position of the plungers. The voltage difference between the TM and the EH/plunger is ΔV (this voltage difference does not depend on the injection voltage, since it is a direct current effect). The capacitance between the TM and the EH, at the release, can be assumed constant since the TM is close to the center of the EH. Its value is computed from FEM models and it is approximately equal to C_0 =35 pF. From Equation 2.3, the potential difference can be written as:

$$\Delta V(\vec{c}) = -\frac{Q_{\mathrm{TM}}}{C_{\mathrm{pl}}(\vec{c}) + C_0} \tag{2.4}$$

Where the only unknown quantity is $C_{\mathrm{pl}}(\vec{c})$. Its value strongly depends on the relative position and the geometry of the plunger head and the TM indent. To simplify the computation, it was decided to study the effect only along direction z. In order to estimate the capacitance $C_{\mathrm{pl}}(z)$ (function of TM z coordinate given a fixed z position of the closer plunger), a dedicated 3D FE model was built (see Figure 2.13).

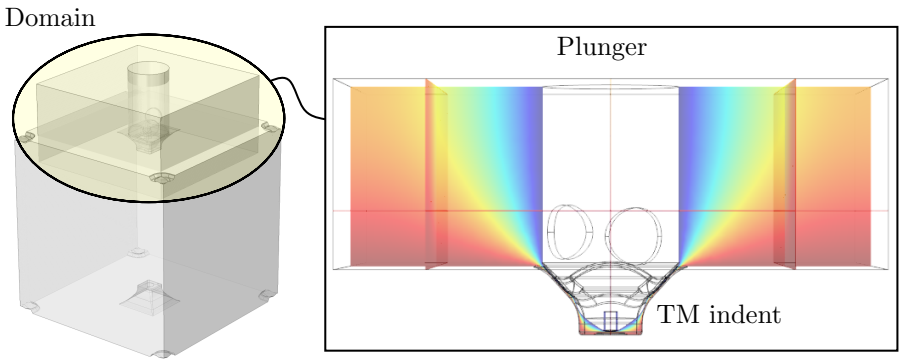

Figure 2.13: Scheme of the 3D FEM geometry used to estimate the triboelectric effect on the TM due to the presence of a plunger nearby. The capacitance of the TM with respect to the plunger is estimated from the electric field potential (on the left).

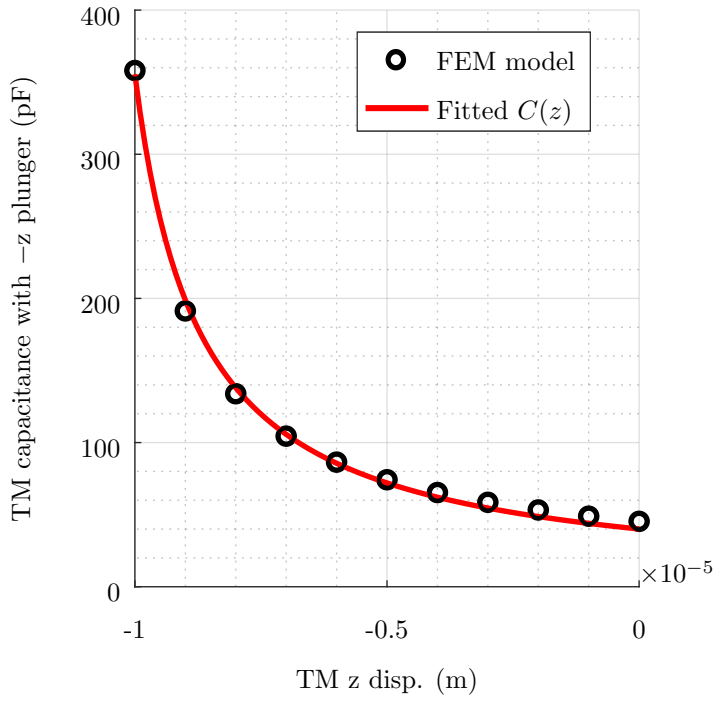

Figure 2.14: Capacitance of the TM versus the −z plunger located 11 µm away from the centered TM, to simulate the release conditions. The simplified analytical capacitance (red curve) is fitted to the FEM data (black dots).

In the model, the pyramidal plunger was initially set 11 µm away from the TM, which was centered in the origin. The plunger head and the TM constitute the two armors of a capacitor, whose capacitance needs to be estimated. The model was run for different z positions of the TM, obtaining a series of points describing the TM-plunger capacitance as function of z.
The next step was to fit a parametric function to the model results. The function chosen is shown in Equation 2.5.

$$C_{\mathrm{pl}}(z) = \frac{p_2}{p_1 + z} \tag{2.5}$$

The choice of the function was made so that it is sufficiently simple (only two parameters) but able to fit the model data with a reasonable accuracy, as shown in Figure 2.14. In fact, the structure of the function resembles the case of two planar conductors set at variable distance. The fitting was performed with the *fminsearch* function of MATLAB, and the optimal parameters found are shown in Table 2.6.
From the value of the capacitance, the attractive force between two conductors is easily computed. Consequently, the magnitude of the acceleration of the TM, $a_{\mathrm{TM}}(z)$, can be computed as:

$$a_{\mathrm{TM}}(z) = \frac{1}{2m_{\mathrm{TM}}} \left| \frac{\mathrm{d}C_{\mathrm{pl}}(z)}{\mathrm{d}z} \right| \Delta V(z) = \frac{1}{2m_{\mathrm{TM}}} \left| \frac{\mathrm{d}C_{\mathrm{pl}}(z)}{\mathrm{d}z} \right| \left(\frac{Q_{\mathrm{TM}}}{C_0 + C_{\mathrm{pl}}(z)} \right)^2 \tag{2.6}$$

Where m_{TM} is the mass of the TM. Inserting into the equation the values of Table 2.6, the TM acceleration due to the triboelectric effect estimated from the model remains below $9 \times 10^{-8}\,\mathrm{m\,s^{-2}}$ even considering a TM-plunger gap as small as 1 µm. Considering this is a worst-case scenario, such an acceleration translates into negligible TM velocity variation in the time span of tens of a second (sampling frequency), which is the number of samples necessary to estimate the TM velocity with reasonable accuracy. A detailed analysis of the impulses received by the TM in the presence of a potential difference with the plunger under different GRS configuration is carried out in [21].

Table 2.6: Value of the parameters used to estimate the acceleration of the TM along z axis due to the triboelectric effect. The fitting parameters are shown with their 95% confidence interval.

Param.	Value	Unit	Description
C_0	35	pF	Capacitance of the centered TM with the EH
m_{TM}	2	kg	Mass of the TM
Q_{TM}	-1.6×10^{-11}	C	Charge of the TM
p_1	11.3 ± 0.1	µm	Fit parameter 1
p_2	451 ± 25	pF µm	Fit parameter 2

Spacecraft acceleration for the solar pressure compensation

According to the mission documentation, the thrusters of the spacecraft of LISA Pathfinder are activated in open loop to compensate for the solar radiation pressure ($\approx$28 µN) and keep the spacecraft centred on the floating TMs. The compensation force of the thrusters, if not equal to the solar pressure, accelerates the spacecraft producing a relative motion between the TM and the spacecraft, that may be detected as a TM acceleration when observing the telemetry readings. Considering a 10% compensation error, the maximum relative acceleration, which is directed along the z axes of the GRSs, since the spacecraft is oriented such that the z axes are parallel to the Earth-Sun line segment, is in the order of $2.8\,\mu\text{N}/480\,\text{kg} \approx 6.3 \times 10^{-9}\,\text{m}\,\text{s}^{-2}$. In a large time interval after the release of 10 s, such a relative acceleration will generate a relative velocity of $\approx 0.06\,\mu\text{m}\,\text{s}^{-1}$, which is negligible if compared to the typical residual velocity, thus, it should not significantly affect the analysis of the GPRM performance.
More details on the thrusters management system of LPF can be found in [22].

GRS measurement noise

The measurement noise constitutes the main noise source for the analysis dealt with in this thesis. This noise is difficult to predict with models, so it was estimated directly from the in-flight data. The estimation of the measurement noise is possible in any phase in which the TM is still, so the signals have a slope close to zero. For example, when the TM is grabbed by the plunger, or held by the two tips (pre-release), or even when it is free falling inside the EH with negligible velocity with respect to the satellite. When possible, the measurement noise was estimated specifically for each test. For example in the pre-release phase the noise can be easily estimated for all of the tests. Regarding the free-falling TM noise, it was not possible to estimate it for any release, due to the lack of time intervals with a slowly free-falling TM few seconds after its release. When a release is performed, the GRS is set in *accelerometer mode* (as explained in the introduction of Section 2.4) thus the noise affecting the readings is greater than during the science operations. Details on the estimation of the measurement noise will be discussed in the following Sections of the thesis.

Electric artifacts

In some tests, strange electric artifacts are visible in the readings. Such artifacts cover variable time intervals, sometimes precluding the estimation of the TM release velocity. The presence of such artifacts appears to be of a casual nature, which significantly affects the readings only in a minor number of tests. A sudden sawtooth behaviour of one or more TM signals is clearly visible in these cases. When the artifacts are present in a key phase of the injection procedure, for example near the release of the TM, the test is discarded from the analysis. What causes this strange distortion of the reading is an undesired electric crosstalk between the actuation and the sensing electrical signals. Such a crosstalk is proportional to I) the absolute readout of the bridge (i.e., TM displacement/rotation) and II) the voltage

that is actuated on each electrode pair on a face of the EH. This phenomenon happens only in the automated tests (12th-13th July), since those are the tests where the actuation is turned on a few seconds after the TM release.
To summarize, there are several noise sources affecting the readings of the LPF position and attitude telemetry signals that may affect the injection procedure analysis (a summary is listed in Table 2.7). Most of those effects, at least as a first approximation, do not influence the analysis of the TM residual velocity. Other effects need to be considered. The main one is the measurement noise of the GRS, which cannot be avoided, but can be estimated from the readings. Another effect, the presence of artifacts in the reading, since is unavoidable, is simply detected, and in case it heavily affects the readings, the test is discarded.

Table 2.7: Summary of the noise sources and their effect on the GPRM analysis.

Noise source	Impact on the analysis
Capacitive effect	Negligible
Triboelectric effect	Negligible
Solar radiation compensation	Negligible
CCU filtering	Negligible
GRS noise	Non-negligible
Reading artifacts	Non-negligible, but affecting only few tests

2.5 The GPRM pre-release performance

The focus of this thesis is to study the release performance of the GPRM exploiting the extended mission campaign data. The analysis of the in-flight data starts from the pre-release phase, since this is the phase that immediately precedes the actual release of the TM. It is important, in order to understand the release dynamics, to check the TM state before the release. In this Section, important considerations regarding the pre-release state of the TM are reported, focusing on some of the criticalities that should be addressed to improve the performance of the GPRM for the LISA mission.
For each extended mission release, a set of 20 data points were chosen on every TM DOF 10 Hz signal. The set is selected in a time interval immediately preceding the tip retraction, so that the TM pre-release state can be computed and compared to the actual requirements. The mean of the 20 points corresponds to the TM pre-release displacement or rotation (according to which DOF is analyzed). Moreover, a linear fit is applied to the points, in order to estimate the pre-release velocity of the TM (the slope of the linear fit). This is done to verify if the TM is still as it should be in the pre-release phase.
In Figure 2.15, the positions and orientations of the TMs in the pre-release phase are plotted. The x axis of the plot reports the index of the test (referred to Tables 2.2 and 2.3).

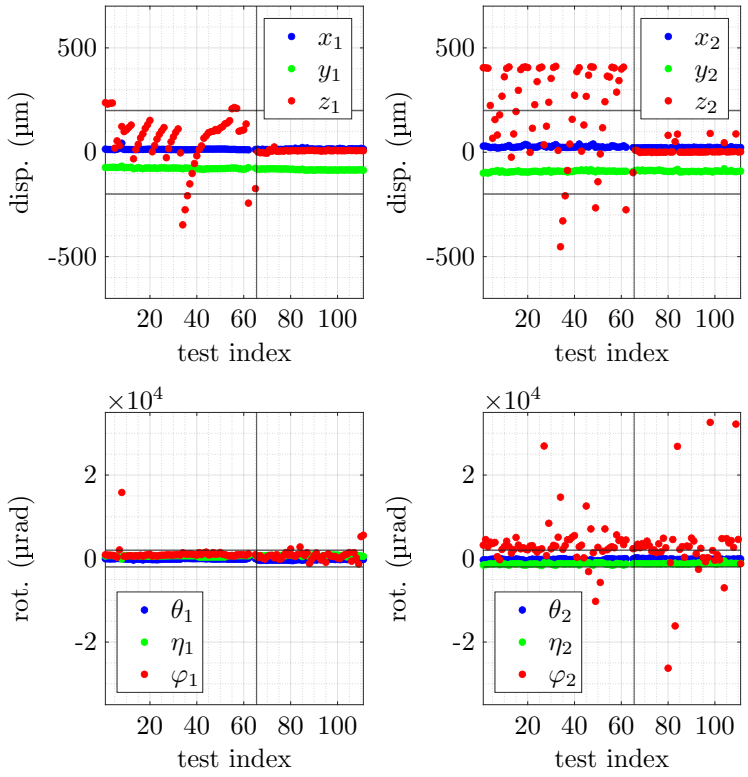

Figure 2.15: TM displacements and rotations in the pre-release phase for the in-flight releases from the extended mission phase. The two graphs on the left refers to the TM_1, the two graphs on the right to the TM_2. The values reported are computed averaging a set of 20 data points just before the release. In the graphs the black horizontal lines represent the mission requirement on the initial TM state ($\pm$200 µm and $\pm$2000 µrad). In each plot, the black vertical line separates the non automated tests (index < 66) from the automated tests (index ≥ 66).

The TM_1 linear displacements (top left graph) x_1 and y_1 are always well within the requirements, which are represented by the horizontal black lines, while z_1 sometime exceeds the limits in the non-automated tests (test index lower than 66). The fact that z_1 in the non-automated tests is not always inside the requirements is not critical. In fact, the repositioning function of the GPRM, which should bring the TM z position inside the desired zone, was simply not performed. When the repositioning is performed in all the tests (see automated tests), the GPRM is always able to bring the TM inside the requirement. The violation of the pre-release z requirement ($\pm$200 µm) has a criticality limited to the decreasing of the maximum control force along z. Thus, the problems here highlighted are not related to the TM z coordinates at the pre-release.

The same exact considerations can be deduced from the displacements of the TM_2 (top right graph). The DOFs x_2 and y_2 are always within the requirement, while z_2 sometimes exceeds the $\pm 200\,\mu m$ margin for the non-automated tests. One thing to notice is that the second sensor seems to have larger dispersion in the z pre-release position of the TM. Again, this should not significantly influence the release performance of the GPRM. Regarding the orientations of the TMs, starting from TM_1 (bottom left graph), angle θ_1 and η_1 are always to within the requirements, while angle φ_1 sometimes exceeds them. Similar considerations are valid for the TM_2 orientations (bottom right graph), even if this time the angle φ_2 is much more scattered with respect to the other TM. Most of the times it exceeds the requirement by a factor 2 or 3, but there are cases in which the TM rotation is even greater.
The following considerations are valid for all the tip retraction tests, which are the majority of the in-flight tests, and not for the plunger retraction tests (indexes from 41 to 52). The fact that angle φ is less repeatable with respect to the other two orientations is explained by the mechanism geometry. In the pre-release state, the form-fit between the pyramidal plunger head and the TM indent is missing (the indent surface is separated from the plunger head by the extraction of the tip). This form fit is the only constraint on the rotation of the TM about z apart from the friction force present on the landing areas. Differently from the z displacement, a TM φ rotation influences the relative gap between the TM indent surface and the plunger head. This fact means that, if the TM is highly rotated about z, then it will be rotated also relative to the plungers. In particular, it will be rotated with respect to the pyramid faces of the bottom plunger. As a direct consequence, the clearance between the TM and the $-$z plunger will be reduced. If the rotation of the TM is excessive, there will be a configuration where the clearance is reduced to zero (i.e., there is a contact).
To check this hypothesis, it is necessary to consider the exact envelopes of the bodies. Given the fact that the geometries involved are complex, a CAD software is used to estimate the relative angle between the TM and the plunger that lead to a zero clearance, which is equal to $\Delta\varphi_{TM-pl} \approx 4800\,\mu rad$. This angle is computed considering that any TM-plunger misalignment in the other directions is null and that the mechanism is in nominal pre-release state, i.e., full $18\,\mu m$ tip extension. According to this idea, supposing:

1. the pyramidal plunger head has a negligible rotation about z with respect to the EH reference frame

2. the TM is in the nominal pre-release state

then the maximum φ_{TM} angle should be in the range $\pm\Delta\varphi_{TM-pl}$. From the bottom graphs of Figure 2.15, it is clear that the TM is, sometimes, more rotated about φ than the mentioned maximum limit, reaching values up to $33\,000\,\mu rad$, i.e., almost 7 times the maximum limit. This means that one or both the hypotheses introduced has to be discarded. The first one, i.e., that the pyramidal plunger is rotated about its main axis, is checked firstly looking at the mission documentation relative to the integration of the GPRM units in the GRS. Post integration verifications reported that the mechanism was aligned to within the specified tolerances. In particular, the rotation of the two pyramidal plunger around their axis

is -117 ± 469µrad and -234 ± 699µrad for $GPRM_1$ and $GPRM_2$ respectively (in the GRS reference frame).
Another check that can be performed is to look at a set of flight-data where the TMs were grabbed by the plungers and repositioned back and forth along z a couple of times, exploiting the repositioning command of the GPRM. Looking at those data, where the form fit between the TM and the pyramidal plunger head constrains the φ angle of the former, its value remains in the order of 1×10^3 µrad for the TM_1 and 2.7×10^3 µrad for the TM_2, with a maximum deviation of approximately 1×10^2 µrad when the TM is repositioned. Those values can explain why the TM_1 and TM_2 pre-release φ values do not have zero mean and, for the TM_2, why they lie slightly outside of the 2000 µrad requirement on average.
The problem is that the in-flight data are not in agreement with the on-ground GPRMs alignment verifications. A possible reason for this may be related to the way the plunger φ rotation is measured. According to the mission documentations, the rotation of a plunger around its main axis is measured with a mechanical feeler touching two points on the linear runner that are far away from the z axis (to increase the measurement precision). This procedure has the drawback of not measuring directly the pyramid surfaces of the plunger head. In fact, such a direct measurement would be difficult since the plungers are quite small (10 mm diameter). Nevertheless, considering the actual alignment the in-flight data of the repositioning tests to be more representative, the check performed on the first hypothesis is not sufficient to explain the large values of pre-release φ observed in some of the in-flight tests. Thus, the second hypothesis, i.e., that the TM is properly held in position by the tips (nominal pre-release state) needs to be verified.
To verify this, it is useful to check the z position of the linear runners (which corresponds to how much each plunger is extracted) when the TM is in the pre-release phase. Rather than considering the displacement of the single plunger, which is not useful, the sum of the extractions of the two plungers is considered. This sum is used to estimate the relative distance between the two linear runners (approximately equal to the relative distance of the two plungers).
In Figure 2.16, the zero-mean distribution of the φ pre-release angle of both the TMs is plotted against the sum of the plunger extensions. The sum is an index of the penetration of the plunger heads into the TM indent. It should be noticed that the uncertainty on the plunger extensions sum is not known, it depends on the position sensor noise and on the drift. The fact that the plunger release tests (cyan and orange dots) are above the tip release tests (blue and red dots) is in accordance with the expectations. In fact, in the plunger tests, the penetration of the plunger should be at its maximum since there is no handover to the tips. Since the plunger tests are carried out among the tip tests, the fact that they remain separated suggests that the drifting of the sensor is not so excessive as to invalidate the conclusions.
Interesting considerations on the GPRM pre-release performance can be drawn observing the behaviour of the data points of the tip tests that lie outside of the geometrical boundaries of ±4800 µrad on the relative φ angle between the TM and the plunger, which are represented by the shaded area. It can be seen that, as soon as the penetration of the plungers moves away from the maximum (0 µm on the y axis), the relative φ angle may assume larger and larger absolute values. Such

a behaviour is due to the fact that a lack of penetration between the pyramidal indent and the TM increases the maximum relative angle reachable before having a contact. To confirm this hypothesis, the maximum relative angle between the TM and the pyramidal plunger head is computed from the CAD model as a function of the penetration.
As shown in Figure 2.16b, the computed trend is compatible with the in-flight data, enforcing the hypothesis that in some tests the TM was not in the nominal pre-release state before the release took place. Another problem highlighted in this graph is that, in some tests, the lack of penetration of the plungers is clearly present even in the absence of high φ rotation. There are tests close to 0 µrad on the x axis but well below the maximum penetration on the y axis. A possible explanation of those points is given in the next paragraph, that deals with the preload force acting on the TM.

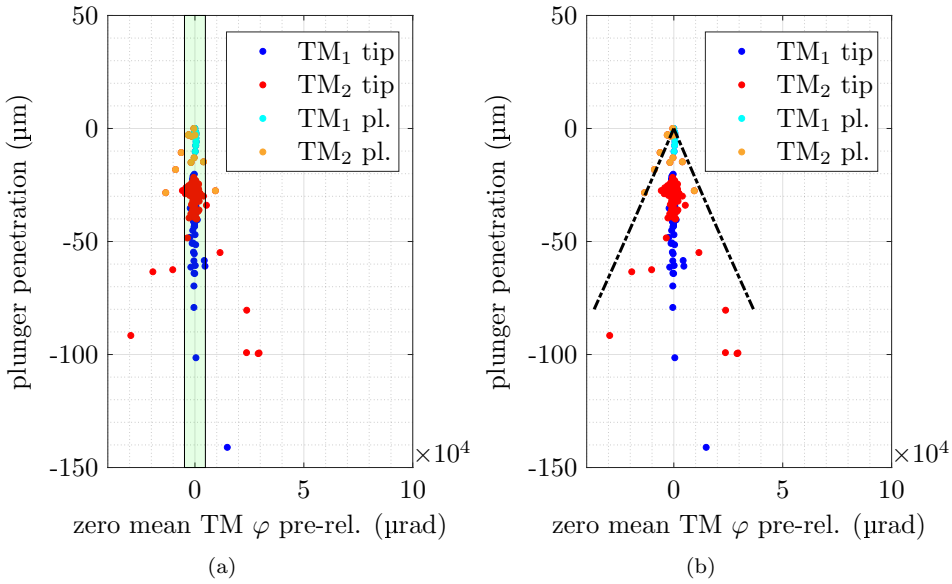

Figure 2.16: Penetration of the plungers (sum of the z position of the linear runners) in the TM indent as a function of the zero-mean pre-release φ angle of the TM (the dots relative to each TM have 0 mean on the x axis). The tests are subdivided by the sensor (1 or 2) and by the type of test (tip release tests vs plunger release test). The shaded area on the left graph represents the geometrical limit of ±4800 µrad relative angle between the TM and the plunger, that cannot be exceeded if the TM is properly handed-over to the tips or held by the plungers. The black lines on the right graph represent the maximum allowable relative φ angle as function of the penetration according to the CAD model.

The preload force on the TM

At this point, it is reasonable to check the preload force on the TM for any of the in-flight tests. The preload on the TM at the pre-release is measured by two sensors simultaneously, one for each half of the GPRM. Ideally, the two sensors should measure the same quantity, but the measurement noise and the imperfect sensor calibration produce two different measurements. The pre-load force exerted by the tips on the TM landing areas before the release is provided by the GPRM telemetry signals at 1 Hz sampling frequency (Figure 2.17). In the neighborhood of the release instant, it is possible to detect a stepwise force drop ΔF_i in the signals related to the two opposed GPRM halves (referred to with subscripts P for pyramidal and C for conical), which provides the redundant measurement. The single force drop is estimated from the force signal taking the difference between the average force before and after the release. The standard deviation of the force drop, named $\sigma_{\Delta F_i}$, is computed as the RSS of the standard deviations before and after the drop.

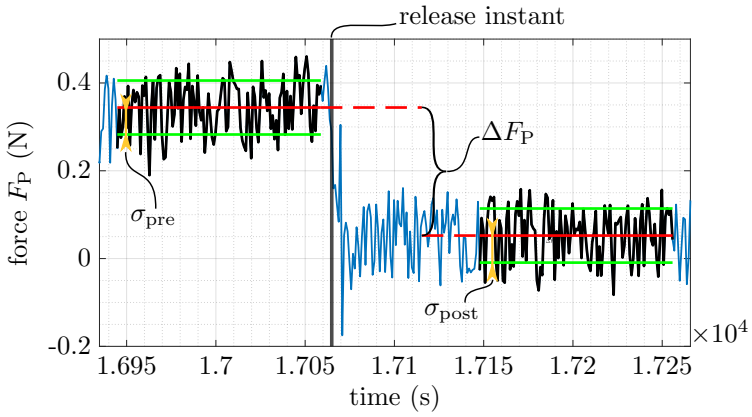

Figure 2.17: Example of the drop in the force signal detected after the release of the TM. The shown case is from the pyramidal plunger of an in-flight test. The quantity ΔF_P represent the difference between the mean force before and after the release (red lines). The green lines represent the standard deviations of the force signal.

The redundancy coming from having computed two force drops may be exploited to increase the precision of the estimated preload, minimizing the variance of the estimator, applying the Bayesian estimation shown in Equations 2.7 and 2.8.

$$F = \frac{\sigma^2_{\Delta F_P} \Delta F_C + \sigma^2_{\Delta F_C} \Delta F_P}{\sigma^2_{\Delta F_P} + \sigma^2_{\Delta F_C}} \tag{2.7}$$

$$\sigma_F = \sqrt{\frac{\sigma^2_{\Delta F_C} \sigma^2_{\Delta F_P}}{\sigma^2_{\Delta F_C} + \sigma^2_{\Delta F_P}}} \tag{2.8}$$

where F is the pre-load force estimation and σ_F is its standard deviation.
The nominal preload before the release should be approximately 0.3 N. During

the extended mission tests, this parameter was changed in some of the tests to verify its influence on the GPRM release performance. According to the extended campaign log documentation, in the first part of the campaign (June), for some tests, it was lowered down to 0.1 N or even to 0.05 N. In the second part (July) it was increased to 0.5 N. Looking at the estimated preload for all the extended campaign tests, plotted in Figure 2.18, it is clear that the desired preload is not achieved for most of them. This fact represents the first criticality of the GPRM. Looking at the force sensors readings, the mechanism is not able to pre-load the TM with the desired preload force. The question, now, is *why does this happen?* With the documentation available, it is difficult to give an accurate answer. Part of the problem is certainly related to the force sensors precision and accuracy. The standard deviation of the force signal, when the force should be constant, is in the order of 0.05 N, which is relatively high if the target preload is 0.3 N. Another part of the problem may be related to how and when the CCU computes the pre-load force to feed the control loop that should set the final pre-load to the desired value. In fact, for the automated tests, the desired preload was set before performing the hammering. This, along with other aspects regarding the overall performance of the handover procedure was not investigated in this thesis but is certainty an aspect to be taken into account for the LTP improvements.

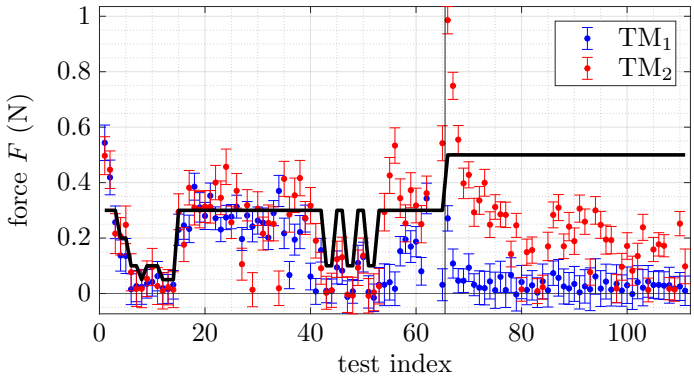

Figure 2.18: Estimated preload force on the TM in the pre-release phase for the in-flight test of the extended campaign. It can be seen that many points are compatible with a zero pre-load (error bars encompassing 0 N value). Moreover, in many tests, the preload achieved is different from the preload set during testing (thick black line). In the automated tests (indexes 66-111, on the right of the black vertical line) the preload was set to 0.5 N before the hammering and in the pre-release phase it was almost always less.

At this point, it is of interest for the analysis to consider the possible correlation between the pre-load force and the φ angle of the TM. The idea is to show that, when the φ angle is large, the TM is not properly handed-over to the tips, i.e., the pre-load force acting on it is potentially zero. This is shown in the plot of Figure 2.19. When the preload is sufficiently high, the φ angle of the TM is inside the geometrical limits imposed by the geometries of the involved parts (shaded

area), and this is valid for both the TMs. When the pre-load is low, compatible with zero, the TM orientation may exceed the geometrical limits. There are a few tests (five) where the pre-load force is small but the 1σ interval does not cross the 0 N axis, so probably it is not zero, and still the TM is highly rotated. In those tests the plungers lack of penetration is always below 28 µm, referring to the plot of Figure 2.16, so the plungers are not fully penetrated in their indent. The hypothesis is that, for those tests, the TM was stuck in this highly rotated configuration and the plungers were pushing it with a force not sufficient to un-stick it. Also this aspect is critical and should be considered in the improvements of the GPRM for the LISA mission.

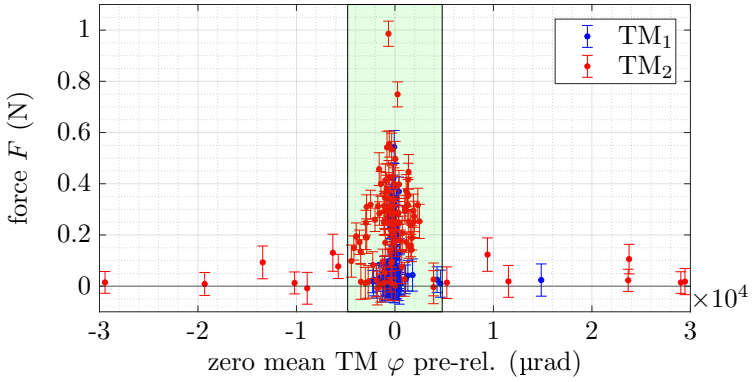

Figure 2.19: Zero mean TM φ plotted against the pre-load force for the extended mission campaign tests. When the force is above 0.2 N, the TM φ rotation is within the geometrical limits imposed by the pyramidal plunger head in the pre-release.

The TM velocity before the release

The demonstrated lack of a correct handover from plungers to tips, mainly due to a null or too low pre-load force or to a TM stuck with large φ angle, make it necessary to also check the velocity of the TM at pre-release. According to the nominal release procedure, the TM should be still before its release. This hypothesis was checked fitting a linear model to the set of 20 data points, preceding the actual release, used for the previous analysis. This operation was carried out for all the six TMs DOFs of all the extended campaign tests.
The fitted velocity components of the pre-release TM state are shown in Figure 2.20. The graphs on the left are referred to the TM_1, the ones on the right to the TM_2. The scale of the plots is common for the two TMs for the linear and angular components. From the plots, it is clear that there are some tests where the TM is not still before its release. In particular, for some of the automated tests (test index 66-111), the φ angle of TM_1 and the x, y and φ components of TM_2 present a non-zero velocity. The fact that the TM is not still before the release seems to be a problem affecting only the automated tests. The non-zero linear velocities are present when the pre-load force is compatible with zero, except for one test TM_1, where the pre-load force is barely positive ($|F| - \sigma_F = 0.0041$ N). In that

test, where the penetration is on the high side ($-35.1\,\mu m$), the tips are probably exerting a very low force on the landing areas and the TM is rotating about z axis. The rotation of the TM about z axis, which is the axis of the tips, is counteracted only by the friction torque due to the tips pushing on the landing areas, which is proportional to the pre-load force but still very limited since the radius of the tips contact patch is in the order of $10\,\mu m$. In other words, if the TM acquires a velocity around φ just before the release, the friction force due to the contact with the tips may not be sufficient to stop it in a short period of time if the preload is very low. The relation of the preload force with the pre-release φ velocity of the TMs is shown in Figure 2.21. Such a velocity is present only when the preload force is low and compatible with 0 N (with the unique exception of the single test of the TM_1 discussed above).

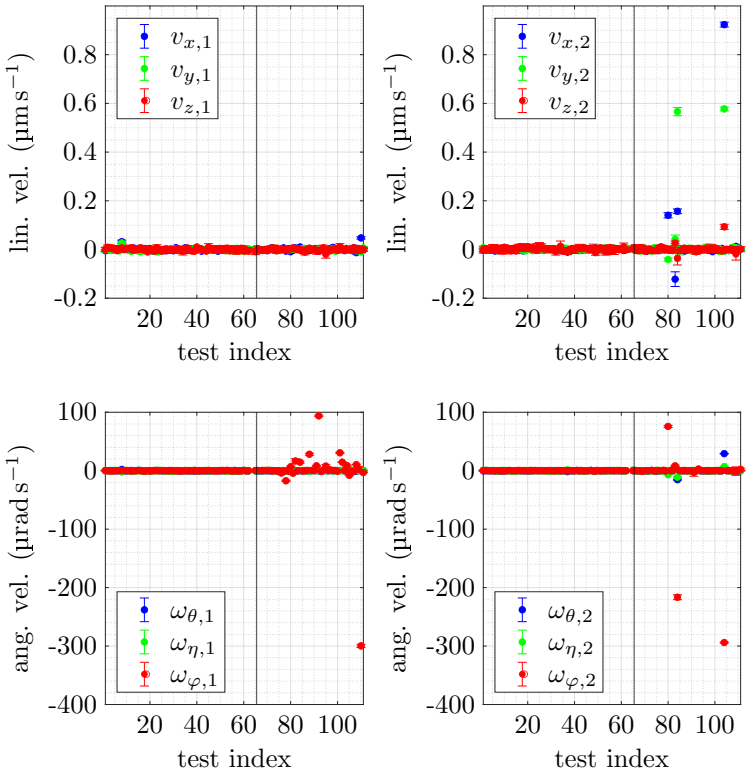

Figure 2.20: TMs linear and angular velocities in the pre-release phase for the in-flight releases from the extended mission phase. The two graphs on the left refers to the TM_1, the two graphs on the right to the TM_2. During the pre-release phase if the TM is properly held in position by a positive preload force, it remains still. In each plot, the black vertical line separates the non automated tests (index < 66) from the automated tests (index ≥ 66).

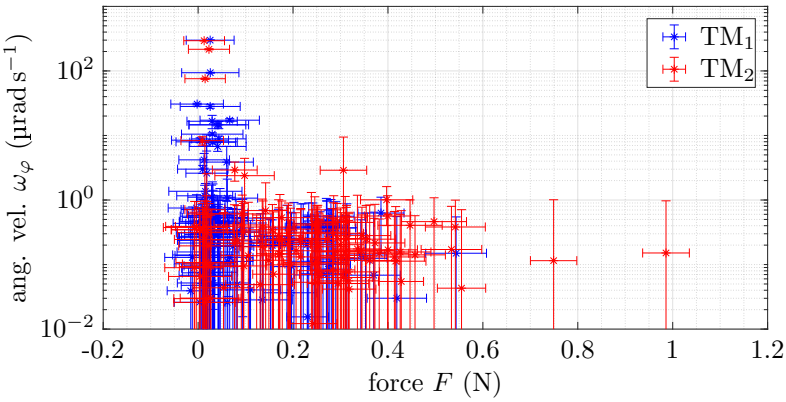

Figure 2.21: Absolute value of the angular velocity around φ of the TMs in the pre-release phase plotted against the preload force F, for all the indexed tests. Only when the preload is very low (below 0.1 N), may the angular velocity be different from zero. Moreover, all the points below 1 µrad s^{-1} have a velocity compatible with zero (error-bars go to $-\infty$ in log scale).

Now the problem is to explain what causes the TMs, especially the TM_1, to have a non-zero angular velocity about z axis before the release. A possible answer to this question is the hammering manoeuvre, which is present for any TM_1 and TM_2 automated tests only few seconds before the release. When the hammering is not performed, for both the TM the ω_φ velocity is approximately zero. When the hammering is performed, a contact between the TM indent and the plungers head may take place, producing the undesired effect. A possible explanation of why this behaviour is not seen in the TM_2 tests lays in the fact that the time interval between the end of the hammering and the actual release of the TM is greater with respect to the TM_1 case (approximately 40 s seconds and 5 s respectively).
To check the hypothesis that an impact with the pyramidal plunger can produce a ω_φ of the TM, a simple 3D contact model was build using the software Recurdyn (version V9R4). The nominal geometries of the TM and the pyramidal plunger head were imported and meshed accurately. The plunger was fixed to the ground, and the TM was set in the pre-release position (approximately 14 µm away along z direction). Then, the TM was rotated about z axis by an angle of 1000 µrad, to introduce a plausible relative angle between the TM and the plunger. An initial velocity of 30 µm s^{-1}, close to the velocity the plunger has during hammering, was given to the TM in direction z while other initial velocity components were set to zero. During the time evolution of the model, the TM collided onto the plunger head, and such a collision produced the transition of part of the linear kinetic energy to rotational kinetic energy about z axis. In other words, a collision of the plunger with the TM, in the presence of an initial relative φ angle, has the effect of producing a TM angular velocity about z axis, due to the shape of the geometries involved. The velocity obtained with the model is in the same order of magnitude of the pre-release velocity ω_φ observed in-flight, i.e., approximately 1×10^2 µrad s^{-1}.

The simple model described explains the observed dynamics after the hammering for some of the tests. This dynamics constitute a critical aspect of the GPRM, since if the TM velocity before the release is large, the electrostatic force control loop may not be able to capture it preventing impacts even if the other velocity components are within the requirements.

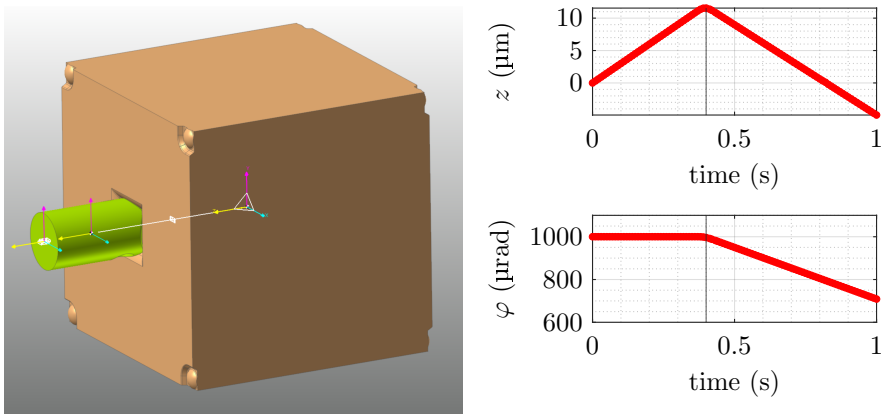

(a) (b)

Figure 2.22: On the left, model developed in Recurdyn to verify the hypothesis that an impact with the pyramidal plunger can generate a TM φ angular velocity. The plunger (green body) is fixed to the ground, and the TM is set 14 µm away along z direction and tilted by 1 mrad. An initial velocity v_z 30 µm s^{-1} is assigned to the TM. On the right, time evolution of the TM z and φ DOFs. The impact, taking place at 0.4 s (vertical black line), is followed by a non-zero ω_φ.

2.6 The GPRM release performance

In the previous Section, the pre-release state of the TM was discussed, highlighting some problems related to this phase. In this Section, the release phase itself is analyzed.

The analysis of the release performance of the GPRM starts from the computation of the impulses received by the TM at the release. The first step was to build the simplest possible model describing the release impulses on the TM. The model built for this calculation is based on the linear system of the TM dynamics, obtained by the Newton-Euler equations written in their impulsive form (System of Equations 2.9). The main hypothesis of this simplified model is that all the forces arising at the release between the TM and the GPRM end-effectors are located in the center of the landing areas. According to the nominal release procedure, these areas should be the only ones where there is a contact (i.e., a force), at least for the tip retraction tests. Moreover, another assumption of the model is that the impulses are simultaneous on both sides of the TM. Unfortunately, the low sampling frequency discussed in Section 2.3 makes it impossible to disentangle the

contribution to the TM residual velocity of a time lag in the retraction of the two tips. In fact, even a few tens of microseconds time lag is enough to convert the nominal contact preload into the maximum allowed momentum.

$$\begin{cases} +\iota_x^+ + \iota_x^- & = mv_x \\ +\iota_y^+ + \iota_y^- & = mv_y \\ -\iota_y^+ + \iota_y^- & = I_{xx}\omega_\theta/L \\ +\iota_x^+ - \iota_x^- & = I_{yy}\omega_\eta/L \end{cases} \tag{2.9}$$

In the system of Equations 2.9 the variable ι_j^f represents the impulse on the landing area in direction j (in the set $\{x, y\}$) on the TM side f (in the set $\{+, -\}$). The mass of the TM is m, and its inertia about j axis is I_{jj}. The linear velocities of the TM after the release are indicated with v_j and the angular ones with ω_γ (γ in the set $\{\theta, \eta\}$). The parameter L represents the distance between the landing areas. Parameter values are reported in Table 2.8.

Table 2.8: Numerical values of the parameters appearing in the simple impulse model of the lateral impulses received by the TM at the release.

Param.	Value	Unit	Description
m	1.98	kg	TM mass
I_{jj}	678×10^{-6}	$\mathrm{kg\,m^2}$	TM inertia about $j \in \{x, y\}$ axis
L	36.2×10^{-3}	m	Distance between the landing areas

Despite the TM having six degrees of freedom, as it is a rigid body floating in a three-dimensional space, only four equations compose the model. Indeed, this is a limit of the model coming from the hypothesis that the impulses are located only on the landing areas. Thus, the information carried by the linear and angular velocities along the z axis cannot be exploited. In fact, along z direction, the two impulses are coaxial, thus no rotation of the TM about φ can be caused.
As a consequence, the model is useful to estimate the lateral (i.e., orthogonal with respect to z axis) impulses that the TM receives, which according to the nominal release procedures should be approximately null. In order to solve the proposed model for the lateral impulses, it is necessary to compute the linear and angular components of the velocity the TM assumes after its release. Such a velocity will be referred to as *initial* velocity. The estimation of the initial velocity is non-trivial. The presence of the noise sources, discussed in Section 2.4, limits the accuracy of the estimation. In particular, the main limitation in this calculation comes from the measurement noise. Moreover, the relatively low sampling frequency (10 Hz) with respect to the time duration of possible impacts between the TM and the surroundings bodies is also a limiting factor. In order to estimate the initial velocity, a dedicated algorithm was developed. An extension and improvement of this algorithm will be discussed in Section 6.3.2. At first, by comparing the telemetry signals (tips extraction, plungers positions, force sensors and TMs DOFs) and by consulting the mission log documentation, the main phases of the injection procedure for each test are detected. For the estimation of the initial velocity, the

important phases are the pre-release and the post-release.
Given the six DOFs signals of the TM, the pre-release noise standard deviation σ_i (where i indicates the relative DOF) is computed considering the set of 20 data points immediately preceding tip/plunger retraction discussed in Section 2.5. The algorithm then searches for a set of 3 consecutive points that exceeded the $\pm 3\sigma_i$ interval in any of the DOFs signals. An extensive explanation relative to the arbitrary choice of the $\pm 3\sigma_i$ interval will be discussed in Section 6.3.2. The initial velocity components, and their relative uncertainty, are found by applying a linear fit to the set of three data points on the six TM DOFs signals. Unfortunately, for some of the tests, the computed uncertainty was predominant with respect to the estimated velocity. In other words, it is not possible to estimate the initial velocity with a reasonable accuracy. The presence of such a large uncertainty is due not only to the measurement noise but is likely caused by impacts that took place just a few tenths of a second after the release. In these tests, there does not exist a set of three consecutive points after the release which does not contain a relevant impact. An example is show in Figure 2.23. In other tests, the estimation of the initial velocity is possible with a relatively high accuracy, as shown in the example of Figure 2.24.

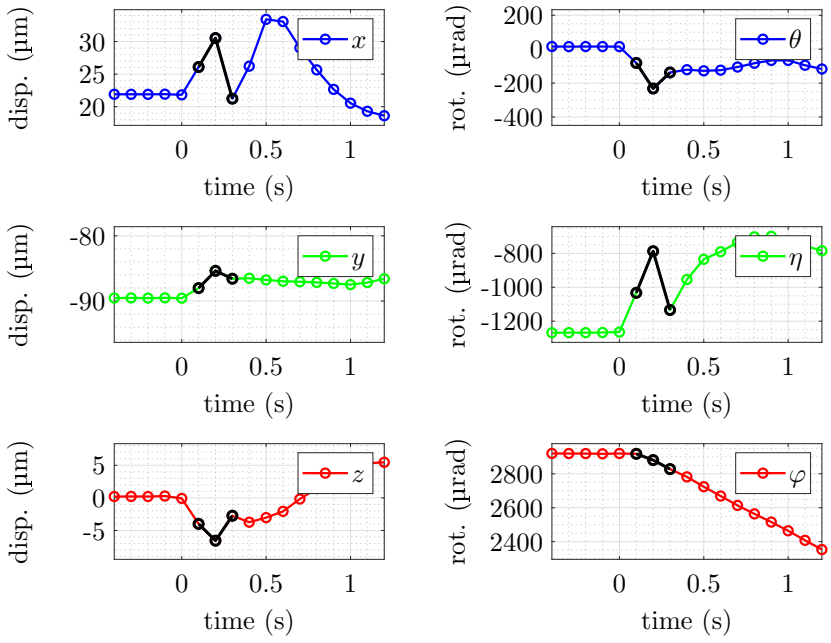

Figure 2.23: Plots of the six degrees of freedom of the TM in the neighborhood of the release instant (close to $t = 0\,\mathrm{s}$) for a non-reliable test. The set of three points, after the release, used to fit the linear model is highlighted in black. It is not possible to have an accurate estimation of the release velocity along all the degrees of freedom, because the residuals of the linear fit are large, so the uncertainty will be predominant.

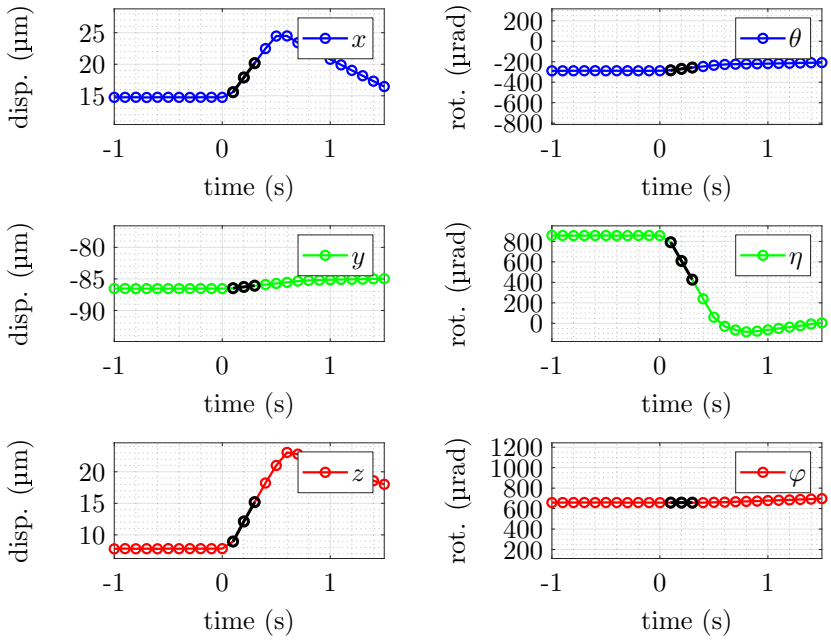

Figure 2.24: Plots of the six degrees of freedom of the TM around the release instant (close to $t = 0\,\mathrm{s}$) for a reliable test. The set of three points, after the release, used to fit the linear model is highlighted in black. The velocity along all degrees of freedom can be estimated with reasonable accuracy.

In the analysis, any collision taking place in the time interval relative to the three selected data points is detected as a diversion from the free-falling motion the TM should follow after the release. Such a deviation somehow worsens the quality of the linear fit, increasing its uncertainty. At this point, an arbitrary criterion was introduced to distinguish the high accuracy tests, called *reliable*, from the low accuracy ones, called *non-reliable*. In theory, this criterion should be based on the measurement noise.

In order to proceed with the calculation while keeping the algorithm simple, the reliability of a test is decided comparing the fit uncertainty on the velocity with the mission requirements. The idea is to consider reliable any test where the absolute uncertainty on the estimated velocity is lower than 1/5 of the requirement or the relative uncertainty is lower than 20%. The probability of detecting relevant impacts even by fitting only three points is enforced by the fact that those conditions need to be satisfied simultaneously by all the six DOFs signals. A more formal criterion, based on the statistical probabilities of detecting an impact will be discussed in Section 6.3.2. The application of the algorithm to the in-flight data produced the results summarized in Figure 2.25, where each pie chart is referred to one of the TMs.

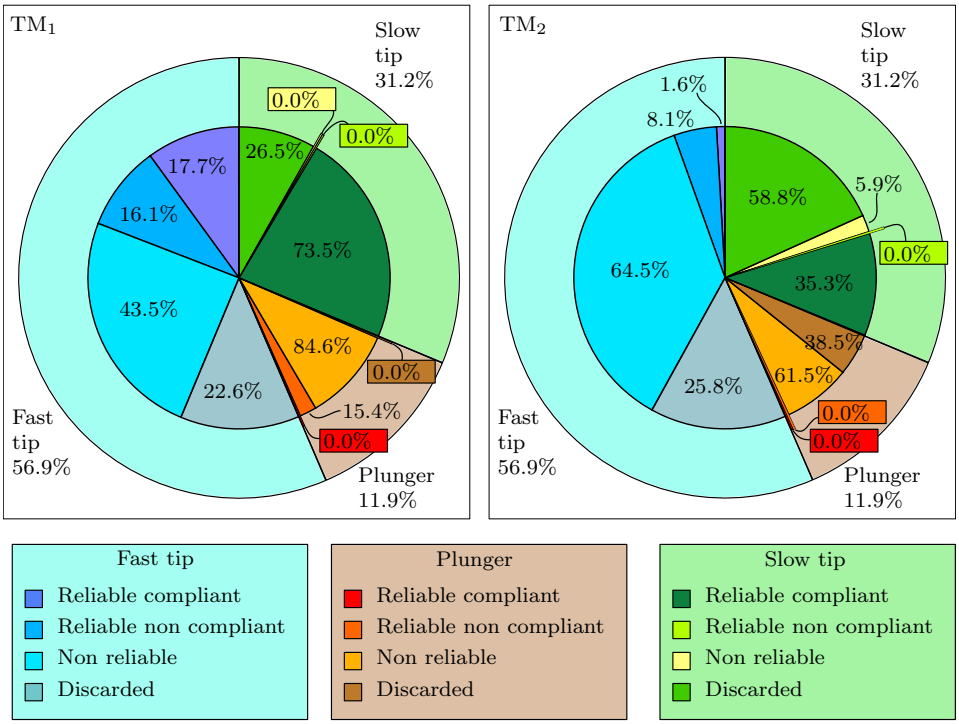

Figure 2.25: Pie charts summarizing the results of the algorithm that detects the initial velocity of the TMs and the reliability of the estimated values compared to the mission requirement. For each TM all the 109 release tests are considered in the chart.

In the chart, all the 109 (111 tests in total minus 2 adhesion tests) releases performed in the extended mission campaign are considered. As can be seen from the legend, some of the tests are discarded from the analysis, since they are affected by one or more of the following problems, that would affect the algorithm results:

- There is a non null TM velocity before the tip retraction. All the tests where the pre-release velocity, also considering its uncertainty, is greater than 1% of the release velocity requirement are discarded. In this way, in the analysis, only those tests with a negligible motion of the TM before the release are considered.

- The TM is rotated about φ by an angle greater than 4000 µrad prior to the release. Such a condition is imposed to consider only tests with a nominal TM state after the handover to the tips.

- There are artifacts in the readings, producing non physical sawtooth behaviour in the TM DOFs signals in the time interval from the pre-release phase to the end of the injection (retraction of the plungers and actuation of the electrostatic control force). This phenomenon is discussed in Section 2.4.

For each TM, the tests are subdivided into three main categories, which are I) the fast tip retraction releases (blue tone colors) composed of 62 tests, II) the plunger retraction release (orange tone colors) composed of 13 tests and III) the slow tip retraction releases (green tone colors) composed of 34. Each of these three macro sections is further subdivided in four minor sub-sectors, namely non reliable tests (indicated as *non rel*), reliable tests compliant with the requirement (indicated as *rel com*), reliable tests non-compliant with the requirement (indicated as *rel non com*) and discarded tests. A test is defined to be *compliant* if all the six components of the release velocity are within the requirements, taking into account also the fit uncertainty.
Regarding the TM_1, the reliable tests detected are a total of 48, subdivided in 25 slow tip, 21 fast tip and 2 plunger retraction tests. Regarding the TM_2, the reliable tests detected are a total of 18, subdivided in 12 slow tip, 6 fast tip and 0 plunger retraction tests. Looking at the charts, some conclusions can be drawn. In general, for both TMs, the slow tip strategy improves the reliability of the release. Almost all the non-discarded slow tip tests resulted reliable and compliant with the requirement when looking at the initial velocity. A hypothesis of what causes such a high reliability and compliance rate is probably due to the fact that the slow tip retraction does not excite the vibration of the plunger (discussed in Chapter 4). Moreover, regarding the plunger retraction tests, almost the totality resulted non reliable. This is a strong hint that, when the plungers are used to release the TM, several collisions take place. Finally, most of the fast tip tests are non-reliable, but there are a few which are reliable for both TMs.
The focus of the following analysis is on the reliable non-compliant tests performed with the tip retraction (i.e., closer to the nominal release procedure with respect to the plunger retraction tests), which are 10 for the TM_1 and 5 for the TM_2. Those tests are studied since they contain information on the main GPRM dynamics which is responsible for the violation of the requirements.
The initial linear and angular velocities of those tests are plotted in Figure 2.26, showing that the y component of the velocity of both TMs is in general much smaller than the x and z components. This suggests that the release dynamics on the x−z and y−z planes are different. Moreover, from the two graphs, it is clear that there is a different behaviour between the two TMs, i.e., the two sensors, since blue and purple arrows points in different directions.
Once the initial velocity components are computed, for the considered tests, the lateral impulses (ι_x^+, ι_y^+, ι_x^- and ι_y^-) received by the TMs are estimated applying the model of Equation 2.9 to the results. Analyzing the impulses, there are some tests where the impulse on one landing area (−z or +z) is much greater than the impulse on the other landing area (which is compatible with zero). The tests showing this dynamics are defined as *one-sided* tests. It can be stated, accordingly to the model results, that in the one-sided tests only one unit of the GPRM contributed to the lateral impulses that the TM received. Under this reasonable assumption, the lateral linear components (x and y) of the total impulse can be compared with the z component of the total impulse (i.e., the TM z linear momentum). The TM linear momentum of the fast tip non-compliant one-sided tests that had a mainly planar release dynamics ($|\iota_x| \gg |\iota_y|$ or $|\iota_y| \gg |\iota_x|$) are plotted in Figure 2.27. The orthogonality of the impulses with respect to the indent surface is a strong hint of

the fact that the plungers collided with the TM at the tips retraction. Conversely, it is not compatible with an interaction limited to the nominal tip-TM contact taking place exclusively on the landing area.

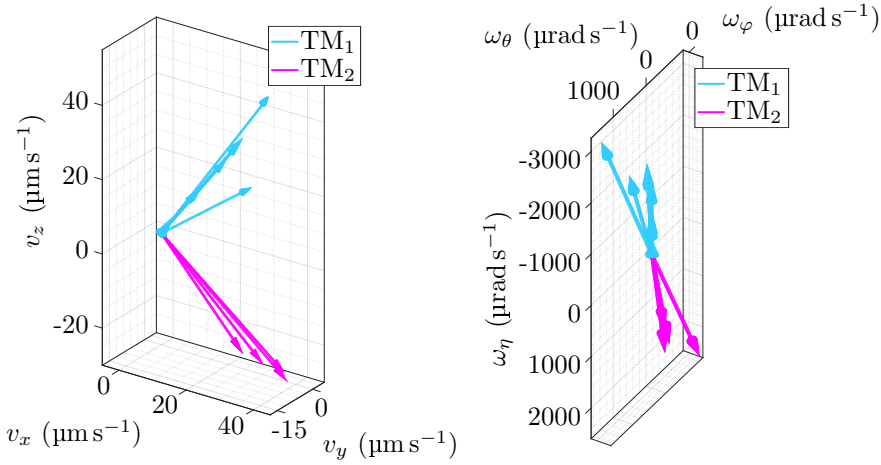

(a) (b)

Figure 2.26: TM linear (on the left) and angular (on the right) initial velocity components for the reliable non-compliant tests. The linear components lay mainly in the x−z plane, while the angular velocity is predominant about η.

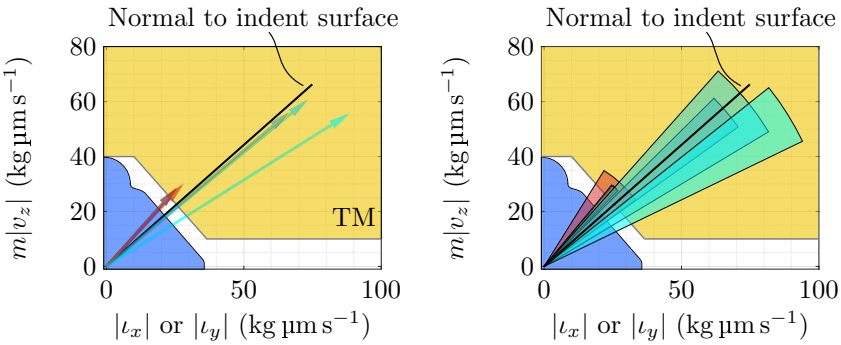

(a) (b)

Figure 2.27: Main components of the total impulse received by the TM at the tip retraction for the one-sided tests. On the left there are the estimated impulses, on the right, their uncertainties. The impulses are almost parallel to the normal direction of the indent surface, enforcing the hypothesis of an unpredicted TM-plunger interaction taking place at the release.

2.6.1 Advanced impulse model

The simple impulse model discussed in the previous section suggests that an interaction between the TM and the plunger is responsible for the un-expected release dynamics. Thanks to this interpretation, an advanced impulse model was developed assuming that TM-plunger impacts took place at the release. The model, composed by the system of Equations 2.10, relates the lateral impulses (x and y directions) with the TM momentum along z (numerical values of the model parameters are listed in Table 2.9).

$$\begin{cases} +\iota_x^+ + \iota_x^- & = mv_x \\ +\iota_y^+ + \iota_y^- & = mv_y \\ (-\iota_y^+ + \iota_y^-)(a + b\tan\alpha) & = I_{xx}\omega_\theta \\ (+\iota_x^+ - \iota_x^-)(a + b\tan\alpha) & = I_{yy}\omega_\eta \\ (|\iota_x^-| + |\iota_y^-| - |\iota_x^+| - |\iota_y^+|)\tan\alpha + \iota_z^{\text{res}} & = mv_z \end{cases} \tag{2.10}$$

This is done considering the geometry of the TM indents and imposing the orthogonality of the impulses, which was suggested by the one-sided tests (Figure 2.28). In this way ι_z^{res}, the residual impulse along z, can be computed. It contains all the effects along z direction than are not explained by the projection of the lateral impulse caused by the plungers. It is difficult to estimate all the effects that caused the residual impulse ι_z^{res}. In general, it includes the effects of the adhesion phenomenon, the contact preload, the retraction delay and a z directed pushing effect of a plunger.

Table 2.9: Numerical values of the parameters used in the advanced impulse model, that are added to the ones already used in the simplified impulse model. The values are estimated from the CAD model of the TM and the plunger heads.

Param.	Value	Unit	Description
a	21.8	mm	Distance of the estimated TM-plunger contact point from the plane x−y
b	3.9	mm	Distance of the estimated TM-plunger contact point from the planes x−z or y−z
α	41.5	°	Inclination of the TM indent contact surfaces with respect to the z axis
I_{jj}	678×10^{-6}	kg m^2	TM inertia about $j \in \{x, y\}$ axis
m	1.98	kg	TM mass

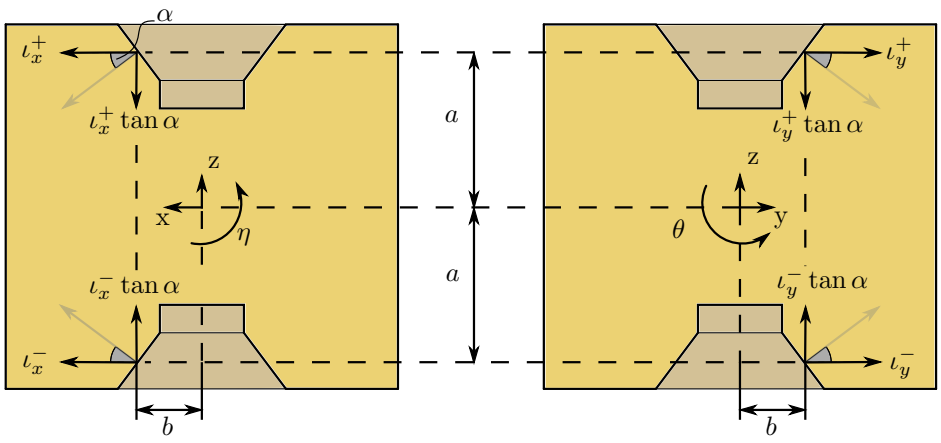

Figure 2.28: Scheme of the advanced impulse model. Any lateral impulse contributes also to the TM linear momentum along z. This is done by imposing the orthogonality of each impulse to the relative TM indent surface.

The lateral impulses, computed with the advanced model, of the reliable non-compliant tests are shown in Figures 2.29 and 2.30. From these graphs, the different behaviour of the $GPRM_1$ and $GPRM_2$ is clearly observable. In the $GPRM_1$, the x component of the pyramidal plunger impulse (ι_x^-) is the dominant one. In the $GPRM_2$, the x component of the conical plunger impulse (ι_x^+) is the dominant one.
Regarding the z direction, the residual impulse ι_z^{res} was computed for the same tests. Its value is lower than the momentum of the TM along z for all the tests, even when the initial velocity is much greater than the requirement. Thus, accordingly to the model, the TM release dynamics of the reliable tests can be almost totally explained by collisions between the TM and the plungers taking place at the tip retraction. Avoiding TM-plunger collision, the mass would likely be controllable by the actuation force without further impacts since the residual impulse (green columns in Figure 2.31) are below or very close to the requirement ($10\,\text{kg}\,\mu\text{m}\,\text{s}^{-1}$) most of the times (except in one case). This result is in line with the 1-g on ground testing which concluded that the adhesion contribution, included in the residual impulse, albeit being significant, is not expected to produce excessive momentum on the TM in the majority of the cases (see Section 1.3).
The dynamical model, when applied to the non-reliable non-compliant tests, suggests the same conclusions, even if with larger uncertainty. In general, also for the non-reliable non-compliant tests, the TM dynamics is much different than the expected mono-dimensional motion along z. For the compliant fast tip tests, which are in most part reliable, the application of the dynamical model shows that the effect of the lateral impulses on the total z momentum is reduced, thus proving that a compliant dynamics is closer to the nominal case. This can be seen in Figure 2.32, where the difference between ι_z^{res} and mv_z is much smaller with respect to the non-compliant tests.

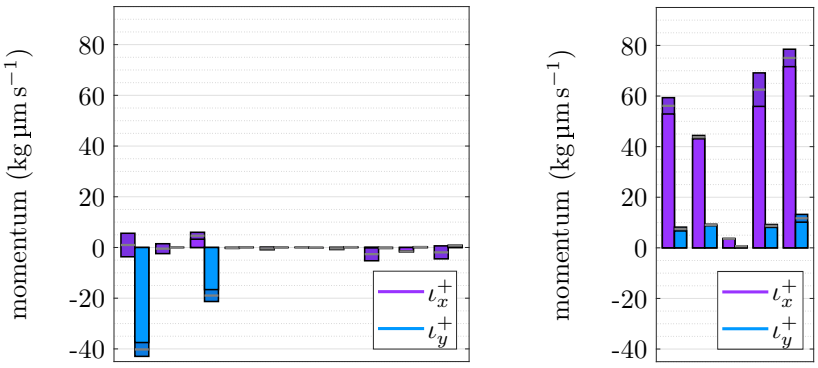

(a) TM_1 (b) TM_2

Figure 2.29: Reliable non-compliant tests. Comparison between the TMs release impulses on the +z side (conical plunger). Blue columns represent the impulse in the y direction, while purple columns the impulse in the x direction. Each pair of columns represent a single test. For each column, the nominal value is indicated by the gray line and the 3σ uncertainty is represented by the colored rectangle around it.

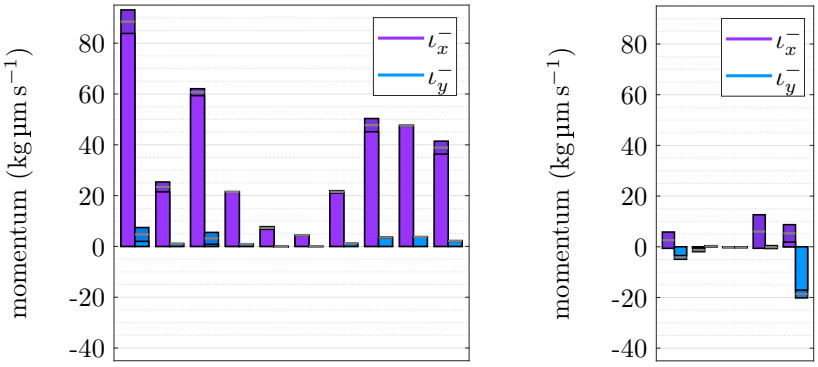

(a) TM_1 (b) TM_2

Figure 2.30: Reliable non-compliant tests. Comparison between the TMs release impulses on the −z side (pyramidal plunger). Blue columns represent the impulse in the y direction, while purple columns the impulse in the x direction. Each pair of columns represent a single test. For each column, the nominal value is indicated by the gray line and the 3σ uncertainty is represented by the colored rectangle around it.

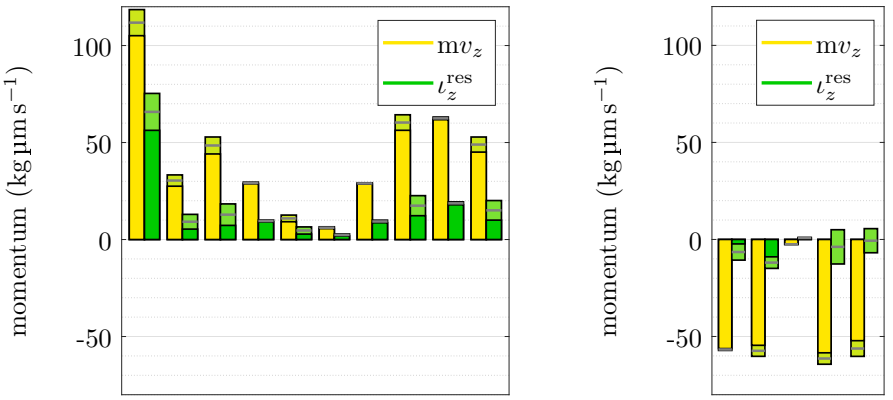

(a) TM$_1$ (b) TM$_2$

Figure 2.31: Reliable non-compliant tests. Comparison between the TMs linear momentum along z (yellow columns) and the residual impulse (green columns) computed from the improved model of the release dynamics. Each pair of columns represent a single test. For each column, the nominal value is indicated by the gray line and the 3σ uncertainty is represented by the colored rectangle around it.

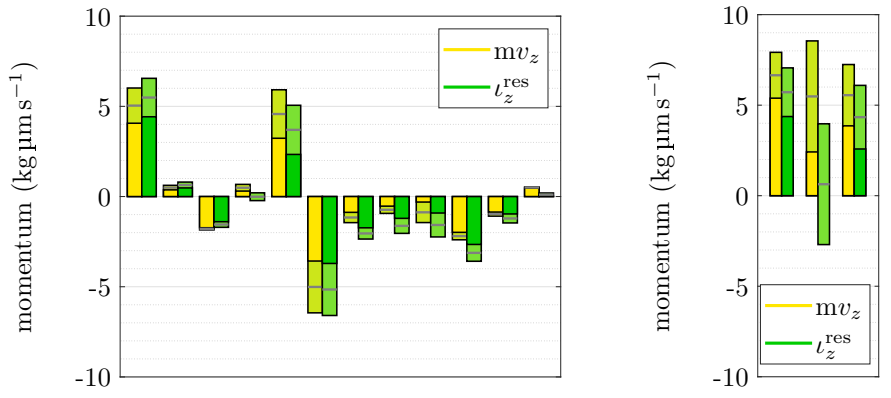

(a) TM$_1$ (b) TM$_2$

Figure 2.32: Reliable compliant tests. Comparison between the TMs linear momentum along z (yellow columns) and the residual impulse (green columns) computed from the improved model of the release dynamics. Each pair of columns represent a single test. For each column, the nominal value is indicated by the gray line and the 3σ uncertainty is represented by the colored rectangle around it.

2.6.2 TM dynamics at the plunger retraction

In the previous Section the release dynamics at the tip retraction has been analyzed. The tests with a reliable estimation of the release velocities and high TM momentum (i.e., high kinetic energy) at the tip retraction (reliable non-compliant tests) have been interpreted through a model, showing that the high momentum is mainly due to the plunger-TM contacts at the indentation surfaces. This means that the TM release at the tip retraction is not nominal and the contacts between the plunger and the TM are extremely critical.
We highlight here a second deviation from the nominal procedure: additional kinetic energy is sometimes acquired by the TM when the plungers are retracted, a few seconds after the tip retraction. The hypothesis is that an additional TM-plunger contact takes place due to non-perfectly straight motion of the plunger when retracted. The dynamics of the TM-plunger interaction at the retraction of the plunger is more complex than the dynamics at the tip retraction. First, the actuator involved in the plunger retraction (piezo-walk) also provides the guiding function of the plunger on the y−z plane, while on the x−y plane a roller-slider bearing is adopted. Second, the identification of an impact cannot be performed by looking for a deviation from constant signals on the six degrees of freedom but requires the identification of two different free-falling states. Third, a single change of the free-falling state is hardly detectable in the telemetry signals at the retraction of the plungers, where probably more impacts occur in a reduced timescale.
As a consequence, the study of the TM dynamics is limited to the kinetic energy, identifying the two constant levels which characterize its state after the tip retraction and after the plunger retraction. Even though the accuracy of the estimation is limited to the order of magnitude, some interesting comments can be realised. Figure 2.33 shows the relation between the kinetic energy at the tip release (K_{tip}) and the kinetic energy at the plunger retraction (K_{pl}), for all the tests (independently of the reliability). For each axis, the kinetic energy is normalized with respect to the maximum compliant kinetic energy $K_{\max}$, which is computed as shown in Equation 2.11. The values of the linear and angular residual velocities v_{req} and ω_{req} are set as listed in Table 1.2, and the mass and inertia of the TM are reported in Tables 2.8 and 2.9.

$$K_{\max} = \frac{3}{2} m_{\text{TM}} v_{\text{req}}^2 + \frac{1}{2}(I_{xx} + I_{yy} + I_{zz})\omega_{\text{req}}^2 \tag{2.11}$$

Important considerations are drawn from the graphs. The TM_1 slow tip tests produce a $K_{\text{tip}}/K_{\max}$ with maximum value around 2×10^{-2} (cyan dots in Figures 2.33a and 2.33c). When not performing the hammering, which is the case of the slow tip tests of Figure 2.33a, the dots are concentrated in a narrow band close to the maximum value. Performing the hammering, which is the case of all the tests represented in Figure 2.33c, allows to reach lower values of K_{tip} ($\approx \left[10^{-4}, 10^{-2}\right] \cdot K_{\max}$), indicating that the hammering sometimes has a positive effect on the release kinetic energy.
Based on the TM-plunger interaction model, the very low K_{tip} value in the slow tip tests may be explained by the fact that the slow retraction of the tip reduces the plunger oscillations and smoothly decreases the preload force on the TM.
Regarding the K_{pl} of the slow tip tests of TM_1, it is greater than K_{tip} in almost

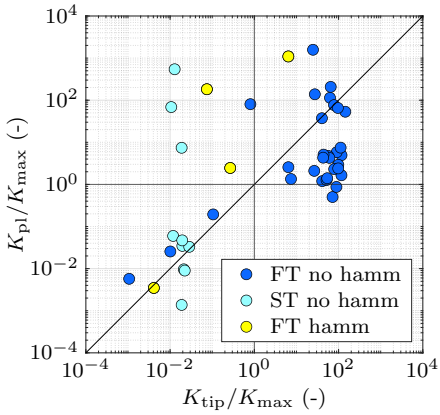

(a) TM_1 Nominal plunger retraction

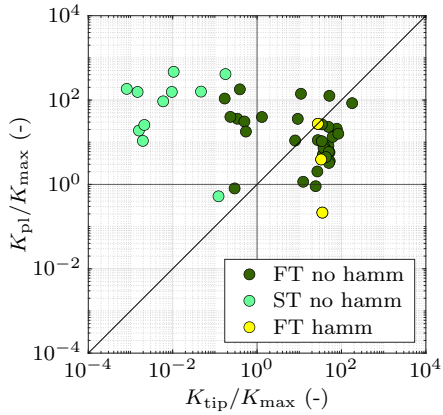

(b) TM_2 Nominal plunger retraction

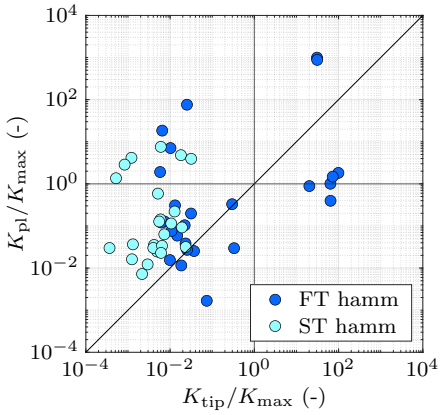

(c) TM_1 Slow plunger retraction

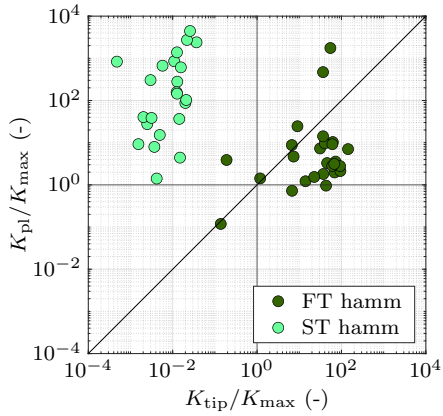

(d) TM_2 Slow plunger retraction

Figure 2.33: Relation between the TM kinetic energy at the tip release and the kinetic energy at the plunger retraction. Graphs (a) and (b) represent the nominal plunger retraction tests, while graphs (c) and (d) represent the slow plunger retraction tests. In the legend, FT stands for Fast Tip, ST for Slow Tip and hamm/no hamm indicates whether or not the release is preceded by the hammering.

all case, meaning that the TM acquires kinetic energy at the plunger retraction. When the plungers are retracted slowly (Figure 2.33c), the K_{pl} presents a lower dispersion ($\approx \left[10^{-2}, 10^{1}\right] \cdot K_{max}$) than when the plungers are retracted with nominal velocity ($\approx \left[10^{-3}, 10^{3}\right] \cdot K_{max}$, Figure 2.33a), meaning that the slow plunger retraction slightly improves the repeatability of the K_{pl} and reduces the maximum kinetic energy transferred to the TM.

The values of $K_{\text{tip}}/K_{\max}$ for the fast tip retraction test of TM_1 (blue dots in Figures 2.33a and 2.33c) are roughly concentrated around the two values 10^{-2} and 10^{2}. In particular, when the hammering manoeuvre is not executed, i.e., almost any test of Figure 2.33a (the yellow dots represent the unique exception), the blue dots are concentrated around 10^{2}, while in Figure 2.33c the majority of the dots are grouped around 10^{-2}, confirming that the hammering manoeuvre has the positive effect of reducing the initial kinetic energy of the TM. Moreover, when K_{tip} is low, the TM tends to acquire kinetic energy at the plunger retraction, reaching high values even if plungers are retracted slowly. In contrast, when K_{tip} is high, K_{pl} is in general lower than K_{tip}, meaning that some dissipative phenomena take place in between the TM release and the plunger retraction. In this case, the plunger retraction results less critical than the tip retraction.
Now we will focus on the TM_2 tests, represented in Figures 2.33b and 2.33d.
The slow tip tests (light green dots) generate a $K_{\text{tip}}/K_{\max}$ spanning the range from 10^{-3} to 10^{-1}. The tests of Figure 2.33b, where hammering is not performed most of the times, are more dispersed if compared to the corresponding tests of the TM_1, grouped around 10^{-2} (2.33a). Executing the hammering manoeuvre (majority of the tests of Figure 2.33d) still limits the dispersion of K_{tip} ($\approx \left[10^{-4}, 10^{-2}\right] \cdot K_{\max}$), resulting in a range similar to the TM_1.
The K_{pl} of slow tip tests are critical. In those tests, when the plungers are retracted, the TM always acquires a high kinetic energy, so $K_{\text{pl}} > K_{\text{tip}}$, no matter what the plunger retraction velocity was.
In particular, the dispersion of K_{pl} in the nominal plunger retraction tests (Figure 2.33b) ranges from 10^{1} to 10^{3}, while in the slow plunger retraction tests (Figure 2.33d) the dots are more dispersed and higher values of K_{pl} are reached ($\approx \left[10^{0}, 10^{4}\right] \cdot K_{\max}$). This is unexpected, since the slow plunger retraction, which improved the performance of the GPRM_1, seems worsening the performance of the GPRM_2.
In the fast tip tests (dark green dots), the TM_2 is released generally with a high K_{tip} (about $10^{2} K_{\max}$), and there are no noticeable improvements given by the hammering manoeuvre (Figure 2.33d). The nominal plunger retraction tests (Figure 2.33b) produce a K_{pl} that is greater than K_{tip} when the latter is below $K_{\max}$; when K_{tip} is greater that the requirement, K_{pl} is in general lower than the tip release kinetic energy, meaning that some dissipative phenomena take place.
Regarding the slow plunger retraction tests (Figure 2.33d) the majority of the dots are under the bisector, meaning that $K_{\text{pl}} < K_{\text{tip}}$. There are few exceptions of tests where K_{pl} reaches high values, up to $10^{3} K_{\max}$, close to the K_{pl} of the slow tip tests.
It is worth mentioning that, thanks to the changes adopted to improve the GPRM performances, one of the automated releases of the TM_1 produced similar results to the nominal case (see Figure 2.34). In this test, which is reliable and almost compliant, the TM did not receive noticeable impacts after the tips retraction event. Moreover, the electrostatic force was able to stabilize and move the TM towards the center of the EH, as can be observed looking at the trend of the TM DOFs trajectories.

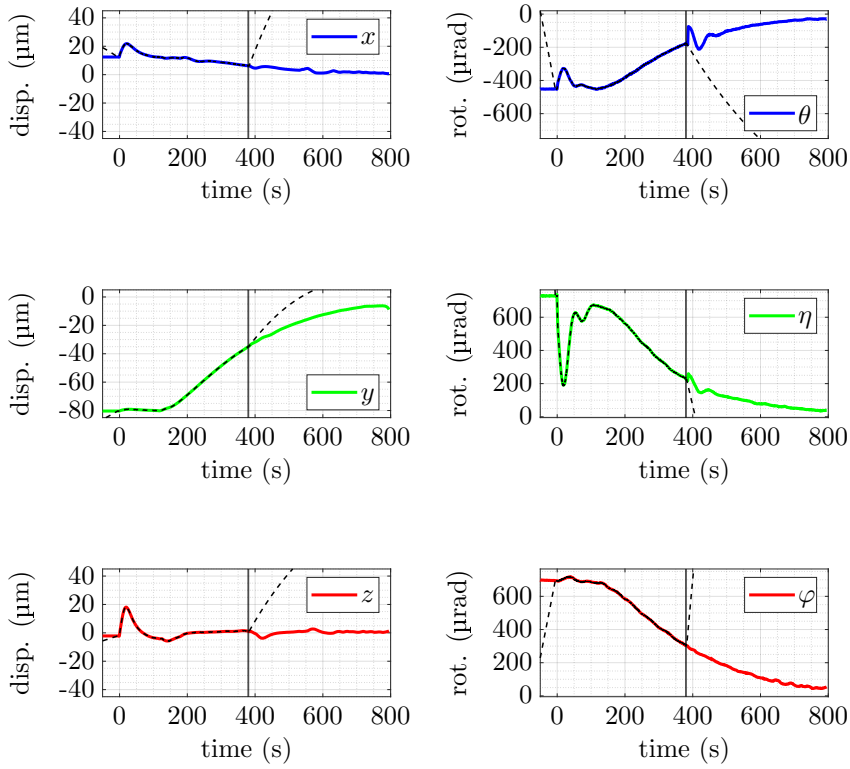

Figure 2.34: Plots of the six degrees of freedom of the TM after the release instant (close to $t = 0\,\mathrm{s}$) for the in-flight test closest to the nominal case. The test is reliable, almost compliant, with no TM-plunger impacts at the plunger retraction. The action of the control force stabilizes the TM and drives it towards the center of the EH. The colored lines represents the 1 Hz signals. The dashed line the 10 Hz. Small oscillations, not corresponding to a real TM motion, are visible in some of the signals right after the 10 Hz acquisition is deactivated (vertical black line).

Chapter 3

The hypothesis of TM-plunger collision

In Chapter 2 the criticalities of the release dynamics were identified in the unexpected contact between the TM and the plunger. In this Chapter the focus is on the possible factors which affect the nominal gap between the TM indent surfaces and the plunger heads. These factors are multiple and will be extensively described.

3.1 Factors affecting the TM-plunger clearance

The in-flight data analysis has shown that a systematic contact between the TM and the plunger is responsible for the non-compliant release dynamics. Thus, it is necessary to understand the possible factors that may have reduced the nominal TM-plunger clearance, which should be present at the release to avoid any collision. According to the nominal pre-release state, a gap in the order of 10 µm between the TM and the plunger should exist. The gap is defined as the distance between the surfaces of the TM indent and the plunger head that are in contact during the grabbing phase, preceding the handover to the tips.
In the plunger release tests, where the handover to the tips is not performed, the TM indents are in contact with the plungers at the release, which is performed by the retraction of the plungers in this case. In the tip retraction tests, the presence of the gap should be guaranteed by the extension of the tip, which should move the plunger away from the TM. After an extensive research, several factors that may have reduced the gap have been identified. The factors are subdivided into two distinct categories, *static* and *dynamic*.
Static factors, listed in the following, influence the gap before the tip retraction, when the bodies are not moving.

- Temperature variations affecting the positions of the GPRM end effectors.
- Mis-regulation of the free stroke of the tip.
- Actual maximum tip stroke.

- Tolerances affecting the geometries of the flight models components.
- Plunger non rectilinear motion.
- GPRM alignment during the integration of the mechanism.

Apart from the static factors, the dynamic factors, listed in the following, involve the motion of the bodies (plunger or TM) before or immediately after the release.

- The TM non-zero angular velocity ω_φ before the release (already discussed in Section 2.5).
- The motion of the plunger triggered by the quick tip retraction.

3.1.1 Temperature effect

The LTP is provided with many temperature sensors, needed to constantly monitor the experiment since any temperature fluctuation can crucially affect the science signals. In fact, an advanced temperature management of a satellite orbiting near the L1 Lagrange point is essential, since the satellite face exposed to the sunlight is much hotter than the faces in penumbra, creating high temperature gradients. Thus, in order to ensure the accuracy of the laser interferometry, the temperature is measured at several key locations. The picture in Figure 3.1 shows the location of the sensors on the two GRS and the optical bench. As reported in the picture, on the EH and on the laser optical bench some heaters are also attached. Those are used to induce controlled heat inputs to compute the transfer functions between the thermal perturbations and the GRS outputs ([23]). The temperature sensors used are negative temperature coefficient thermistors (model Betatherm G10K4D372, with a resistance of 10 kΩ). The heaters used are of two types, I) 45 Ω resistors on the optical bench and on the two optical windows and II) 2 kΩ resistors on the EH walls.

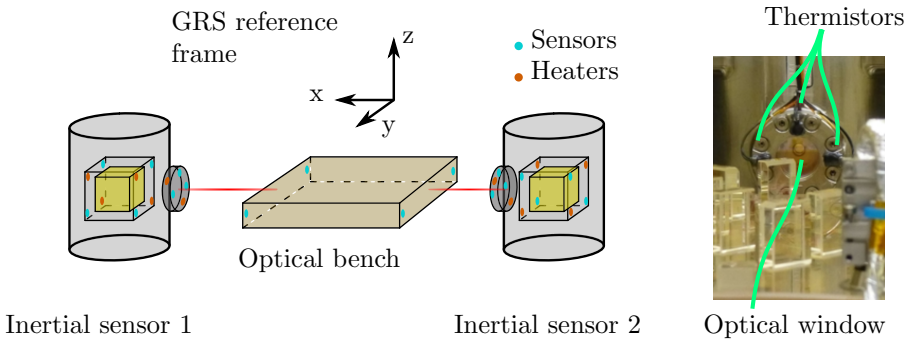

Figure 3.1: Location of the temperature sensors and the heaters used in the LISA spacecraft nearby the TMs.

In order to verify if temperature variations are correlated with the GPRM performance, the output of the four temperature sensors closest to each GRS have been analyzed. The correlation may occur if the deformation produced by the temperature of the GRS produces distortions which ultimately affect the plungers configuration. The sensor readings used to test this hypothesis are the ones on the vertices of the EHs (see Figure 3.1). Temperature data are plotted in the time frame of interest, i.e., in the dates when the in-flight tests have been performed. The Figure 3.2 clearly shows that the temperature variation is monotonically increasing both in the June test days and in the July test days. The range of temperature variation is approximately 1 °C in the June tests (from 23 °C to 24 °C) and approximately 9 °C in the July tests (from 16.5 °C to 25.5 °C).

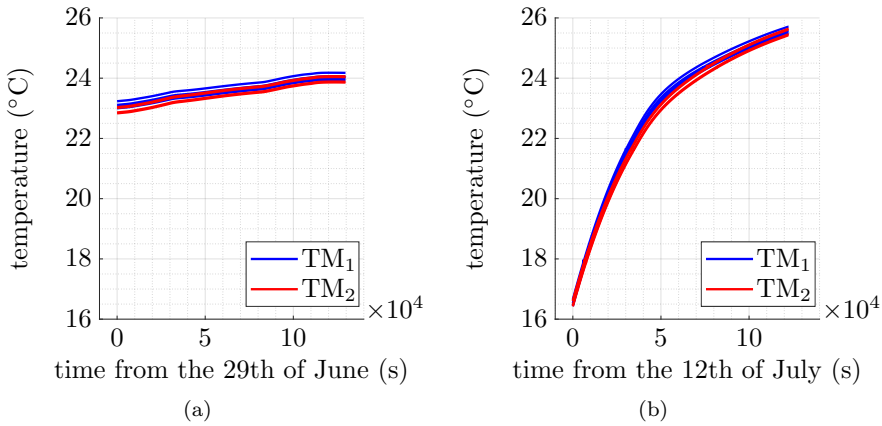

Figure 3.2: Temperature readings from the TM_1 (blue curves) and TM_2 (red curves) sensors for the June tests (left plot) and July tests (right plot). In each plot there are four curves for each TM, referring to the four sensors positioned on opposite vertices of the EH.

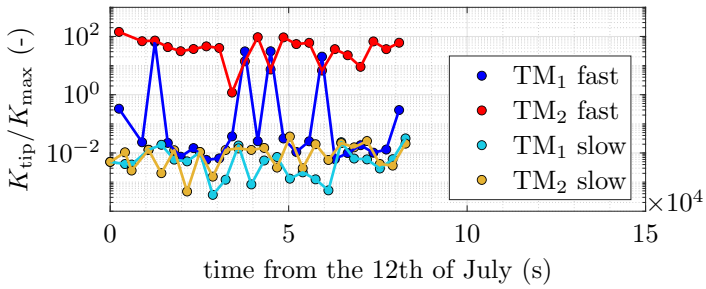

Figure 3.3: Normalized kinetic energy at the tip retraction for all the automated tests (July), as function of the release instant. No correlation is present with the EH temperature on the same days.

Analyzing the release performances of the GPRM over time, no clear correlation with the temperature emerges. In particular, for the scope of this analysis, the in-flight data of July tests are considered, exploiting the fact that I) those tests were automated, i.e., the release procedure parameters where fixed, and II) the temperature variation was significant. The mentioned tests show no monotonic behaviour, neither in terms of pre-release performance, nor in terms of post release TM kinetic energy, as shown in Figure 3.3. For this reason, it is concluded that the EH temperature variation do not significantly affect the GPRM performance, at least in the range from 16.5 °C to 25.5 °C.

3.1.2 Tip free stroke verification

In Section 1.2.3 the mechanics of a single GPRM unit was described and the concept of the *free stroke* of the tip was introduced. The free stroke of the tip corresponds to the nominal gap between the TM indent landing area and the retracted tip surface, when the TM is grabbed by the plungers, which is equal to 4 µm. The position of the retracted tip is adjusted, during the assembly of the GPRM, thanks to a fine regulation screw (differential bush) present in the bottom end of the plunger. Turning the screw allows for precise positioning, along the z axis, the series of components inside the plunger (the piezo stacks, the spacer, the tip) as a whole block.

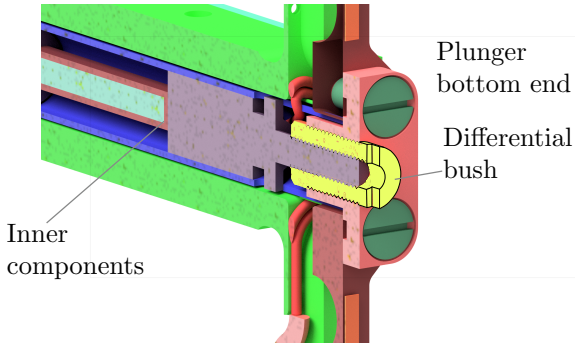

Figure 3.4: Section view of the plunger bottom end. The differential bush has two treads, one external, engaging with the plunger, and one internal, engaging with a slider inside the plunger. The slider, when moved, changes the z position of the series of internal components of the GPRM, which constitute the actual release mechanism.

An incorrect regulation of the free stroke influences the release performance of the GPRM, since it directly affects the TM-plunger gap in pre-release, i.e., after the handover to the tips. Supposing for example that the tip-free stroke is close to the maximum tip extension, then after the handover to the tips TM plunger gap will be close to 0 µm. Conversely, if the tip-stroke is close to zero, there is the risk of exerting a high pressure directly on the landing area when the TM is grabbed with the plungers. In fact, the requirement of a 4 µm landing area-tip gap is set to avoid damaging the landing area.

Apart from the differential bush, another factor that influences the free stroke is the relative angle of the TM and the plunger. Thanks to the CAD model, it was verified that, when the plunger is tilted and kept in contact with the TM indent, the tip-landing area gap slightly changes, but the variation is limited (below 0.1 µm for a relative TM-plunger angle of 1 mrad).

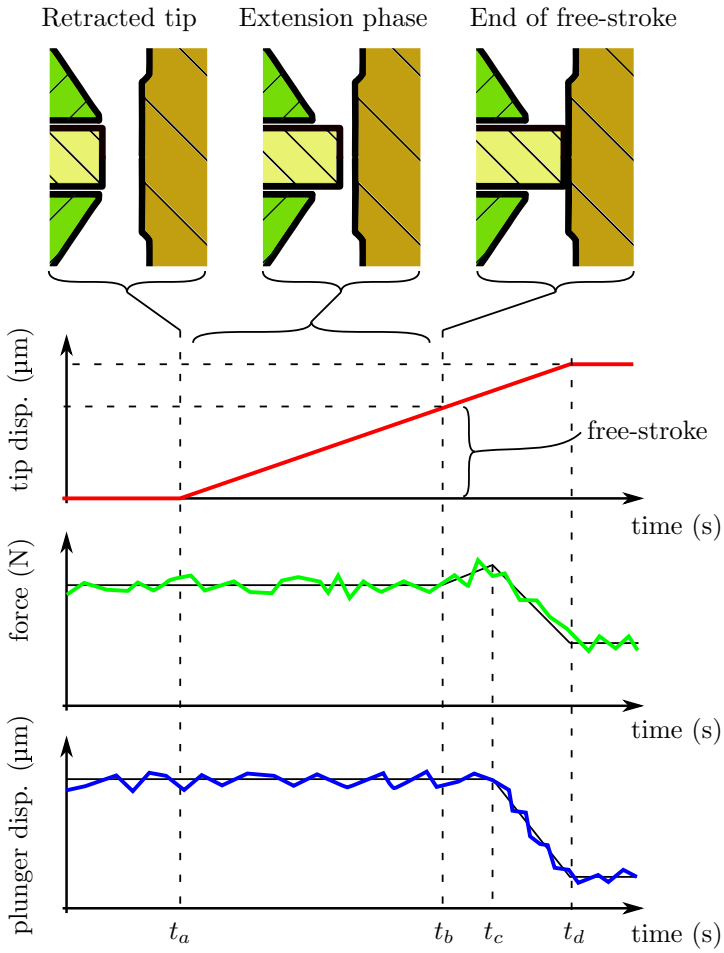

Figure 3.5: Scheme showing the principle behind the estimation of the tip free stroke from the LTP telemetry data available during the handover.

In order to verify if the tip free stroke during the in-flight releases is compatible with the nominal value, a method was found to estimate it exploiting the in-flight telemetry data. The data used are:

- The measured preload force signals of the two GPRM units.
- The measured displacement of the linear runners (i.e., the plungers).
- The commanded extensions of the two tips.

The time interval considered for the analysis is when the handover to the tips takes place. During that phase the tips are extended and the plungers retracted away from the TM. The telemetry signals of any test were manually visualized during the handover searching for those tests fulfilling the following two conditions:

- The tip extension begins before the relative plunger is retracted.
- The force is constant and positive during the initial tip extension, and increases after a while, while the plungers remain still.

Under such conditions, the distance covered by the moving tip during the initial phase of the extension, up to the point when the force starts increasing, should give an estimation of the free stroke. Before introducing the estimation process, represented in the scheme of Figure 3.5, it useful to recall that the CCU control loop is designed to maintain the preload force approximately constant during the handover even if some force variations are presents. At the instant t_a, the tip starts moving towards the TM, while the plunger is still. Due to the presence of the free stroke, the force will remain constant until the tip touches the landing area (instant t_b). The free stroke is estimated as the extension of the tip in correspondence of the instant t_b. At the instant t_c, the plunger is retracted from the control loop, preventing an excessive increase of the preload force. Up until the full tip extension is reached (instant t_d) the tip and the plunger keep moving in opposite directions. From all the tip retraction tests, only 8 fulfilled the two aforementioned conditions (four for each TM). Those tests are all from the non-automated set of in-flight experiments. In the other tests, either the preload force was compatible with zero, or the plunger started moving before the force increased. The estimated free stroke is compatible with the nominal 4 µm for all the eight tests, with an uncertainty of ± 1 µm.
In conclusion, the result of the analysis is that there is no evidence from the in-flight telemetry that the tip free stroke was significantly different from the nominal value of 4 µm, so it should not have affected the TM release dynamics.

3.1.3 Maximum tip stroke

The maximum tip stroke, similarly to the free stroke, affects the gap between the TM indent and the plunger head surfaces, since it determines their relative distance along z. The maximum tip stroke is equal to the maximum elongation of the piezo-stack that extends the tip during the handover. Such a value is reached when the piezo is supplied with 120 V, which is the case of the nominal injection procedure. From the specification of the piezo-stack, such a voltage difference should produce an elongation of $18\,\mu m \pm 3.6\,\mu m$ (the 20% relative uncertainty is due to the manufacturing process). When the GPRM units were tested on-ground by RUAG, prior to their integration into the GRSs, the tip stroke was measured with a laser interferometer. Several units of the GPRM were measured, both qualifying models (QM), engineering qualifying models (EQMs) and flight models (FMs). In any of the tested units, the actual tip stroke was inside the $\pm 20\%$ interval, except for an EQM where the value was off by 22%. The problem is that every unit tested showed a value significantly lower than 18 µm with a mean value of approximately 15.5 µm. Part of the experimental data produced by RUAG are depicted in

Figure 3.6, showing the motion of the tip for the four flight models ($GPRM_1$ +z, −z and $GPRM_2$ +z, −z). It is worth mentioning that the tip motion, although always on the lower side of the ±20% interval, was highly repeatable. This same behaviour of the tip retraction, repeatable and with approximately 15.5 µm stroke, was measured also during the on-ground testing on the GPRM EQMs performed in the laboratory of Space Applications of the University of Trento. Further details on the experiment will be discussed in Chapter 4.

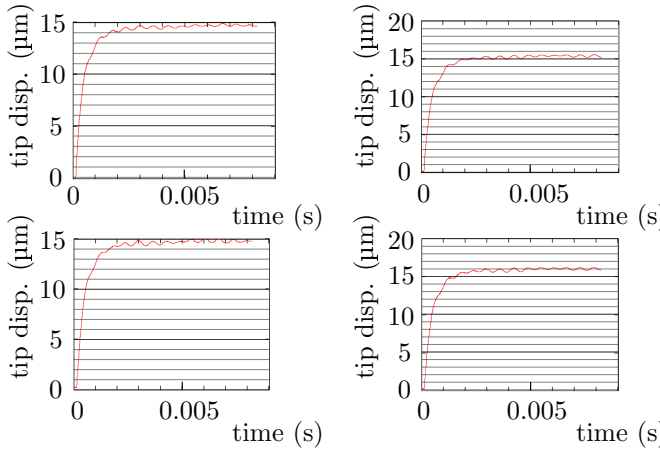

Figure 3.6: Experimental curves of the tip retraction on the four flight models units of the GPRM. The tip z motion is measured with a laser interferometer. The tip stroke (steady state values) is within 14.5 µm and 16 µm approximately. Courtesy of RUAG Space.

With a tip stroke significantly lower than 18 µm, the gap between the TM and the plungers at the pre-release phase are reduced with respect to the nominal case as listed in Table 3.1. The clearance along any direction, which can be interpreted as the maximum linear offset (or angular misalignment) that the plunger may have, is computed from the 3D CAD model, moving the plunger from the nominal position along one linear or rotational DOF until it interferes with the TM indent. As can be seen from the table, the reduction of the available gap is significant when taking into account the actual tip stroke. Moreover, it is important to notice that any combination of two or more offsets/misalignments (along different DOFs) will lower the clearances even further. Thus, such an effect is certainly one of the factors contributing to the unexpected TM-plunger collisions during the injection phase.

Table 3.1: Value of the clearance between the TM indent and the pyramidal plunger head in pre-release conditions.

Tip stroke	x (µm)	y(µm)	z(µm)	θ(µrad)	η(µrad)	φ(µrad)
Nominal (18 µm)	≈12.4	≈12.4	≈14.0	≈ 1600	≈ 1600	≈ 4800
Effective (15 µm)	≈ 9.7	≈ 9.7	≈11.0	≈ 1300	≈ 1300	≈ 3600

3.1.4 Machining tolerances

It is obvious that machining tolerances of the components are an important factor in determine the actual TM-plunger clearance. Their contribution is significant since the clearance is small (in the order of 10 µm) even assuming a perfect alignment and nominal geometries of the involved bodies. For this reason, the FM pyramidal plunger and TM indentations have been measured and compared to the nominal geometry by Astrium EADS (now Airbus Defence and Space). It is difficult to understand the effect of geometry deviations in the reduction of the gaps, due to the complexity of the involved surfaces. The measurements reported by Astrium are:

- One of the FM test mass indents presents a maximum measured deviation with respect to the nominal surface of 2 µm.
- FM_1 and FM_2 pyramidal plungers, in the contact zones, present some deviations with respect to the nominal geometry.

These deviations are in the range of 10 µm to 36 µm for FM_1 and in the range of 67 µm to 137 µm for FM_2.
Since the tip free stroke is adjusted to 4 µm when assembling the GRS, the gap along the z axis should not be influenced by machining tolerances. On the other hand, gaps along other axes should be affected.

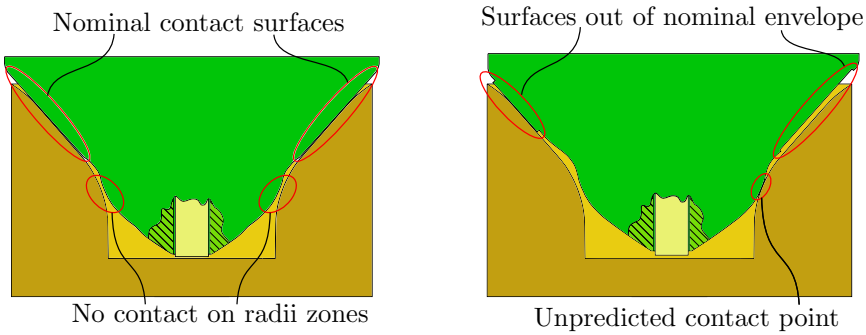

Figure 3.7: On the left, nominal pre-handover conditions (after the TM is grabbed and possibly repositioned), with perfect geometries and perfect relative alignment of TM and plunger. The surfaces are in contact where they are flat. On the right, case of non-perfect plunger inserted in a nominal indent geometry. Unexpected contacts may take place, for example in the radii zone of the plunger.

A probable effect of these deviations is the reduction of the gap between the plunger and the TM at the radii zone, due to the wrong position of the contact surfaces in a reference frame fixed to the plunger. After taking the measurements, the grabbing configuration is studied in a 2D CAD model. As shown in 3.7, the measured plunger is not fitting the nominal TM indent touching the dedicated interface surfaces.

3.1.5 Plunger non-ideal motion

The linear runner, as explained in Section 1.2.2, is the body which drives the plunger along the z axis. Ideally, the plunger moves in a straight line when the linear runner is actuated by the NEXLINE. In reality, the motion presents some deviations from the straight line. For this reason, the plunger motion deviations produced while actuating the NEXLINE have been analyzed on ground, prior to the mission. Experiments showed that the plunger rotates itself about angle η when its direction of motion is reversed and also angles θ and φ vary when repositioning the TM. Thus, such a phenomenon happens also during the handover to the tips when the plungers are retracted by approximately 10 µm.
This behaviour generates some sort of bi-stable configuration of the plunger, related to its direction of motion, especially in the x−z plane, which is where most of the release impulses lie. The bi-stability is probably caused by the side guiding mechanism of the linear runner and by the way in which the piezo-stacks of the NEXLINE generate the force producing the motion of the linear runner. In Table 3.2, which is taken from a mission technical note from RUAG, a summary of the different side guiding systems performance is shown. As can be read, the *slider/roller*, used in the flight models of the GPRM, presents a high risk of plunger recontact with the TM after the release.

Table 3.2: Overview of the performance of different side guiding systems for the linear runner. The slider/roller, highlighted in red, is the one adopted for the FMs.

Side guiding system	Risk of change of alignment during launch	Release position repeatability	Risk of re-contact during pass-over process	Risk of re-contact after release
Slider/roller	*none*	*poor*	*moderate*	*high*
Roller/roller	*high*	*very poor*	*moderate*	*high*
Ceramic ball bearings	*high*	*very good*	*low*	*low*

A bi-stable behaviour of the plungers has been detected also analyzing the in-flight data. In particular, the TM repositioning tests of the 9th of July 2017. The tests were carried out grabbing the TM and moving the plungers back and forth by ±200 µm while maintaining a preload force of approximately 2 N (see Figure 3.8). Ideally, the resulting motion of the TM should be only along z (time history plotted in Figure 3.9) but in reality, all the six degrees of freedom of the TM were affected by the repositioning.
Figure 3.10 shows the correlation between each DOF with the z position of the TM during the repositioning test. The signals are plotted with zero mean and the time history is expressed by the same color gradient of Figure 3.9, to facilitate the comparison of the plots. The x coordinate of the TMs seems not to significantly depend on its z position, while the angles η_1 and η_2 show a hysteresis cycle. The rotation of the TM in the x−z plane, for both sensors, strongly depends on the direction of motion of the NEXLINE. At any inversion of motion, there is a jump of approximately 60 µrad, while during the constant velocity repositioning there is

a limited linear correlation $\eta \approx k\,z$, with $k \approx 0.1\,\mu\text{rad}\,\mu\text{m}^{-1}$. On the y−z plane the mechanism behaves differently. The linear DOFs y_1 and y_2, as well as the angular DOFs θ_1 and θ_2 have a correlation with the z position of the TMs, but show no jumps at the inversion of motion. The rotations φ_1 and φ_2 behave in the same way.

It is important to point out that the correlations seen in the plots are obtained under a relatively high preload force of 2 N and such a force is opposing any relative rotation between the TM and the plunger.

This fact is due to the shape of the TM indentations and the plunger head (see Figure 3.11). When the preload force is low, which is the case of a nominal injection procedure (0.3 N), the relative rotations between the TM and the plunger may be higher. Anyway, it is obvious that the bi-stable configuration of the plunger negatively affects the clearance between the TM and the plunger itself at the release. In fact, the bi-stability is observed in the same plane where most of the TM momentum at the release is generated, which suggest a correlation between the linear runner constraint mechanism and the release performance.

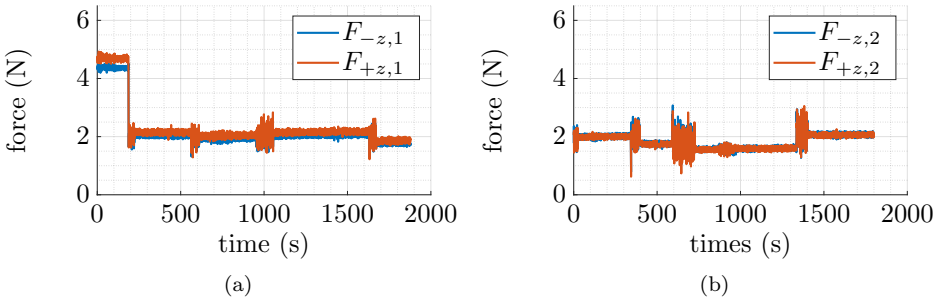

Figure 3.8: Preload forces of both plungers acting on the TMs during the repositioning tests. TM_1 is on the left, TM_2 on the right.

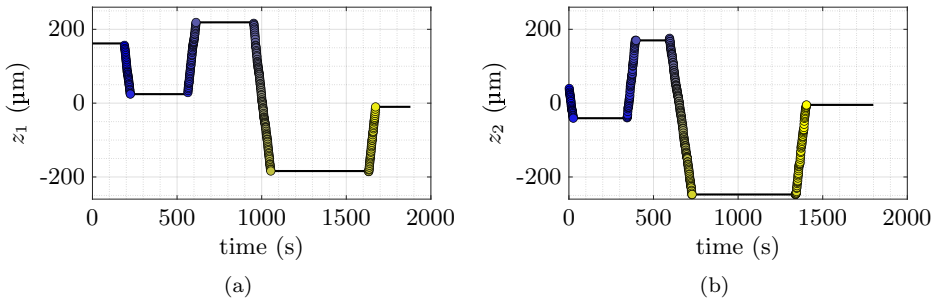

Figure 3.9: TM displacements z_1 and z_2 as function of time during the repositioning tests of the 9th of July. The z motion of the TM is commanded by actuating the NEXLINEs.

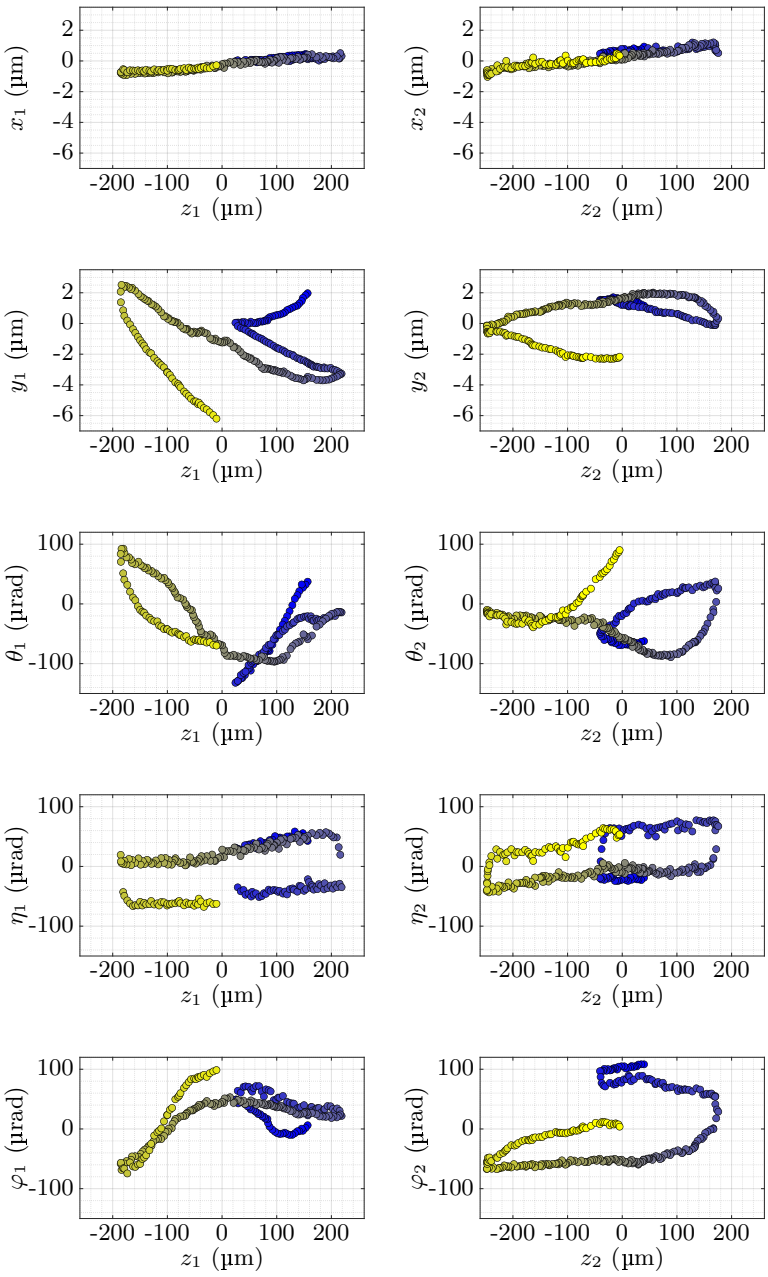

Figure 3.10: Displacements x, y and rotations θ, η, φ of the TMs during the repositioning tests of the 9th of July plotted against the z position. Time is represented by the color gradient, from blue (start) to yellow (end). In the graphs of η_1 and η_2 a hysteresis cycle is clearly visible, caused by the bistable behaviour of the plungers in the plane x−z.

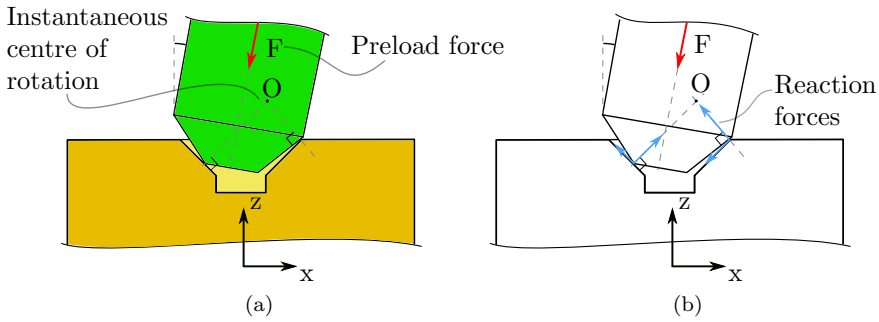

Figure 3.11: Scheme of the forces arising at the grabbing of the TM in case there is a misalignment between the TM and the plunger. The forces create a torque that reduces the misalignment.

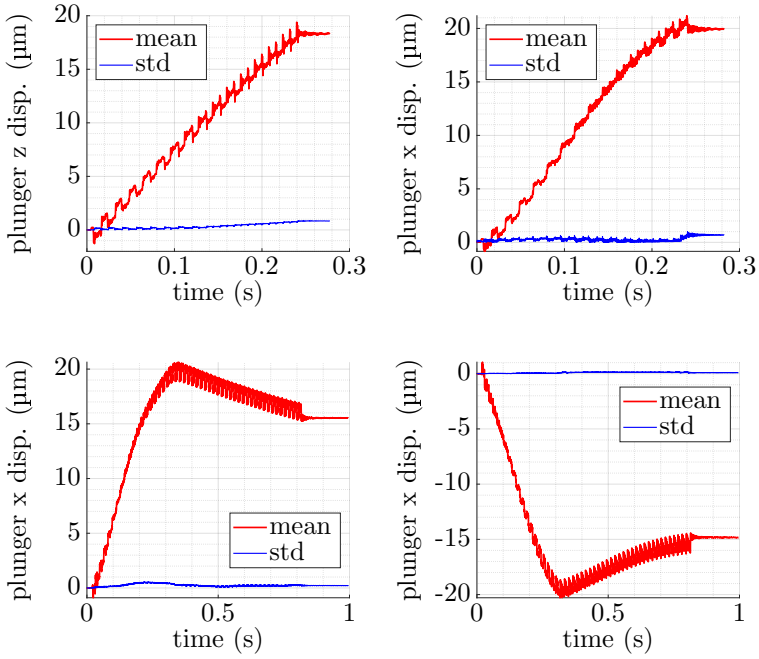

Figure 3.12: Plunger motion when actuating the NEXLINE, measured on-ground with a laser interferometer. The mean of 5 tests (red), along with the standard deviation (blue), is shown. Top graphs show the axial (z) and lateral (x) motion of the plunger when commanding a short repositioning (15 NEXLINE steps). In this range, the plunger moves diagonally since the same distance is covered axially and laterally. Bottom graph show the saturation of the lateral motion for extended repositioning (50 NEXLINE steps). The saturation is similar when commanding a backward (left) or forward (right) motion.

In order to verify the bi-stable behaviour of the plunger, an experiment was carried out at the Laboratory of Space Applications of Trento University (details on the experimental setup are given in Section 4.1). The NEXLINE was actuated and the resulting plunger axial and lateral motions on the x−z plane were measured with a laser interferometer. The plunger initial position was set close to the nominal grabbing position, to replicate the in-flight release conditions. The NEXLINE was commanded setting either 15 or 50 steps, to verify the effect of a short range and a long range repositioning. In Figure 3.12, the experimental results are shown. When commanding a short repositioning (top graphs), the trajectory of a plunger that reverse its motion is parallel to the bisector of the x−z plane, since the x and z position of the plunger head have similar time history. When commanding a longer repositioning (bottom graphs), it can be seen how the lateral motion saturates after approximately 20 steps of the NEXLINE.
So, the on-ground tests were useful to verify that the plunger motion is non-ideal, especially in the first instants after the inversion of the NEXLINE motion, which is even more critical since it happens any time the handover or the hammering is performed.

3.1.6 Alignment of the GPRM units

Another important factor that influences the TM-plunger clearance at the release is the relative alignment of the two GPRM units obtained during the integration of the GRS. The alignment of the two units is a difficult task, mainly for the following reasons:

- The objects to be aligned (the plungers) are cylindrical and small, which means that is it difficult to define reference surfaces for the coordinate measuring machine.

- The plungers are not rigidly attached to the external structure of the GPRM unit. In fact, as explained in Section 3.1.5, their position depends on the state of the NEXLINE actuator mechanism.

- Once the two GPRMs are mounted on the GRS, the two plungers are not reachable due to the presence of the EH and the TM.

For this reason, the alignment procedure was carried out assembling the two GPRM units on a dummy IIS by MAGNA Steyr Space, and then replicated by CGS S.p.A. (now OHB Italia) on the FM IIS. In particular, the first step of the alignment was to align each GPRM to its relative flange, which constitutes the interface with the IIS. In this way, the reference surfaces for the alignment are transferred from the plungers to the flanges, which are outside the EH (see Figure 3.13). As a last step, the two flanges were aligned with respect to each other.

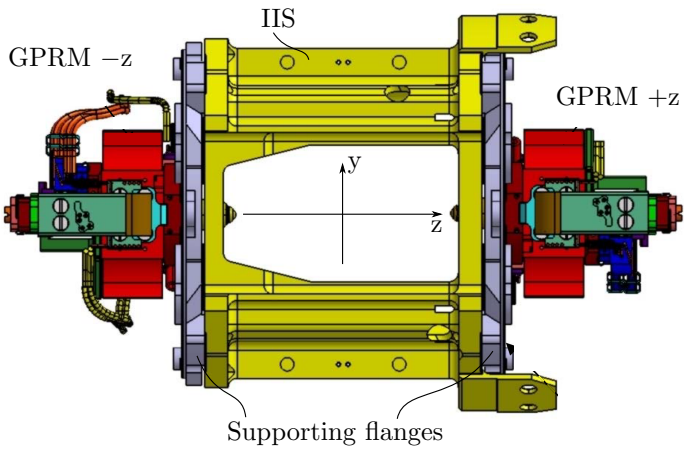

Figure 3.13: GPRM units, with their supporting flanges, assembled onto the internal interface structure (IIS) of the GRS. Courtesy of MAGNA Steyr Space.

Table 3.3: Results of the GPRMs alignment budget estimation performed by CGS S.p.A. (now OHB Italia).

	DOF	GPRM bottom		GPRM top		Unit
		Offset	RSS	Offset	RSS	
FM_1	x_1	-12.4	17.6	12.5	27.0	µm
	y_1	8.0	25.2	8.6	32.5	
	z_1	10.1	78.1	5.2	80.7	
	θ_1	1.0	859.9	102.8	863.4	µrad
	η_1	844.9	461.3	924.3	467.8	
	φ_1	-289.5	462.2	-116.8	468.6	
FM_2	x_2	15.2	20.6	18.6	29.1	µm
	y_2	-28.8	33.0	-26.0	38.8	
	z_2	13.4	29.7	15.0	36.1	
	θ_2	-522.8	895.3	-523.9	898.7	µrad
	η_2	1047.2	205.8	1123.8	220.0	
	φ_2	-406.7	694.9	-234.3	699.3	

According to the alignment results contained in the mission documentation, the two units of each GRS were aligned fulfilling the requirements. The final alignment budget, carried out by CGS S.p.A., is reported in Table 3.3. Both the measured offsets and the uncertainties, expressed as root square sum (RSS) of all the possible contributions, are reported. The table shows the offsets and the uncertainties of the top (+z) and bottom (−z) plunger with respect to the electrical zero reference frame, i.e., the GRS reference frame. Note that the offsets are similar between the top and bottom units, as the alignment procedure consisted in first aligning the

bottom unit to the TM and then the top unit to the bottom unit. For example, if the bottom unit has a θ tilt offset of 860 µrad then the top unit, since it is aligned directly to the bottom, will also have a similar θ tilt offset.
The offset and uncertainty budget reported includes the contributions of the machining tolerances, the alignment procedure and the uncertainty in the plunger position (discussed in Section 3.1.5). The relatively high RSS uncertainties clearly suggest that, even if the plungers offset were aligned with respect to each other, a significant misalignment may still be present. Such a misalignment may be critical considering that any superposition of linear/angular misalignments affects the TM-plunger clearance. For example, imposing in a TM-plunger 3D model a relative misalignment on the plane x−z equal to the RSS of the angle θ ($\approx$ 900µrad), the limits on the maximum φ angle leading to a contact on the indent are reduced from $\approx \pm$4800µrad to $\approx \pm$2500µrad.
The numbers presented in Table 3.3 have been compared with the mean values of the in-flight TM position at the pre-release. The comparison of the on-ground alignment budget with the in-flight pre-release position z_{pr} and orientation ϕ_{pr} have been discussed in Section2.5. Regarding the other DOFs, the comparison consists in a two-step verification, carried for the two planes x−z−η and y−z−θ. The first step is to check if the TMs mean pre-release position x_{pr} or y_{pr} stays inside a band defined by the offsets and the RSSs of the top and bottom GPRMs (an example is shown in Figure 3.14a). The second step consists in verifying if the TM pre-release orientations η_{pr} or θ_{pr} stays inside the minimum and maximum angles computed from the offsets and RSSs of the plungers (Figure 3.14b). If the first check is not passed, the second step is carried out assuming the TM position is the average of the plunger offsets.

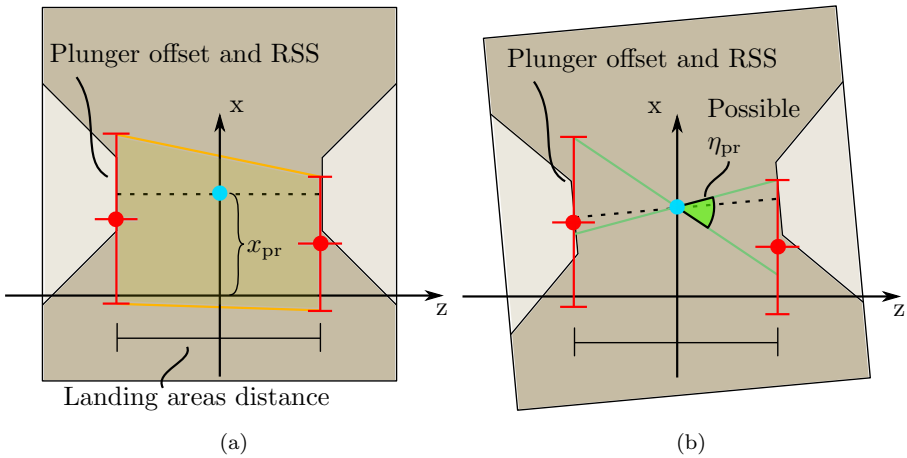

Figure 3.14: Steps for the comparison of on-ground alignment of the GPRMs and the in-flight pre-release position and orientation of the TM (x−z−η plane is depicted). On the left, check of the x_{pr} position, on the right check of the η_{pr} angle.

The results of the analysis are reported in Table 3.4. While some of the pre-release positions and orientations are compatible with the on-ground alignment, others are not. The cause of these discrepancies is not known, even if there is the suspect of some errors in the interpretation of the reference frames (for example, the orientation of the plungers of the GRS_2 is approximately 1.1×10^3 µrad, while the in-flight orientation is approximately -1.2×10^3 µrad , i.e., basically opposite).

Table 3.4: Results of the comparison between on-ground alignment budget and the pre-release state of the TM in flight.

TM_1		TM_2	
x_1	Passed	x_2	Passed
y_1	NOT passed	y_2	NOT passed
θ_1	Passed	θ_2	Passed
η_1	Passed	η_2	NOT passed

3.2 TM-plunger collision models

As discussed in Section 2.6.1, the analysis of the in-flight data strongly suggests that a TM-plunger contact is the cause of the high TM release momentum. The analysis of the contributions that affect the relative TM-plunger clearance, carried out in the previous sections, although not conclusive, does not allow to exclude the hypothesis. In fact, the presence of several factors that reduce the clearance should be interpreted as another suggestion that the contact is indeed possible. In order to prove that a TM-plunger contact is the cause of the observed release momentum, different mathematical models of the GPRM interaction with the TM have been developed. The models are used in particular to explain the reliable non-compliant fast tip retraction tests, i.e., those tests which are similar to the nominal injection procedure but resulted in a TM momentum outside the requirements.
Before developing the models, an interesting consideration is derived from the correlation of the preload force exerted by the GPRM and the TM release kinetic energy. Those quantities are plotted against each other for the two TMs in Figure 3.15. The tests are subdivided in slow tip and fast tip tests. As can be seen on the plots, both slow tip and fast tip tests are not easily correlated to the preload force acting on the TM at the release.
The gray curve on the plots, which is the same for TM_1 and TM_2, represents the conservation of the GPRM mechanical energy before and after the release (the elastic energy stored in the plungers due to the preload force F is set equal to the TM kinetic energy, neglecting the energy of the plunger oscillations). Such a curve should represent an upper bound for the in-flight data, since in reality only a fraction of the potential energy stored in the mechanism before the release is transferred to the released TM.

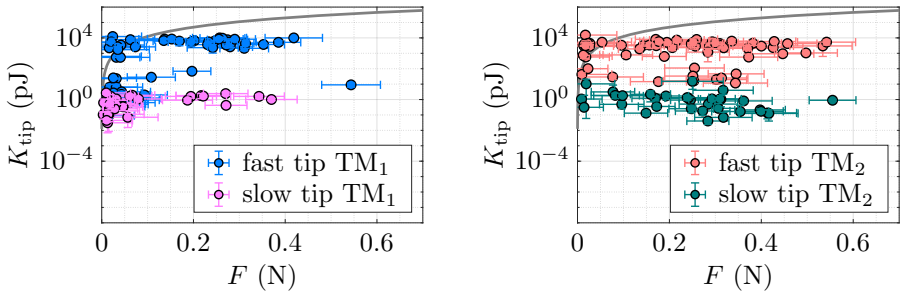

Figure 3.15: Correlation of the preload force (F) and the released TM kinetic energy (k_{tip}) from the in-flight fast and slow tip tests. On the left TM_1 and on the right TM_2. The gray curve represents the kinetic energy of the TM as a function of the preload according to the energy conservation law.

Unexpectedly, there are tests which lay above the curve for very low pre-load. Thus, the release dynamics is not trivially correlated to the pre-load. The conservation of mechanical energy is imposed as described in Equation 3.1.

$$U_{\text{pre}} = K_{\text{post}} \Rightarrow \frac{1}{2}\frac{F^2}{k} = K_{\text{tip}} \tag{3.1}$$

Where U_{pre} is the potential energy stored in the mechanism before the release. The energy is stored thanks to the elastic deformation of the low stiffness linkages of the GPRM. The kinetic energy post release is K_{post} and is assumed to be equal to the released TM kinetic energy (K_{tip}). This is true in the hypothesis that all the potential energy is transferred to the TM. The variable F is the preload of the mechanism and the variable k represents the equivalent stiffness of a single GPRM unit. The value of the stiffness k is computed thanks to a dedicated in-flight test. The test is performed starting from the pre-release state, with the TM held in position by the two tips, and commanding a slow tip retraction followed by a slow extension. The preload force should then decrease and increase, following the tip motion, due to the elasticity of the mechanism. In Figure 3.16, the in-flight data of the $GPRM_1$ stiffness test is shown. The slope of the linear fit on the force sensor signal in the highlighted time intervals gives an estimation of the stiffness of the series of the two GPRM units. The value of the estimated stiffness is approximately $2 \times 10^5\,\text{N}\,\text{m}^{-1}$ and is the same for both the GPRMs. In the hypothesis the two units of each GPRM have similar stiffness, the value of a single unit is equal to approximately $4 \times 10^5\,\text{N}\,\text{m}^{-1}$.

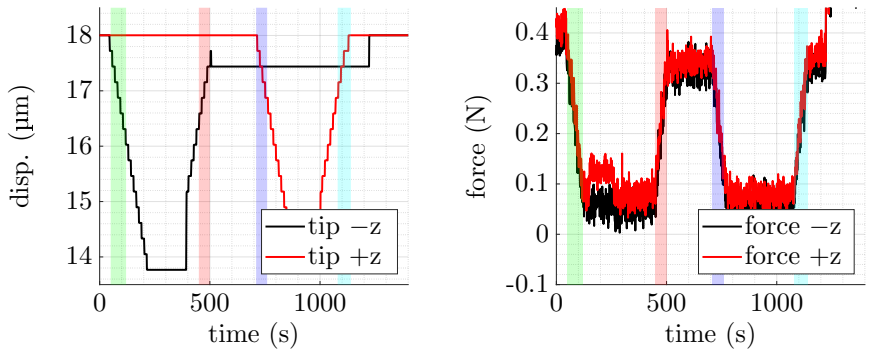

Figure 3.16: In-flight data of the stiffness tests of the $GPRM_1$. The time intervals where the stiffness is computed are highlighted with colored patches. Inside each interval, both the extension of a tip (+z or −z) and the preload forces have are characterized by a linear trend.

3.2.1 Pre-release static equilibrium

The first collision model developed is based on a simplified 2D geometry of the GPRM and is used to verify if there exist a pre-release equilibrium configuration of the GPRM in which the two plungers are preloaded both axially (z direction, nominal case) and laterally (x or y directions). If such an equilibrium is possible, at the release the elastic potential energy stored in the mechanism due to the preload forces would trigger a motion of the plunger which may result in a collision with the TM.

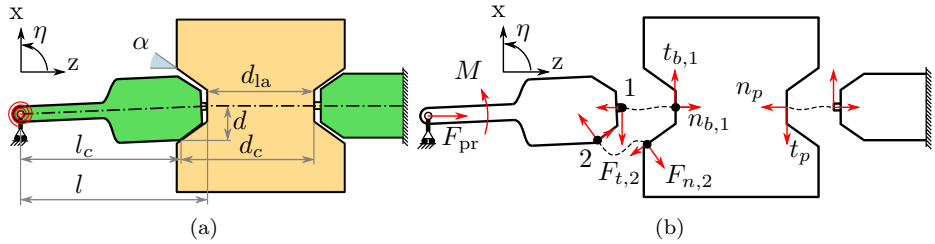

Figure 3.17: On the left, sketch of the pre-release state of the GPRM with a plunger in contact with the TM on the side of the indent. The geometrical parameters of the model are shown. On the right, free-body diagram of the model, showing the notation of the forces and torques applied.

The first hypothesis of the model is that one plunger is fixed to the ground while the other plunger is able to rotate and translate on the plane. Such a hypothesis is based on the fact that, for the in-flight reliable non-compliant releases, one plunger always gives a significantly larger lateral impulse with respect to the other (as

explained in Section 2.6.1). The second hypothesis is that, at the pre-release, the TM is in contact with the tips (pushing on the landing areas) and the tilted plunger (rotated by $\approx 1 \times 10^3$ mrad) is touching the indent surface. Under those hypotheses, the scheme of the model is shown in Figure 3.17. The values of the parameters are listed in Table 3.5.

Table 3.5: Numerical values of the geometrical and physical parameters of the 2D model of the static equilibrium condition of the GPRM. The values are estimated from the CAD model of the GPRM, setting a TM-plunger relative misalignment of $\approx 1 \times 10^3$ mrad, and from mission technical notes. The point where the TM and the plunger touch is referred to as contact point.

Param.	Value	Unit	Description
d	0.0043	m	x distance of the contact point from the TM center
d_{la}	0.0362	m	z distance of the landing areas, where tips are in contact with the TM
d_c	0.0406	m	z distance from the right tip to the contact point
l	0.0490	m	z distance from the plunger pivot (assumed in the middle of the linear guide), to the tip
l_c	0.0449	m	z distance from the plunger pivot to the contact point
k_{lat}	7×10^4	$\mathrm{N\,m^{-1}}$	Lateral stiffness of the plunger measured at the tip
F_{pr}	0.25	N	Pre-release preload force on the TM
K_{tip}	1×10^4	pJ	Typical value of the TM kinetic energy after the release
α	0.724	rad	Angle of the indent surfaces with respect to z axis

The GPRM may reach this configuration if the two plungers are not aligned. For simplicity it is assumed that the TM is aligned with the plunger that does not contribute to the release dynamics, while the other plunger is tilted with respect to the TM. When the TM is grabbed, the tilted plunger pushes against the indent with a certain angle, thus a torque which tends to align it to the TM is generated (see Figure 3.11). The plunger is now tilted with respect to its equilibrium, so it is preloaded laterally. At the handover, the plunger will recover some of the lateral preload but may still remain in contact with the TM in one point of the indent. The steps here described are shown in Figure 3.18. It is important to notice that the lateral preload acting on the plunger is not pushing it against the indent where it is in contact with the TM. Conversely, it is pulling the plunger in the opposite direction.

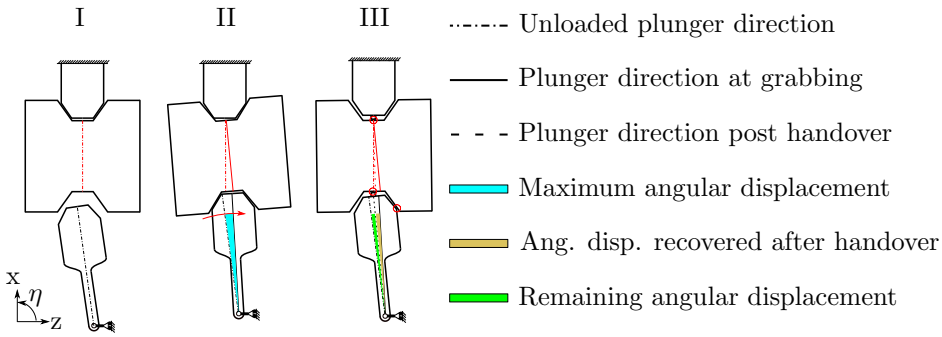

Figure 3.18: Steps of the grab and handover procedure that may lead to a TM held in position by the tips and a contact point with a tilted and laterally preloaded plunger.

The equilibrium of the TM and the plunger, given the forces and torque in the scheme of Figure 3.17, is expressed in Equations 3.2 and 3.3 respectively. The variables n_p, t_p, $n_{b,1}$, $f_{n,2}$ and $f_{t,2}$ are considered unknowns, while the variable $t_{b,1}$ (friction on the landing area) is considered independent.

$$\begin{cases} -t_p + t_{b,1} - (f_{n,2}\cos(\alpha) + f_{t,2}\sin(\alpha)) = 0 & , \text{x} \\ -n_p + n_{b,1} + (f_{n,2}\sin(\alpha) - f_{t,2}\cos(\alpha)) = 0 & , \text{z} \\ -d_{\text{la}}t_{b,1} + d_c(f_{n,2}\cos(\alpha) + f_{t,2}\sin(\alpha)) + d(f_{n,2}\sin(\alpha) - f_{t,2}\cos(\alpha)) = 0 & , \eta \end{cases} \tag{3.2}$$

$$\begin{cases} -n_{b,1} - (f_{n,2}\sin(\alpha) - f_{t,2}\cos(\alpha)) + f_{pr} = 0 & , \text{z} \\ M - t_{b,1}l + (f_{n,2}\cos(\alpha) + f_{t,2}\sin(\alpha))l_c - (f_{n,2}\sin(\alpha) - f_{t,2}\cos(\alpha))d = 0 & , \eta \end{cases} \tag{3.3}$$

The friction coefficients of the contacting surfaces in point 1 and 2 can be computed as functions of the independent variable $t_{b,1}$, as shown in Equation 3.4.

$$\begin{cases} \mu_1 = \dfrac{t_{b,1}}{n_{b,1}} = \dfrac{(d(d_c + l_c)t_{b,1})}{(df_{\text{pr}}(d_c + l_c) - d_c M + d_c l t_{b,1} - d_{\text{la}} l_c t_{b,1})} \\ \mu_2 = \dfrac{t_{b,2}}{n_{b,2}} = \dfrac{(-(d_{\text{la}} l_c t_{b,1} + d_c(M - l t_{b,1}))\cos(\alpha) + d(-M + (d_{\text{la}} + l)t_{b,1})\sin(\alpha))}{(d(-M + (d_{\text{la}} + l)t_{b,1})\cos(\alpha) + (d_{\text{la}} l_c t_{b,1} + d_c(M - l t_{b,1}))\sin(\alpha))} \end{cases} \tag{3.4}$$

The torque M, generated by the elastic deformation of the GPRM components, is computed from the experimental value of the lateral stiffness of the plunger k_{lat}, equal to $7 \times 10^4\,\text{N m}$. At first, the conservation of mechanical energy before and after the release is computed, supposing most of the elastic energy is stored in the lateral preload of the GPRM, as shown in Equation 3.5.

$$K_{\text{tip}} = \frac{1}{2}\eta_{\text{pl}}^2 k_{\text{lat}} l^2 \tag{3.5}$$

Where the value of η_{pl} corresponds to the tilt angle of the plunger from its equilibrium. The tilt is obtained solving Equation 3.5 and used in Equation 3.6 to finally compute the torque M.

$$M = \eta_{\text{pl}} k_{\text{lat}} l^2 = l\sqrt{2K_{\text{tip}} k_{\text{lat}}} \tag{3.6}$$

Considering the model parameters uncertainties and feasible values of the static friction coefficient for gold-gold contact surfaces equal to 0.5, the graph of Figure 3.19 shows that there may be a solution to the problem where the TM is in equilibrium at the pre-release state and the plunger is laterally preloaded by an amount sufficient to transfer a significant release kinetic energy to the TM. Despite this, the angle η_{pl} of the plunger preload computed from Equation 3.5 is approximately 10 µrad. Such a value is small if compared to the angle that the plunger should span, once the TM is released, to collide to the opposite indent face, which is approximately 4×10^2 µrad under nominal conditions. Thus, the proposed model is not able to justify the measured K_{tip} in the presence of a pre-release equilibrium where the plunger is laterally pre-loaded.

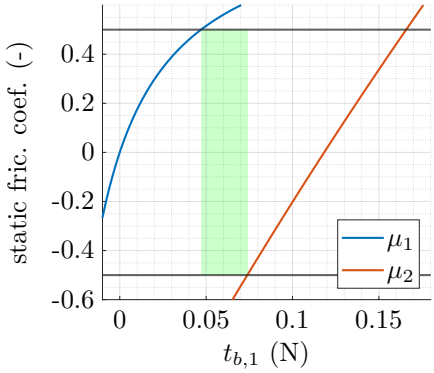

Figure 3.19: Plot of the curves μ_1 and μ_2 for feasible values of the model parameters, along with the ± values of the gold-gold static friction coefficient (horizontal black lines), set to 0.5 (-). The two curves, when intersecting the horizontal lines, define a zone (green rectangle) of the possible values of $t_{b,1}$ that guarantee the presence of an equilibrium condition in the preloaded configuration. In fact, for any $t_{b,1}$ comprised in the rectangle, both μ_1 and μ_2 are within the range ±0.5.

3.2.2 Piezo-induced oscillations of the plunger

The next step in the analysis of the GPRM release dynamics is to build a dynamical model, that takes into account not only the elastic energy due to the preload of the mechanism, but also the energy stored in the piezo-stack actuators. Since the development of such a model required an intense experimental activity with a dedicated on-ground setup, the description of the experiment and of the model development are reported in the following Chapter.

Chapter 4

Dynamic testing of the GPRM

The possibility of an impact occurring during the TM release due to plunger motion is explored in this Section through a combined experimental-theoretical approach. The first step consists in a testing campaign performed on the GPRM EQM, aimed at characterizing the motion of the plunger on the x−z plane at the tip retraction. The second step is based on the identification of a mathematical model of the GPRM dynamics at the release, completed by an impact model.
The third step consists in the comparison between the predicted in-flight TM dynamics, subjected to the impacts produced by the identified dynamic model of the GPRM, and the actual dynamics described by the telemetry signals.

4.1 On-ground testing of the GPRM dynamical response

In this section the tests performed on the GPRM qualification model to characterize its motion in the x−z plane are presented. The set-up, derived from a previous GPRM ground testing experiment, is designed to simulate the outer-space environment ([24]), as shown in Figures 4.1 and 4.2. It includes a vacuum chamber maintained at approximately 10^{-7} mbar by an ion pump. The vacuum chamber is positioned on top of a customized W.A.V.E. DUO 100 ACTIVE anti-vibration platform that limits the external disturbances caused by floor vibrations. A SIOS SP-S 120 laser interferometer pointing inside the chamber (through optical windows) is used to measure the displacements of the plunger of the GPRM EQM, located in the chamber. The laser interferometer sampling frequency is 200 kHz and the measurement resolution is 0.3 nm. When a tip retraction is performed, the laser interferometer controller is triggered by the commanding voltage drop and the plunger motion signal is stored.
In order to fully characterize the in-plane plunger motion, several tests are performed pointing the laser interferometer at different locations on the plunger surface. The laser is pointed both orthogonally to the plunger axis (lateral surface

of the plunger, direction x) and parallel to the plunger axis (direction z). The measuring configurations are shown in Figure 4.3, along with a picture of the laser pointing at the plunger in Figure 4.4. Laterally, the laser is focussed on six plunger-surface positions (x_i, for $i \in \{1, 2, \ldots, 6\}$), and on the supporting flange (x_{fl}). The latter is needed to verify that the fixture of the mechanism is stiff enough and does not participate in the measured dynamics. For each laser position, a data set of ten measurements of the plunger oscillations and five noise measurements (not actuating the system) are acquired.
In Figure 4.5, an example of the mean signal and the standard deviation of the data set from the fourth lateral laser position is plotted. The amplitude of the oscillation excited by the retraction of the plunger is on the order of 0.2 µm and is characterized by a good repeatability. The signal to noise ratio (SNR) is about 1×10^2.

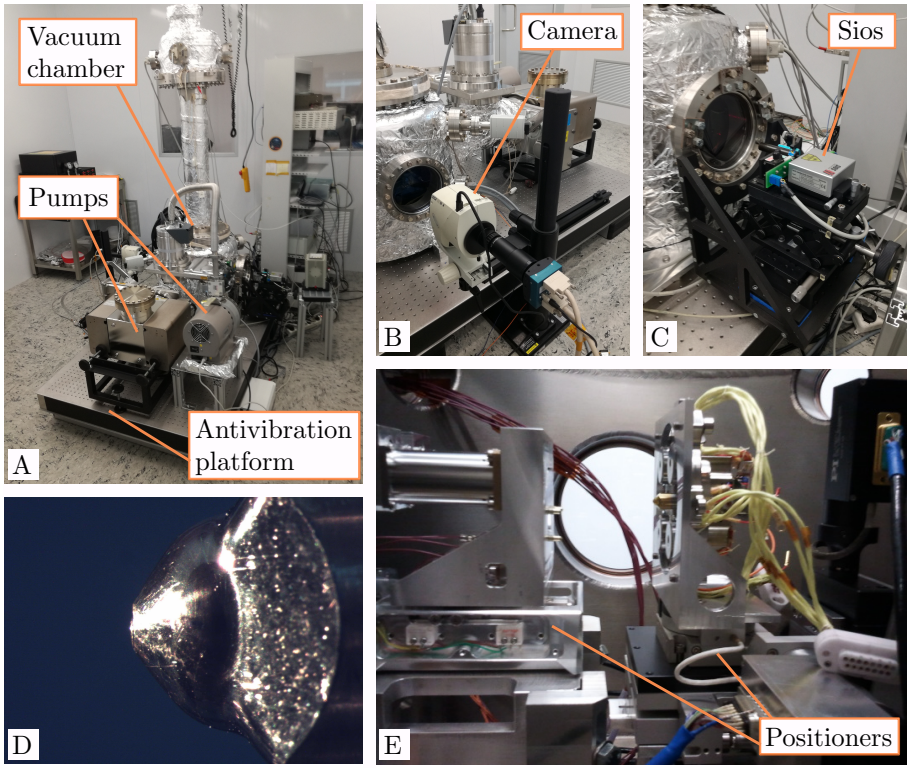

Figure 4.1: In picture A, full view of the experimental setup inside the clean room of the Trento University Space Application Laboratory. Two pumps are used to reach outer-space pressure inside the vacuum chamber. The high-speed camera and the SIOS (pictures B and C) point inside the chamber thanks to dedicated optical windows. In picture D, high resolution image of the pyramidal plunger head inside the chamber. In picture E, the GPRM inside the vacuum chamber with its positioners and wiring.

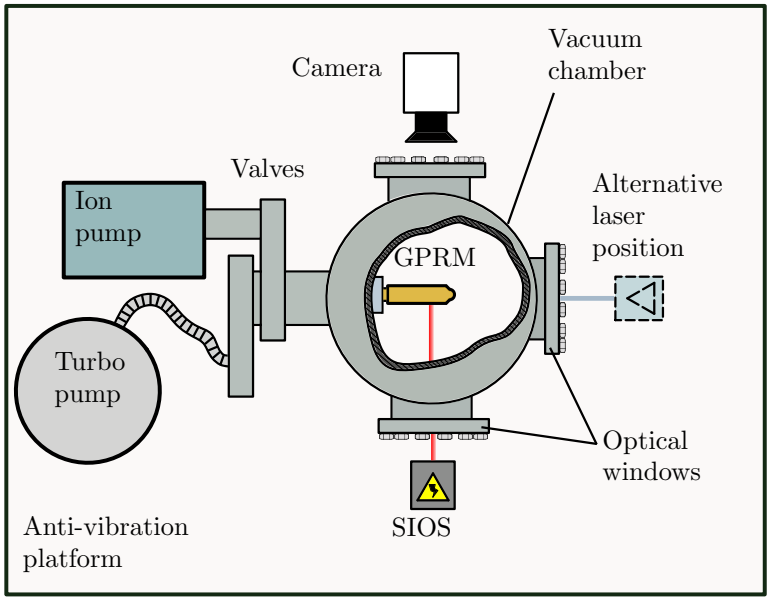

Figure 4.2: Schematic top view of the experimental set-up, not to scale. The hole setup is mounted on an anti-vibration platform, to isolate the experiment from the ground noise.

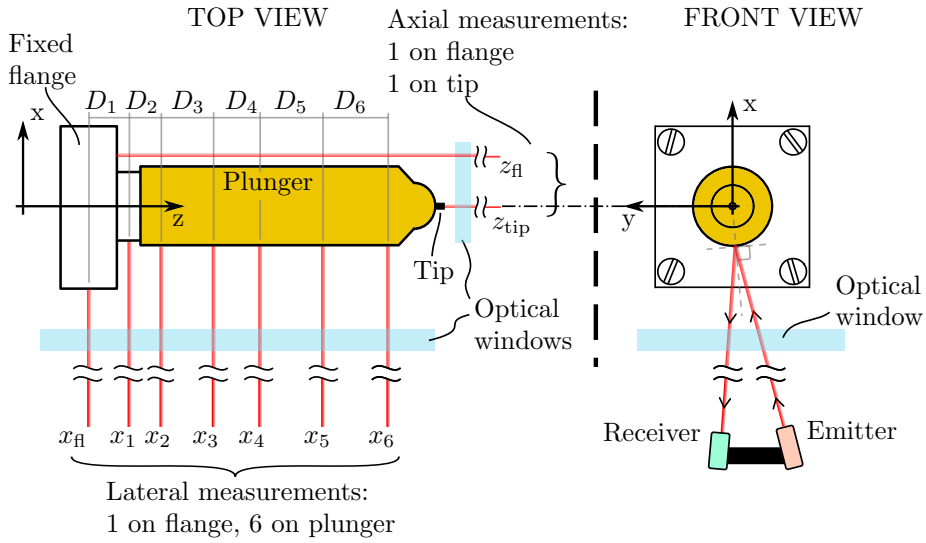

Figure 4.3: Schematic representation of the laser positions used to acquire the data, top and front views. On the right, picture of the plunger, inside the vacuum chamber, with the laser pointed on its lateral surface.

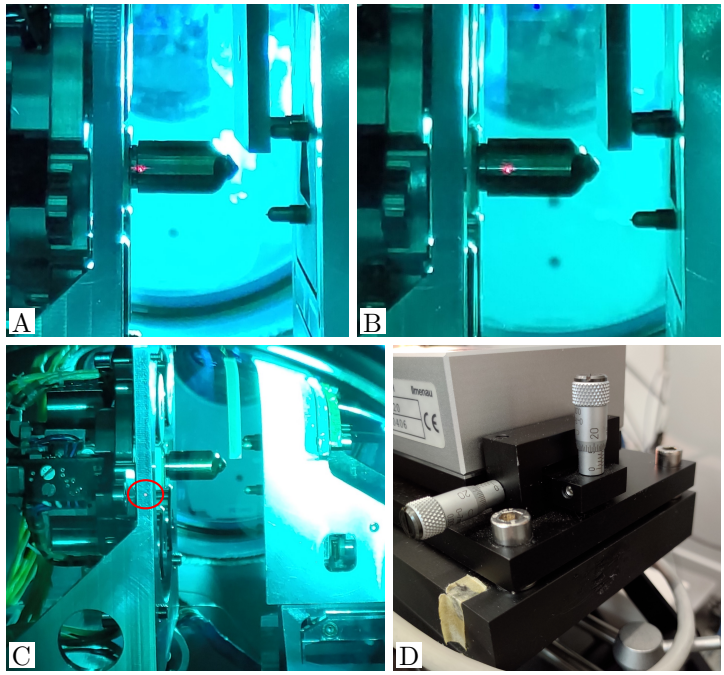

Figure 4.4: Pictures of the GPRM located inside the vacuum chamber with the laser focussed on the surfaces of interest. In pictures A and B the laser is pointed at two different lateral positions on the plunger. In pictures C it is pointed at the flange. Picture D shows two of the micrometer screws used to precisely point the laser.

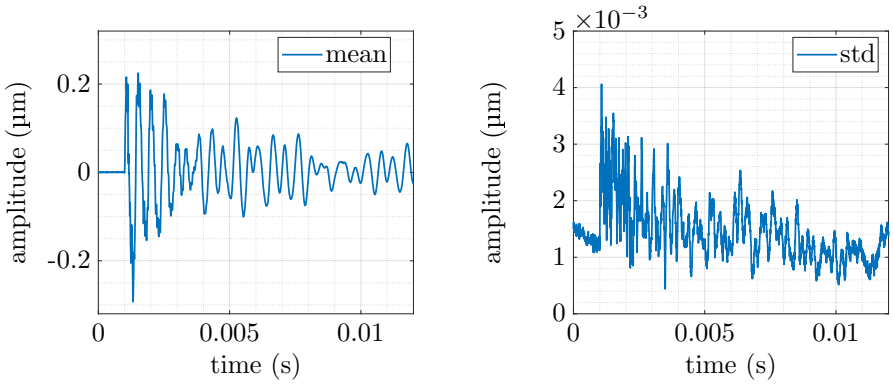

Figure 4.5: Mean signal of the fourth lateral data set x_4 along with its standard deviation. The high precision of the laser interferometer and the good repeatability of the plunger motion allow for a high SNR.

Regarding the set of axial measurements, due to the absence of a frontal flat surface on the plunger to be exploited as a target mirror for the interferometer, the z motion of the plunger is characterized using the release tip edge as a mirror (z_{tip}). Again, the motion of the supporting flange (z_{fl}) is measured to exclude a significant contribution to the dynamics.
In Figure 4.6, the mean signal and the standard deviation of the ten repetitions of the axial data set are plotted. The measured motion of the release tip is about 15 µm, with an evident superimposed oscillation (overall amplitude of about 1 µm) produced by the dynamics of the system. A relevant drawback of this approach is that this signal is dominated by the relative plunger-tip motion. The release tip does not contribute to the impact dynamics even though its motion constitutes the trigger event. However, the dynamic response of the mechanism is still detectable if compared with the motion of the flange (which is negligible) and the standard deviation of the set (SNR about 1×10^2). The underlying plunger axial motion therefore needs to be estimated by subtracting the relative motion of the tip. This requires a dynamical model of the mechanism, identified through the measured data set.

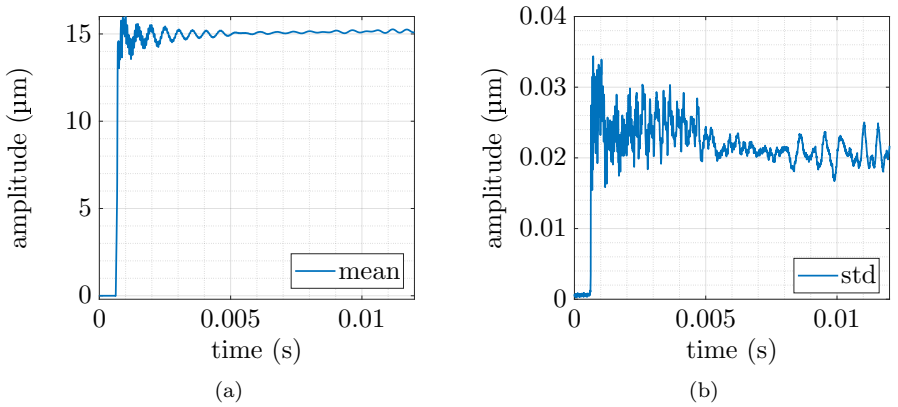

Figure 4.6: Mean signal of the axial data set z_{tip} along with its standard deviation. The high precision of the laser interferometer and the good repeatability of the plunger motion allow for a high SNR.

4.2 Identification of the GPRM dynamical model

The rigid body-like behaviour of the plunger

The first hypothesis to be verified to build a plunger-TM impact model is the rigid body-like behaviour of the former in the relevant bandwidth of frequencies present in the displacement signals. In Figure 4.7a the seven mean signals of the lateral data sets are plotted together, limiting the time axis to the first 2 ms of the plunger motion. The amplitude of the flange displacement mean signal ($\bar{x}_{\text{fl}}$, light blue curve) is much smaller than the mean signals of the plunger displacement ($\bar{x}_j$, for $j \in \{1, 2, \ldots, 6\}$) (ratio of about 8). The same plot shows that, after the first 100 µs in which the system is forced, the signals are composed of harmonic components describing free oscillations whose characteristics change along the plunger.

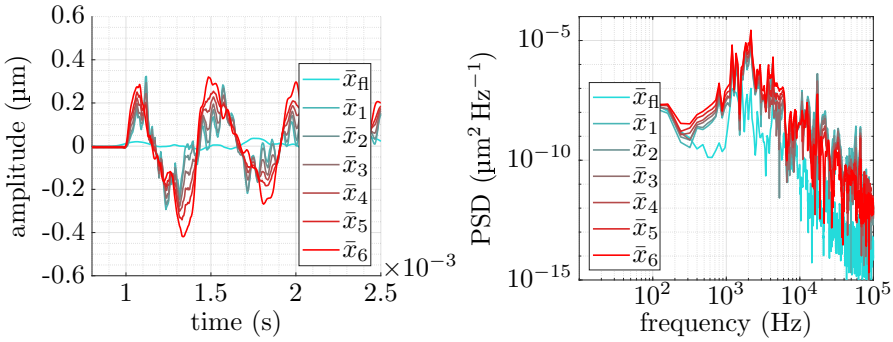

(a) (b)

Figure 4.7: On the left, magnified plot of the six lateral means signals together with the mean signal of the flange displacements (cyan curve). On the right, plot of the PSDs of the same seven signals.

In Figure 4.7b the power spectral densities (PSDs) of the mean signals are plotted, showing the presence of several peaks. Most of the energy is concentrated between 1 kHz and 2.5 kHz, where multiple peaks are present, with the highest one approximately equal to 2 kHz. Another predominant peak is present at around 17 kHz. The rigid-body like behaviour of the plunger is verified extracting the oscillation amplitude and phase of the main modes of vibration excited by the tip retraction, in the hypothesis that the system is linear. If the plunger is rigid at a given frequency, the amplitude of the lateral oscillation is expected to scale linearly with the axial position, while the phase remains constant or has a 180° shift across a nodal point.
In order to estimate the amplitudes and phases, the mean signals of the plunger lateral motion are fitted (see Appendix A). An example of the fitting result is shown in Figure 4.8.

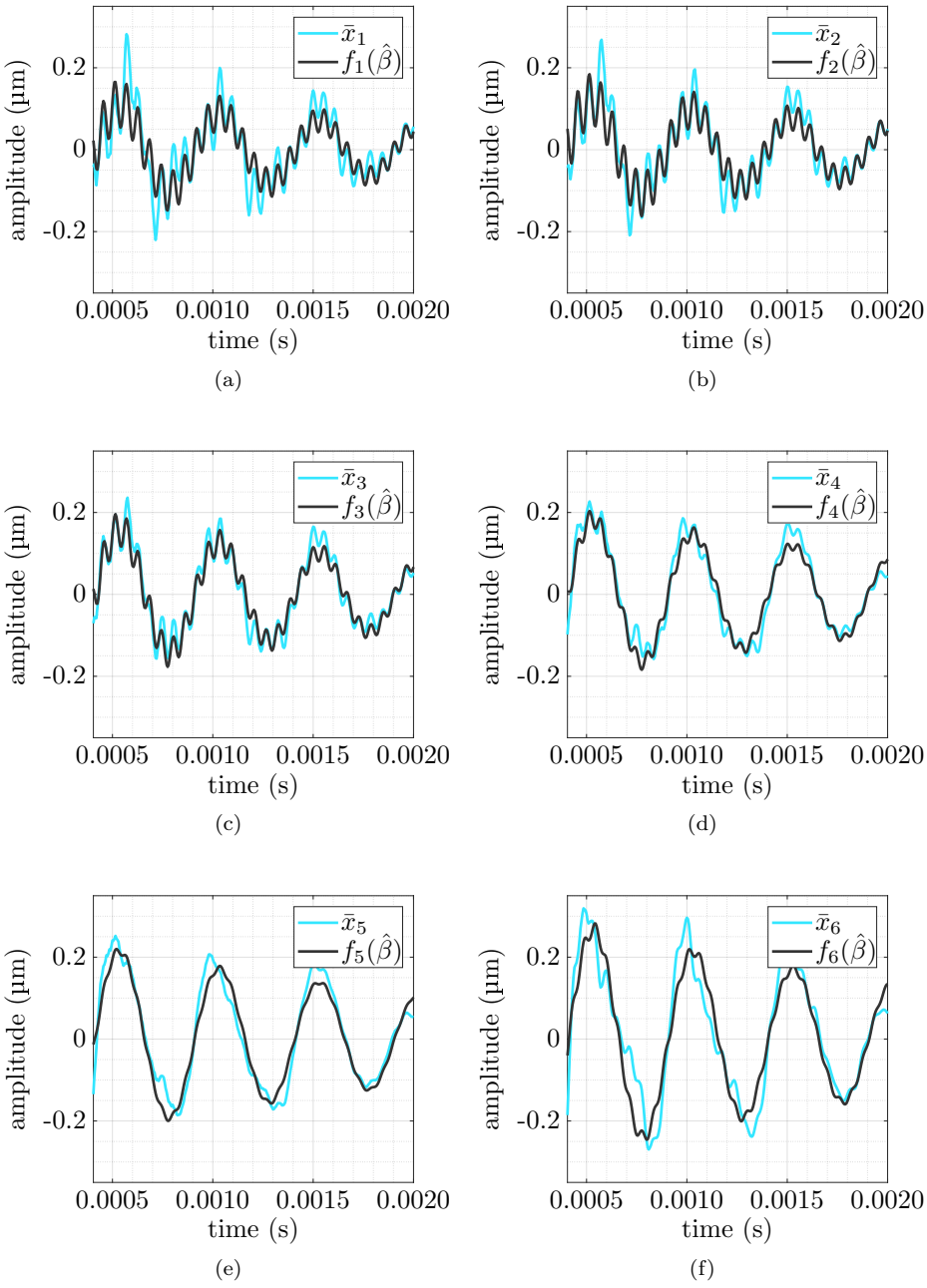

Figure 4.8: Magnified plots of the lateral mean signals for the laser positions of the plunger (cyan curves) and their respective fitting curves (black curves).

Each plot depicts one mean signal $\bar{x}_j$ (cyan curves) and the corresponding fitting curve obtained evaluating the fitting model function in the optimal parameters (black curves). The two modes-based target function is able to describe with good approximation the motion of the plunger capturing most of its dynamics.
To verify the correctness of the rigid body hypothesis, the estimated amplitudes and phases (defined with respect to the incipient motion of the plunger) are analyzed for the two modes along the plunger as shown in Figure 4.9. The estimated values of the parameters are plotted with error bars, expressing the 95% confidence intervals (CI) for amplitudes and phases. The uncertainty on the laser position is also considered.

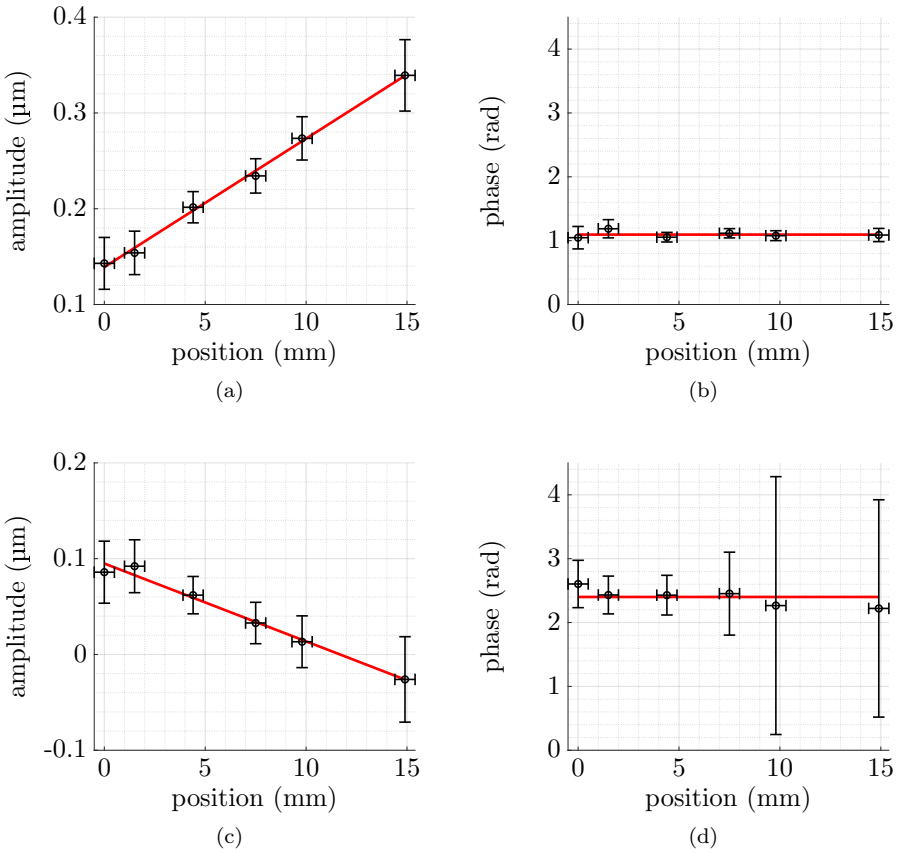

Figure 4.9: Amplitudes of the first mode (a), amplitudes of the second mode (c), phase of the first mode (b) and phase of the second mode (d). Amplitude and phases are plotted with their 95% confidence interval. Linear fit is shown in red.

The mode parameters are summarized in Table 4.1. The compatibility of the estimated amplitudes with a linear trend in both modes of vibration confirms that the plunger behaves as a rigid body in the range of frequencies of interest. Similarly, the estimated phase does not show fluctuations larger than the uncertainty, where

the latter gets worse when the detected amplitude approaches zero. This occurs when the interferometer is pointed close to the node of each mode shape, i.e., in the neighborhood of the flange for mode 1 and of the tip for mode 2.

Table 4.1: Frequency and damping parameters describing the GPRM plunger modes of vibration.

Param.	Value with 95% CI	Unit	Description
f_1	2009 ± 15	Hz	Frequency of the first mode of vibration
f_2	17256 ± 142	Hz	Frequency of the second mode of vibration
d_1	446 ± 104	s^{-1}	Damping exponent of the first mode of vibration ($d_1 = \xi_1 f_1/(2\pi)$)
d_2	695 ± 323	s^{-1}	Damping exponent of the second mode of vibration ($d_2 = \xi_2 f_2/(2\pi)$)

Estimation of the plunger motion at the tip retraction

The prediction of the TM state after the impact requires the knowledge of the plunger velocity at the collision instant. Given the rigid motion of the plunger, it is possible to characterize its motion on the x−z plane using only three laser measurements. The estimation process is carried out in steps:

- Definition of a mobile (subscript m) and a fixed (subscript f) reference frames (RFs), as shown in Figure 4.10. The former is body-fixed to the plunger and centered in the center of mass of the plunger (point G).
- Laser acquisition of the x_f displacement of the points P_A and P_B (whose $\mathrm{x_m}$ coordinates are known).
- Laser acquisition of the $\mathrm{z_f}$ displacement of the tip, which however does not yield the motion of the plunger. The subtraction of the tip-plunger relative motion is performed as explained in Section 4.2. After that, the $\mathrm{z_f}$ displacement of the point P_C, whose $\mathrm{z_m}$ coordinate is known, is estimated.
- Application of the coordinate transformation from the mobile to the fixed reference frame, making it possible to obtain a system of six equations, expressed in Equation 4.1.

$$\begin{pmatrix} z_{i,\mathrm{f}} \\ x_{i,\mathrm{f}} \end{pmatrix} = R(\eta) \begin{pmatrix} z_{i,\mathrm{m}} \\ x_{i,\mathrm{m}} \end{pmatrix} + \begin{pmatrix} z_G \\ x_G \end{pmatrix} \text{ for } i \in \{A, B, C\} \tag{4.1}$$

where $R(\eta)$ is the rotation matrix between the mobile and fixed frames. The solution of the system leads to the motion of the plunger described by the

position of the center of mass and its attitude (z_G, x_G, η) as a function of the measured signals $x_{A,\mathrm{f}}$, $x_{B,\mathrm{f}}$ and $z_{C,\mathrm{f}}$, together with the ancillary unknowns $z_{A,\mathrm{m}}$, $z_{B,\mathrm{m}}$, $x_{C,\mathrm{m}}$.

In order to maximize the accuracy of the estimation of the plunger rotation, P_A and P_B are chosen as the farthest points on the lateral plunger surface from where the laser is pointed, i.e., the laser locations 1 and 6 in Figure 4.3.

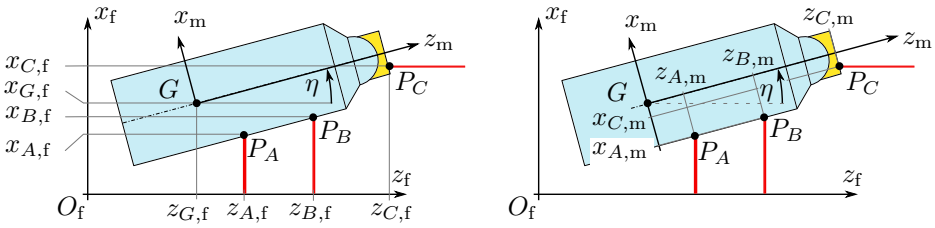

Figure 4.10: On the left, coordinates of the points of interest P_A, P_B and P_C expressed in the fixed reference frame (subscript f). On the right, same points expressed in the mobile reference frame (subscript m). The x coordinates of points P_A and P_B in the mobile reference frame are both equal to the plunger radius. The yellow area represents the tip, not to scale, showing that point P_C remains always on the tip.

Tip-plunger relative motion

The model-based subtraction of the tip-plunger relative motion from the measured tip axial displacement $\bar{z}_{\mathrm{tip}}$ starts from the identification of an electro-mechanical model of the mechanism dynamic response, shown in Figure 4.11. The control unit provides the 120 V DC signal ($V(t)$) commanding the full extension of the release tip, whereas the retraction is commanded by setting the voltage to zero through a resistor. Since $V(t)$ constitutes the input to the model, several tests are performed to characterize it, using a DSO7032A Agilent Technologies digital oscilloscope. The mean voltage signal is plotted in Figure 4.12. The outputs of the model are the axial displacement of the plunger ($z_1(t)$), of an internal lumped mass ($z_2(t)$), of the release tip ($z_3(t)$) and the charge in the actuated piezo ($q(t)$). The parameters of the model are listed in Table 4.2. Their nominal values are obtained from the GPRM technical documentation, published papers and direct measurements.

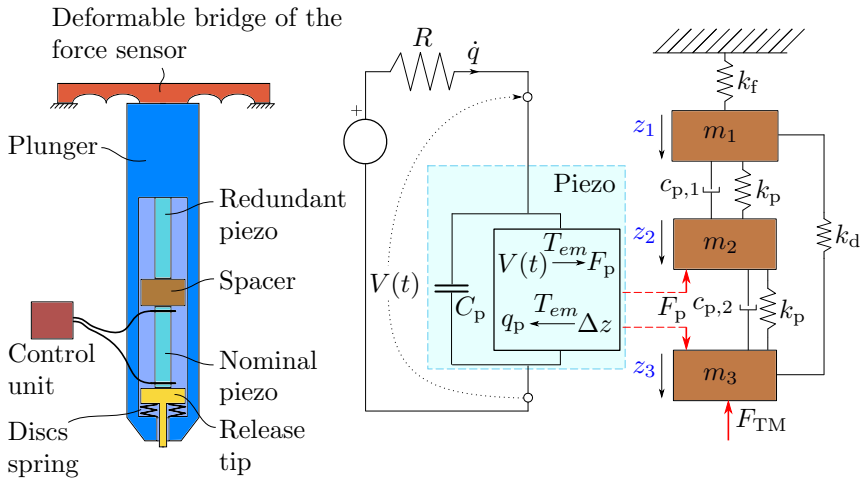

Figure 4.11: On the left, functional scheme of the GPRM release mechanism. On the right, lumped-parameter electro-mechanical model of the same mechanism. The quantity Δz is defined as $z_3 - z_2$. The lumped masses are defined as $m_1 = m_{pl} + 1/2 m_{pz}$, $m_2 = m_{sp} + m_{pz}$ and $m_3 = m_{tip} + 1/2 m_{pz}$, where subscripts pl, pz and sp stand for plunger, piezo and spacer respectively.

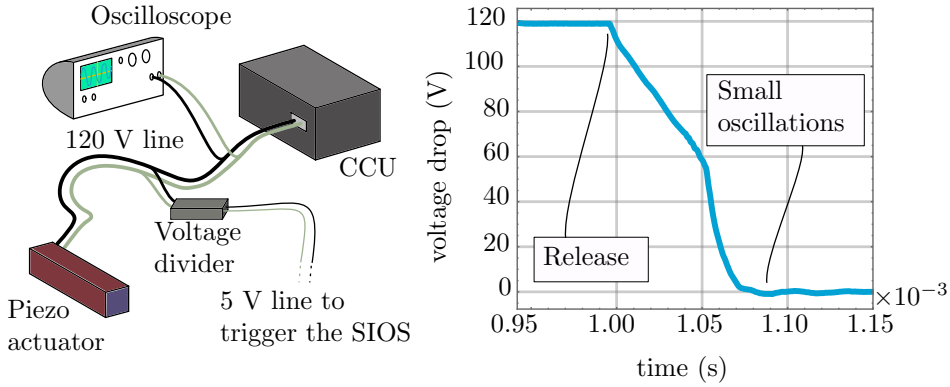

Figure 4.12: On the left, electrical scheme of the release mechanism actuation circuit, from which a low voltage signal is used to trigger the SIOS measurement recording. On the right, plot of the commanded piezo-stack voltage drop (from 120 V to 0 V) at the tip retraction, measured during on-ground testing. The mean of 5 tests is plotted.

Table 4.2: Parameters describing the GPRM lumped model.

Param.	Unit	Description
m_i	kg	Mass of the i-th model component ($i \in \{1,2,3\}$)
k_i	$\mathrm{N\,m^{-1}}$	Stiffness, with $i \in \{\mathrm{f},\mathrm{p},\mathrm{d}\}$, referring to force sensor, piezo-stack and discs spring respectively
$c_{\mathrm{p},j}$	$\mathrm{N\,s\,m^{-1}}$	Piezo damping coefficient ($j \in \{1,2\}$)
$V(t)$	V	Input voltage of the electrical circuit
R	Ω	Resistance of the electrical circuit
C_p	F	Capacitance of the piezo
T_{em}	$\mathrm{C\,m^{-1}}$	Electro-mechanical transducer (or piezo-effect)

The model is based on four linear differential equations (Equation 4.2), derived using Newton and Kirchhoff laws together with the constitutive equation of the piezo-stack actuator (Equation 4.3), which provides the exerted force F_p ([25], [17] and [26]). For the model identification, since the ground-based tests are performed with the mechanism unloaded, the force exerted by the TM on the tip (F_TM) is set to zero.

$$\begin{cases} m_1\ddot{z}_1(t) + c_{\mathrm{p},1}(\dot{z}_1(t) - \dot{z}_2(t)) + k_\mathrm{f} z_1(t) - k_\mathrm{p}(z_1(t) - z_2(t)) - k_\mathrm{d}(z_1(t) - z_3(t)) &= 0 \\ m_2\ddot{z}_2(t) + c_{\mathrm{p},1}(\dot{z}_2(t) - \dot{z}_1(t)) + c_{\mathrm{p},2}(\dot{z}_2(t) - \dot{z}_3(t)) + k_\mathrm{p}(2z_2(t) - z_1(t) - z_3(t)) &= -F_\mathrm{p} \\ m_3\ddot{z}_3(t) + c_{\mathrm{p},2}(\dot{z}_3(t) - \dot{z}_2(t)) + k_\mathrm{p}(z_3(t) - z_2(t)) + k_\mathrm{d}(z_3(t) - z_1(t)) &= F_\mathrm{p} - F_\mathrm{TM} \\ RC_\mathrm{p}\dot{q}(t) + q(t) - T_{em}(z_3(t) - z_2(t)) &= C_\mathrm{p}V(t) \end{cases} \tag{4.2}$$

$$\begin{cases} F_\mathrm{p} &= \frac{T_{em}q(t)}{C_\mathrm{p}} - \frac{T_{em}^2(z_3(t)-z_2(t))}{C_\mathrm{p}} \\ F_\mathrm{TM} &= 0 \end{cases} \tag{4.3}$$

The model parameters are estimated by fitting the analytical displacement of the tip $z_3(t)$, obtained solving the system of Equations 4.2, to the measured one $\bar{z}_\mathrm{tip}$. The set of differential equations is solved by numerical integration according to the IDA method ([27]). The target function is minimized by means of a customized routine implementing the quasi-Newton method with a randomly generated initial guess of the parameters. The fitting result is shown in Figure 4.13a, where the measured signal and the fitting function are plotted together.
The identified model is used to predict the axial motion of the plunger which occurred in the in-flight planar release tests, assuming that the flight model dynamics does not differ from the tested EQM.
After solving Equations 4.2, the system of Equations 4.1 may be solved by substituting the mean signals $\bar{x}_1$, $\bar{x}_6$ into $x_{A,f}$, $x_{B,f}$ respectively and the estimated plunger axial motion $z_1(t)$ into $z_{C,f}$. The motion of the plunger in the x−z plane is fully described by the obtained quantities (z_G, x_G, η). The estimated motion of the center of mass of the plunger for the ground tests is shown in Figure 4.13b.

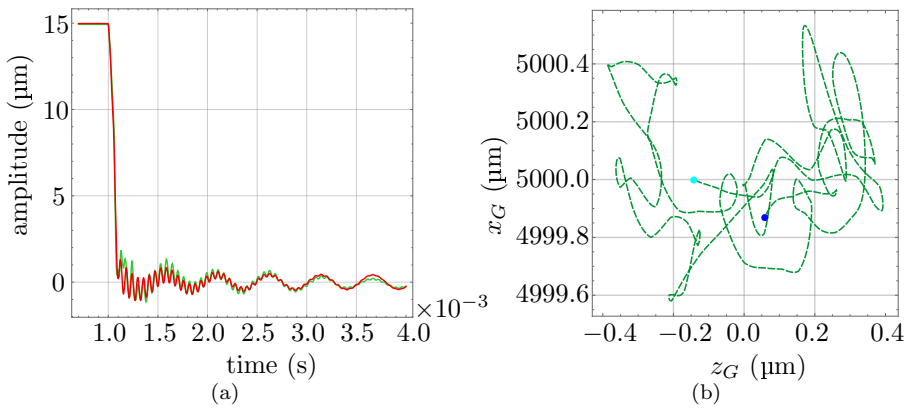

Figure 4.13: On the left, $\bar{z}_{\text{tip}}$ (green curve) and the best fit (red curve). On the right, the estimated trajectory of the plunger center of mass (expressed in the fixed RF). The cyan point corresponds to $t = 1 \times 10^{-3}$ s, while the blue point to $t = 1.7 \times 10^{-3}$ s.

4.3 Analytical model of in-flight release dynamics

This Section focuses on developing an analytical model of the plane collision between the plunger and the TM. In this way, it is possible to estimate the kinetic energy received by the TM after an impact with the plunger excited by the tip retraction.

4.3.1 The effect of the in-flight preload force

The electro-mechanical lumped parameters model developed in Section 4.2 is used to estimate the plunger axial motion at the tip retraction in the flight configuration of the mechanism. The in-flight contact force between the plunger and the TM, that defines the mechanism initial conditions at the release, is provided by the GPRM telemetry signals. In this Section, in order to simulate the in-flight release dynamics, the same model is updated by adding the pre-load force due to the presence of the TM. In the electro-mechanical model, the force exerted on the tip by the presence of the TM is modeled, for any in-flight release, as a negative step (Equation 4.4). This approximation is possible because the force drop time (less than 5 µs) is much smaller than the smallest period of oscillation of the plunger (approximately 60 µs at 17 kHz). The effect of adhesion, here neglected, is taken into account when defining the initial conditions of the TM (in Section 4.3.3).

$$F_{\text{TM}}(t) = \begin{cases} F & t \leq \text{release instant} \\ 0 & t > \text{release instant} \end{cases} \tag{4.4}$$

4.3.2 Plunger-TM plane collision model

Collision models between rigid bodies are widely reported in the literature. In the case under analysis, the simple collision model described in [28] is used. Its basic assumptions are:

- The strains produced by the impact on the two bodies are small if compared to their dimensions.
- The impact forces are much larger than the other forces acting in the mechanical system in the same time-frame.
- The impact time is negligible with respect to the analysis time, i.e., instantaneous collision.
- The analysis is planar, i.e., bi-dimensional problem.
- The bodies collide only one time.
- The friction coefficient is negligible during the impact, i.e., the impulse received by the TM is orthogonal to the impacting surface.
- The restitution coefficient e_k is set equal to 1, i.e., perfectly elastic collision, in order not to underestimate the kinetic energy transferred to the TM.

The assumptions are justified by the analysis of the in-flight data, as discussed in Section 2.6, and by the geometry and the material properties of the bodies. Given the previous considerations, the collision can be described by a system of ten equations with ten unknowns, that is reported in Appendix B. The inputs of the system are the positions and velocities of the center of mass of the bodies before the collision (superscript i). The outputs are their velocities after the collision (superscript f). Those quantities are computed with respect to a reference frame centered on the collision point of the two bodies, with the x axis tangential to the colliding surfaces and the y axis orthogonal to them.

4.3.3 Validation of the TM release dynamic model with the flight data

In Sections 4.3.1 and 4.3.2, the updated electro-mechanical model and the plane collision model are presented. Combining them, knowing the collision instant, it is possible to compute the TM angular and linear velocity after an impact with the plunger and, therefore, its kinetic energy. However, due to the deviation of the real system with respect to the nominal design, the in-flight configuration of the system and the instant of the impact are unknown. This analysis therefore aims at proving the compatibility of the measured signals with respect to the hypothesis of plunger-TM impact, for the reliable tests performed in-flight.
A strong argument in support of such a hypothesis is the orthogonality of the estimated impulses with respect to the mechanical interface between the plunger and the TM, described in [14]. In the present thesis, the assessment of compatibility to the impacting body (i.e., the plunger) is extended, focusing on the kinetic energy acquired by the TM after the impact.
When the plunger oscillates after the tip retraction, it results in a sequence of positions and velocities some of which may constitute initial states at the impact. In particular, an impact is possible when the plunger approaches the TM and occurs when its displacement equals the available gap (see Figure 4.14).

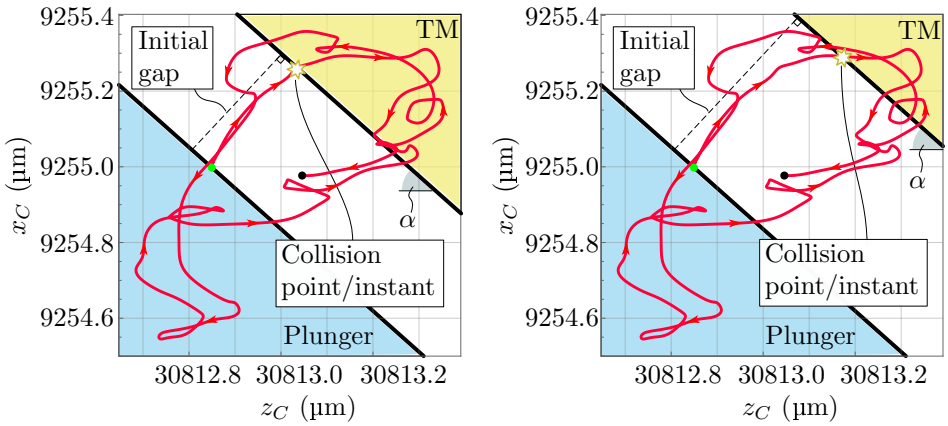

Figure 4.14: Estimated trajectory of a point on the plunger head in the case of 0.3 N pre-load force. Referencing to Figure 4.13b, the green point corresponds to $t = 1 \times 10^{-3}$ s, while the black point to $t = 1.7 \times 10^{-3}$ s. Two cases are depicted, with different initial gaps, which correspond to different collision instants.

For this reason, the plunger motion, estimated using the updated electro-mechanical model, yields the sequence of possible plunger initial conditions. On the other side, the initial angular velocity of the TM and its linear velocity along x are set equal to zero, while the linear velocity along z is set equal to ι_z^{res}/m (see Equation 2.10 for reference). In fact, before any collision with the plunger, the TM is moving with velocity ι_z^{res}/m along z-axis according to the advanced impulse model.
The position of the predicted contact point C is estimated from the CAD model of the mechanism. Even if it is not possible to know a priori its exact position on the TM and on the plunger, the particular geometry of the mechanism limits its position to a narrow region with respect to the dimensions of the bodies, as shown in Figure 4.15.

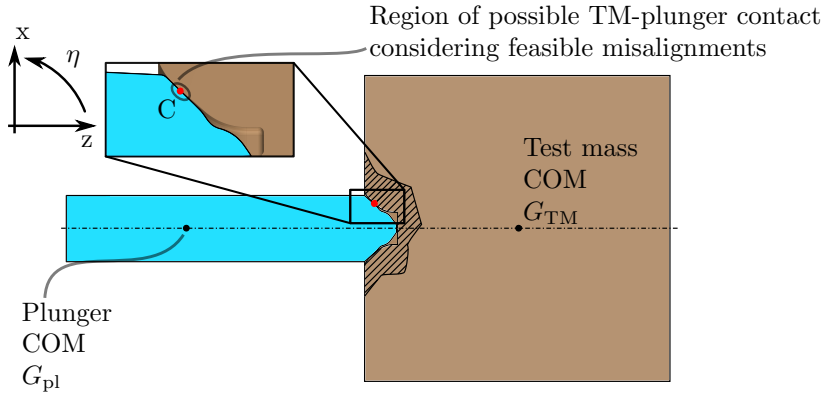

Figure 4.15: Estimated contact point C from the CAD model of the GPRM. The exact location of the contact point is not known a priori but the region where it is located is narrow with respect to the dimensions of the bodies. The centers of mass (COMs) of the TM (G_{TM}) and the plunger (G_{pl}) are shown.

The estimation of the TM state after an impact with the plunger relies on the calculation of two relevant quantities. The first is the available gap, that is the distance between the TM and the plunger in the direction orthogonal to the colliding surfaces (i.e., orthogonal to the TM indent surface). This quantity is useful since an impact is possible only when the plunger is moving toward the TM, i.e. the gap is reducing. The second relevant quantity is the TM kinetic energy predicted by the collision model if an impact occurs at the generic time instant t. This kinetic energy is compared with that measured in-flight.
An example of the mentioned quantities, related to one of the in-flight tests, is plotted in Figure 4.16, showing that the model-predicted kinetic energy is compatible with the one measured in-flight.

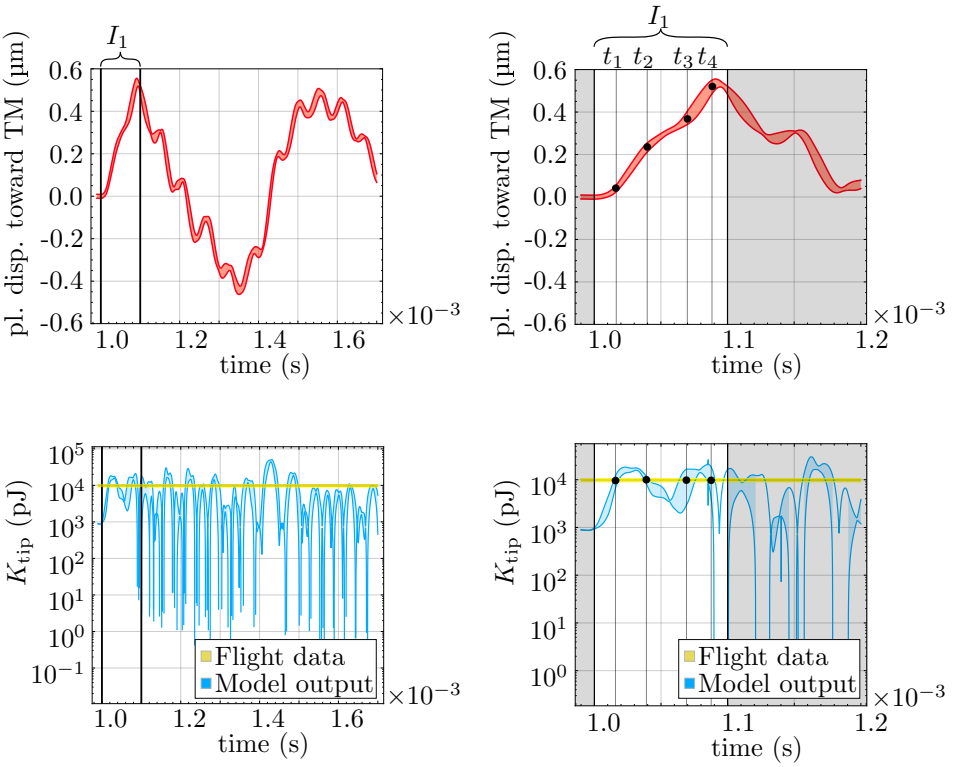

Figure 4.16: On the top left, distance between the TM and the plunger in the direction orthogonal to the colliding surfaces (red curve). On the bottom left, logarithmic plot of the predicted TM kinetic energy after the impact with the plunger at the generic time instant t (blue curve) together with the kinetic energy measured in-flight (yellow line). On the right, same graphs magnified in the time interval of interest. The plotted curves are represented by bands derived from the propagation of the uncertainty in the model parameters and in the measurements.

From the top left graph, the intervals in which the TM-plunger collision may occur can be spotted. The intersections between the yellow and the blue curves

inside those time intervals represent the possible collision time instant in which the in-flight measurements are compatible with the predictions of the model. In this particular case, which also resembles the other tests, a single time interval of possible collision is present and is named I_1. In fact, since the TM velocity before the impact is negligible with respect to the velocity of the plunger, the collision can occur only when the plunger is moving toward the TM and has not reached its maximum amplitude of motion. In other words, given an initial plunger-TM relative configuration compatible with an impact, this must take place during the first approach, because the following oscillations do not add any additional plunger-TM collision configurations. Furthermore, even considering the following intervals the maximum TM kinetic energy produced by an impact with the plunger remains in the same order of magnitude. The analysis of the kinetic energy estimated by the model should be restricted only in this time interval, as depicted by the shaded areas in the graphs on the right. In the depicted case, there are four possible time instants (t_i, for $i \in \{1, 2, 3, 4\}$) in which the predicted kinetic energy is compatible with the measured one.
The following considerations remain valid for all the in-flight tests under analysis. The kinetic energy predicted by the model in the time intervals of interest is compatible with that measured in-flight, and at least one time instant of possible collision exists, which explains the kinetic energy measured in-flight. The estimated initial gaps fall in the range from 0 µm to 0.5 µm approximately. This confirms that the TM is much closer to the plunger with respect to the nominal case (9.3 µm).
The same analysis is carried out considering that the impact between the TM and the plunger occurs on the region diametrically opposite to the one reported in Figure 4.15. In this case, the substantial difference is that the maximum distance traveled by the plunger toward the TM is approximately 0.2 µm instead of the 0.6 µm of the previous case. The kinetic energy acquired by the TM after the impact has the same order of magnitude as the one of the first case, represented in Figure 4.16. Therefore, in both cases, the impact model leads to the same conclusions.

4.4 Model extension: continuous push

The model presented in Section 4.3 considers the kinetic energy transferred from the plunger to the TM in the case of an instantaneous impact takes place between the two bodies. A new model is now developed to cover another possible case of interaction, i.e., a non-instantaneous push of the plunger on the TM. The main hypothesis which differentiates the new model from the previous one is that the TM and the plunger are already in contact before the tip retraction.

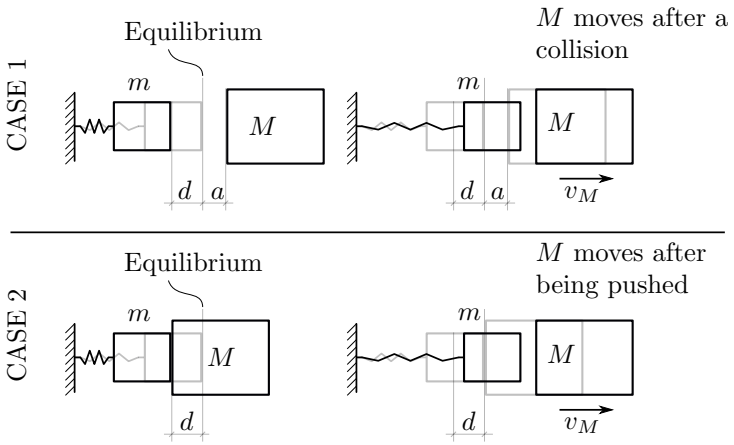

Figure 4.17: Cases of interaction between a single DOF oscillator and an external mass M.

Before introducing the model, a simplified case is presented. Consider the 1 DOF oscillator, mass m and stiffness k, depicted in Figure 4.17, that interacts with a mass M in two different ways. The first case consists in preloading the oscillator (initial deformation $-d < 0$) and positioning the mass M at a distance $|a| < d$ from the equilibrium. When the mass m is left free to oscillate, it will impact the mass M. Under the assumption of elastic collision, the final velocity, i.e., post impact, of the mass M is easily computed, as shown in Equation 4.5.

$$v_{M,1} = \frac{\sqrt{d^2 - a^2}\sqrt{k}}{\sqrt{m+M}}\sqrt{\frac{m}{M}} \tag{4.5}$$

The maximum value of $v_{M,1}$ is obtained for $a = 0$, as shown in Equation 4.6.

$$v_{M,1,\max} = \frac{d\sqrt{k}}{\sqrt{m+M}}\sqrt{\frac{m}{M}} \tag{4.6}$$

The second case consists in positioning the mass M in contact with the oscillator mass m (preloaded with the same initial deformation $-d < 0$) before releasing it. In this case, the former will be pushed by the latter until the maximum velocity is reached, i.e., when the equilibrium position is crossed. At that instant, the bodies will detach since the mass m will be slowed down by the spring. The maximum velocity reached by the mass M in this case is shown in Equation 4.7.

$$v_{M,2,\max} = \frac{d\sqrt{k}}{\sqrt{m+M}} \tag{4.7}$$

Comparing Equations 4.6 and 4.7, the maximum velocity obtained in the second case is greater than the one of the first case if $M > m$. This is indeed the case of the LPF release mechanism. The mass of the TM is much greater than the mass of the plunger. Thus, the model of a push of the plunger against the TM at the release is expected to generate greater release velocities if compared to the collision model previously discussed.

In order to model the push of the plunger, a simplification is introduced. In particular, the plunger lateral motion is neglected, and only the axial motion is considered. Thus, the plunger is constrained to move along z axis. The dynamical model used here to describe the plunger motion along the z axis is the same used in Section 4.2. The contact of the plunger with the TM is modeled introducing a frictionless revolute-translational joint between the two bodies in the TM indent surface (see Figure 4.18). The initial velocities of the TM and the plunger are set equal to zero. The initial rotation of the TM ($\eta_{\mathrm{TM}}(0)$) is set equal to 0, the initial positions of the TM and the plunger depends on the preload force, which is considered as an independent variable.

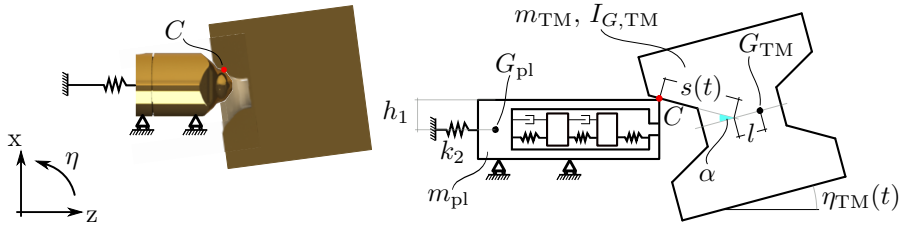

Figure 4.18: Scheme of the TM plunger interaction model in the case of a TM already in contact with the plunger before the release. In the contact point (red dot) there is a revolute-translational joint.

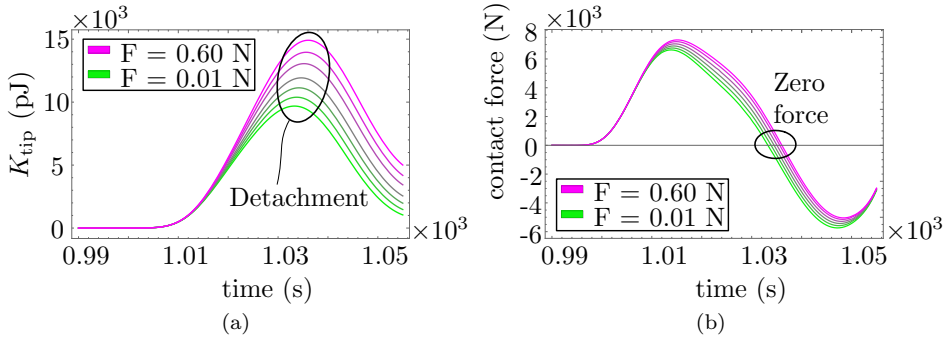

Figure 4.19: Results of the model involving a continuous push of the plunger on the TM. The contact is not instantaneous and takes place in a time interval of approximately 0.03 ms.

The model is solved for different preload values, in the range from 0.01 N to 0.60 N, which are similar to the values observed in-flight. In Figure 4.19 the outcomes of the model are plotted. In particular, on the left plot, the kinetic energy of the TM (K_{tip}) as a function of time is shown. The detachment of the TM from the plunger takes place when the TM reaches its maximum kinetic energy, which is approximately at 1.03 ms (the tip retraction is at 1.00 ms). In fact, observing the right plot, at this time instant the force exchanged by the TM and the plunger is

zero. Considering the maximum of K_{tip} as a function of the preload force, it can be presented in a graph and compared to the in-flight data, as shown in Figure 4.20. The proposed model, while being relatively simple and with the limitation of the purely axial plunger motion, should return an upper limit of the TM release kinetic energy (K_{tip}). The prediction of the model is in accordance with the in flight data. The maximum kinetic energy measured in-flight at different preload force is close to the one predicted by the model.

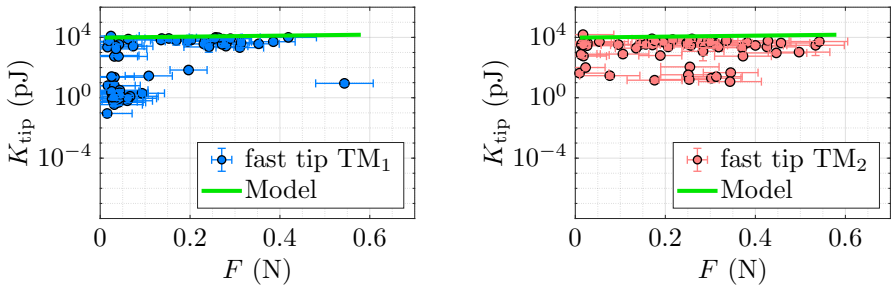

Figure 4.20: Graphs of the TM kinetic energy at the tip retraction as a function of the preload force at pre-release. The in-flight data are in accordance with the model prediction.

In this Chapter, the kinetic energy of the TM at the release has been interpreted with two different models. The first model considers the impact with the oscillating plunger in the presence of an initial TM-plunger gap and can explains all the reliable in-flight tests which resulted non-nominal (with different levels of release kinetic energy). The second model may explain only the tests where the TM has the highest level of kinetic energy. Thus, given the mechanism geometrical and physical parameters, it is useful to define an upper bound of the kinetic energy transferable to the TM.

Chapter 5

Conclusions and future developments

This Chapter, in the first part, briefly summarizes the analysis performed and the main results presented in this thesis. The main conclusions are taken from [29]. In the second part, possible improvements of the grabbing positioning and release mechanism are presented. Those improvements are useful for the forthcoming LISA mission, where the lessons learnt in LPF will be of considerable value.

5.1 Main conclusions

The LISA Pathfinder mission unquestionably represents a great success for the scientific community. The mission demonstrated the achievement of the technological maturity required for the gravitational wave measurement from space. The strict mission requirements imposed on the relative acceleration of the two free-falling TMs, sensing bodies of the experiments, were fulfilled with a large margin.
Even if the mission was a success, some unexpected complications occuring before the start of the science phase, had to be overcome. In fact, the analysis of the in-flight telemetry data showed that the two TMs, hosted in the GRSs, were released into free-fall with unexpected residual velocities, that exceeded the maximum requirements.
As a consequence, an additional in-flight test campaign was carried out at the end of the mission in order to implement different TM release strategies. Unfortunately, the two release mechanisms behaved differently under the same testing conditions, therefore no optimal release strategy was found. Moreover, the adopted release strategies present some drawbacks.
For example, a significant rotation of the TM about φ angle before the release was induced by the hammering maneuver. Interpreting what caused the unexpected release dynamics of LPF mission is a challenging problem since the GRS design aims at minimizing the acceleration noise at low frequency (1-30 mHz) rather than provide high-frequency signals of the TM dynamics and an accurate diagnostic of the mechanisms involved. Nevertheless, understanding the main causes of the ob-

served dynamics is critical for the implications in the forthcoming LISA mission. The analysis of the telemetry signals suggests that, in most cases, impacts occurred between the GPRM plungers and the TM, however little information is available to confirm this hypothesis and to understand the criticalities of the mechanism.
The compatibility of the proposed explanation with the GPRM dynamics is verified in this manuscript through a combined experimental-analytical approach, based on dedicated tests performed on ground on an EQM of the GPRM. An electro-mechanical model of the mechanism is validated and used to predict the effect of the plunger vibrations in the x−z plane on the in-flight release velocity of the TM, involving a possible impact.
The results of the analysis provide evidence that the in-flight behavior of the reliable and non-compliant TM releases was caused either by TM-plunger impacts or by a static push applied by the plunger to the TM.
Regarding the model involving impacts, the first collision takes place at the tip retraction step of the injection procedure, due to insufficient clearance between the two bodies. The proposed model makes it possible to draw some conclusions concerning the mechanism design, development and in-flight operation, summarized in Figure 5.1. The contour plot shows the predicted kinetic energy acquired by the TM (K_{tip}) at the impact with the plunger, normalized by the maximum requirement, as a function of the initial gap with respect to the plunger and the preload force.

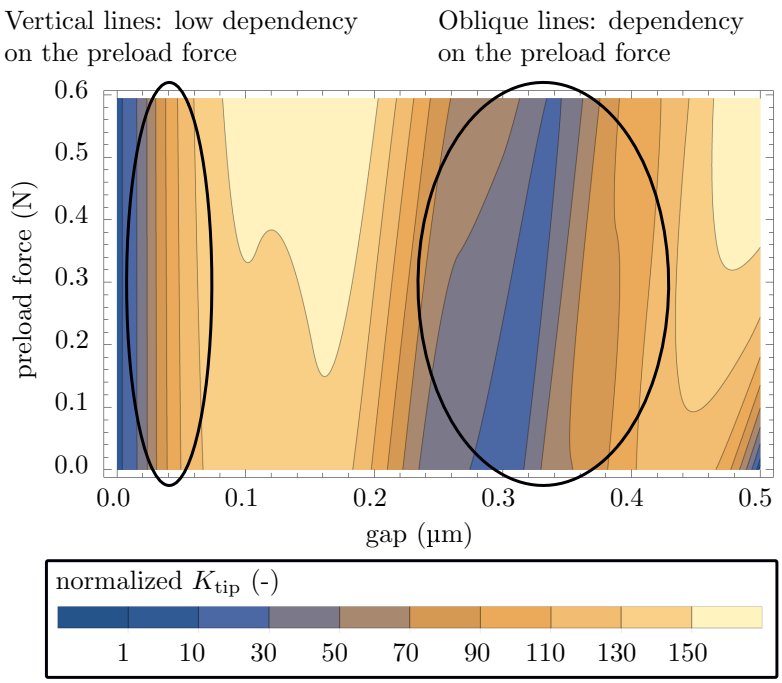

Figure 5.1: Contour plot of the kinetic energy of the TM as a function of the TM-plunger gap and the pre-load force predicted with the analytical-experimental model involving a TM-plunger collision.

Some regions of the domain are characterized by a TM state close to the requirements. However, they cannot be reached through the only controllable variable (the preload force) since the contour lines lie almost parallel to the vertical axis. This means that the current criticality may not be overcome by an improvement of the preload control system, but an adequate plunger-TM clearance needs to be guaranteed in the release configuration.
The plot region where the gap tends to zero is not appropriately described by this plot. In this case the kinetic energy of the TM is better described by the model of a static push of the plunger, developed in Section 4.4, where the TM and the plunger are already in contact before the release.
Considering the results of the impact model and the static push of the plunger, it can be stated that the energy stored in the mechanism, in the form of potential energy in the actuated piezo stack and elastic energy stored in the deformable components due to the preload force, is more than sufficient to produce a TM velocity out of the requirements.

The picture of compatibility here proposed covers the in-flight tests which present reliable signals, i.e., characterized by easily identifiable impacts and with good signal to noise ratio. However, some tests are available which requires further investigations, possibly involving a full three-dimensional approach and more relaxed hypotheses about the nature of the TM-plunger contact (for instance, the case of multiple impacts).
This may constitute an interesting development, which however is quite demanding and requires further investigations (the topic is briefly addressed in Chapter 6), analysis and test on the mechanism. Moreover, the question of strong anisotropy of the mechanism behaviour (preferred impact plane x−z) seen from the analysis of the in-flight tests may be addressed by a deep study of the NEXLINE linear actuator.
It useful to recall that a deep comprehension of the criticalities of the current GPRM design related to the TM release and injection in the geodesic trajectory may be instrumental in the improvement of the mechanisms to be flown in LISA.
The next steps of the GPRM analysis are currently being carried on by the Author, along with colleague E. Dalla Ricca, under the supervision of Prof. D. Bortoluzzi. Currently, new experiments are being designed and an improved mathematical model of the plunger dynamics is being developed. The model takes into account both the axial (z) and the lateral motions (x and y) of the plunger triggered by the quick retraction of the tip and is being fitted thanks to several new measurements collected with the existing experimental setup. In the future, the model may be utilized as a useful tool for the definition of the GPRM requirements and the qualification of the new units.

5.2 Possible GPRM improvements

In this Section, some improvements to the GPRM design are proposed and briefly discussed, starting from the ideal strategies and later listing more practical solutions.
Ideally, two different strategies are possible to improve the release performance of

the GPRM, i.e., I) maximizing the clearance between the TM and the oscillating plungers at the pre-release or II) minimizing the plunger motion at the tip retraction as well as reducing its deviation from the straight line trajectory when the NEXLINE is activated. Of course, any combination of such methods would benefit in terms of the mechanism release performance.
Regarding the increase of the clearance, one of the best ways to accomplish such an objective would be to introduce another actuator, coaxial to the plungers, that has the function of stepping away the plunger pyramidal and conical surfaces from the TM indents in a sort of middle phase between the TM repositioning and the actual handover to the tips.
The concept is essentially to further separate the functions of the GPRM described in Table 1.3. This is done by splitting the centering function, achieved by the form fit of the plungers and the indents, from the locking function before the handover. A possible example of such a modification is depicted in Figure 5.2, where an added end-effector is sketched during the steps of the *updated handover* phase. The final configuration of the mechanism is characterized by a higher TM-plunger clearance, since the second actuator could be designed with a stroke much greater than the piezo-stack actuating the tip. Such a design would make unnecessary the hammering maneuver (preventing the TM φ rotation that may follow it, see Section 2.5).
The depicted upgraded is just an example, which is not worth analyzing further, since such a modification is not possible, because it would require a complete redesign of each GPRM unit. Moreover, also the existing electronics would require major modifications.
Thus, other minor modifications to the LPF release mechanism are proposed in the following, with the objective to realize the two ideal strategies introduced. Those modifications may eventually be applied to the flight models of LISA. In fact, some of those design improvements have been already discussed with partners from the industry and addressed as practicable solutions to reduce the risk of high residual velocities at the release (see Table 5.1).

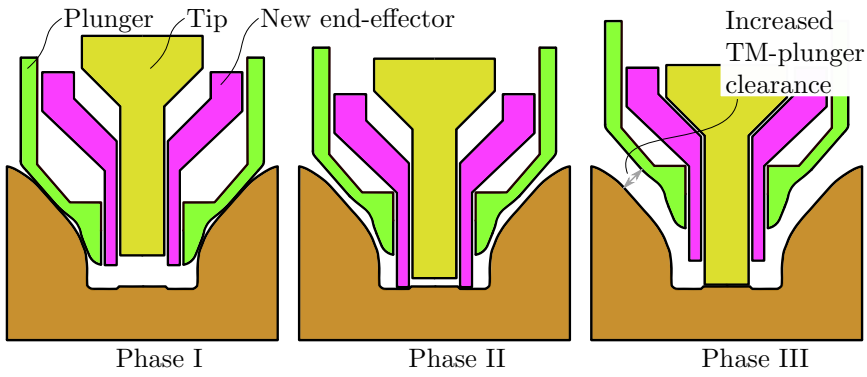

Figure 5.2: Upgraded handover procedure where a new actuator/end effector is introduced. The new end-effector has the function of separating the plunger and the TM before extracting the tip (phase II), thus there is enough clearance when the release (i.e., tip retraction) is performed. Drawing not to scale.

Linear runner sensors and actuator

The linear runner state is monitored measuring two quantities, which are its linear position along z axis and the preload force exerted on the TM. The position sensor has a dead zone in the mid-range of motion, moreover it is affected by $\approx 1\,\mu m$ (standard deviation) noise and some hysteresis, so its information is difficult to exploit. Substituting the sensor with a more precise one, without the dead zone, would make it possible to understand if the TM has been successfully grabbed checking the sum of the position sensors. Indeed, such a quantity should remain constant, once the TM is properly grabbed, independently from its z position.
As discussed in Section 2.5, the pre-load force on the TM before the release is affected by large uncertainty and offset with respect to the desired preload value (sometimes the preload drop before and after the release is compatible with zero). In order to improve the repeatability of the injection procedure (in particular the handover and the release phases), a more precise and more accurate force sensor is required.
Following this idea, the NEXLINE micro-stepping function should be implemented, since a fine position control of the linear runner is critical to generate the desired preload. It would also allow for a more controlled hammering procedure. The reduction of the minimum step-size of the NEXLINE may be achieved modifying the voltage control provided to the NEXLINE, without the necessity of hardware modifications.

Linear runner stiffness

The force measurement of the GPRM is based on the compliance of the bridge connecting the linear runner with the plunger. The overall stiffness of the GPRM depends on several components, in series with the force sensor. As discussed in Chapter 4, the plunger motion after the tip is retracted depends on the overall compliance. On one hand, a stiffer mechanism would minimize the overshoot motion amplitude of the plunger towards the TM, thus reducing the risk of a collision, on the other hand, following problems are detected:

- The NEXLINE stiffness cannot be modified at will, as it depends on the manufacturer. The properties of the latest developed versions may be different with respect to the LPF configuration.
- Increasing the stiffness of the force sensor will lower its sensitivity, in conflict with the need to improve the force measurement precision and accuracy. An alternative solution would be to redesign the force sensor.
- The stiffness of the stacks is hardly modifiable, especially because their length is not to be reduced (being proportional to the stroke).

Linear runner/plunger side guiding

As shown by on-ground testing and confirmed by in-flight data, the motion of the plunger along z axis, governed by the actuation of the NEXLINE, suffers from large rotations and bi-stable configurations any time the motion is reversed. This

is an important factor that contributes to reducing the TM-plunger clearance at the release. A possible solution is to study different materials and minor design changes to be implemented in the slider-roller coupling, minimizing the friction of the slider. In this way, it is possible to increase the lateral preload of the constraining guide, reducing the bi-stability, and maybe to improve the motion precision, reducing the linear runner rotation.
The linear motion functionality should be characterized on ground, to understand if the rotations are compatible with a nominal GPRM-TM configuration at the release, repeating the tests after repositioning the TM in the center from different locations.

TM/plunger interfaces

As shown in Section 2.5, for some in-flight tests, the plunger was stuck in the TM indent in pre-release conditions with the TM rotated about φ. This implies that the retracted tip is at a large distance from the landing area, making its extraction (handover) ineffective. The improvement of the force and position sensors of the linear runner, already discussed, may be useful in detecting eventual stuck conditions. In order to reduce the risk of a stuck TM, a non-trivial re-design of the plunger head and the TM indent geometry profile may be considered.
During on-ground testing, it may be investigated if the friction arising at the interface is increased by plunger-TM misalignments, i.e., a relative configuration different from the nominal design. In addition, the improvement of the machining tolerances of the plunger heads (measured deviations of about 100 µm) may be useful to guarantee a release under nominal conditions and sufficient TM/plunger clearance.
Apart from re-designing the interfaces, another important improvement would be to define a GPRM-plunger reference frame close to the head of the plunger, in order to avoid the problems highlighted in Section 3.1.6. As was discussed, the results of the alignment procedure where not compatible with the in-flight measurements. In particular, the in-flight TM_2 φ angle was not inside the requirement (± 2000 µrad) on average and was different from the alignment realized on-ground.

Increased tip stroke

Increasing the stroke of the pin would increase the gap margin between the TM and the plunger, thus limiting the risk of impacts. This may be achieved by commanding both piezo-stacks simultaneously when extracting and retracting the tip. Such a strategy would double the total stroke of the tip, increasing the clearance. Actuating both the piezo-stacks (the nominal and the redundant ones) means that the mechanism has a hot redundancy, i.e., if one of the two actuators fails the handover and release phases have to be performed with only one piezo-stack. The latter case is in fact the one used in LISA Pathfinder so it should not correspond to a decrease in performance with respect to the nominal release procedure.
The realization of a larger stroke adopting longer piezo-stacks is limited by the available space in the axial direction (z axis of the GRS RF). This limit may be overcome by introducing a telescopic actuator, exploiting the free space available on the sides of the piezo-stack (see Figure 5.3).

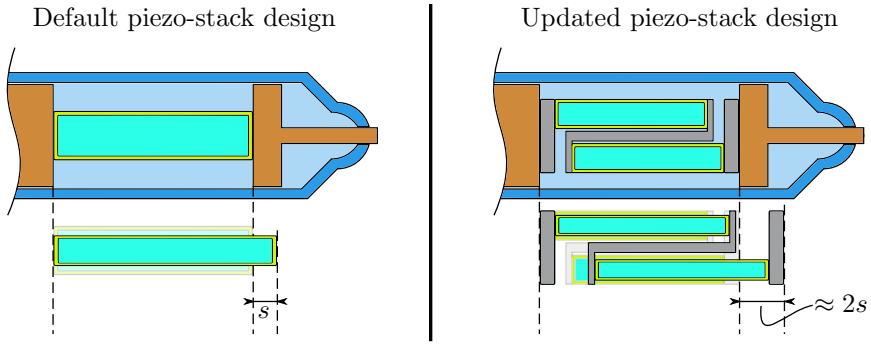

Figure 5.3: Comparison between the default design of a single piezo-stack actuator (on the left) and the modified one (on the right). The proposed solution exploits the available empty space on the sides of the stack to almost duplicate the maximum tip stroke, called s.

Another possible way to increase the tip stroke would be to adopt a different actuator, characterized by a greater range of motion with respect ot the piezo stack actuator used in LPF. As observed from the analysis of the in-flight tests, the slow tip retraction is sufficient to break the adhesive bonds on the landing areas so the new actuator is not required to retract the tip as fast as the piezo solution. This solution has the advantage of minimizing the plunger oscillations when a slow tip retraction is performed.

Electrical isolation of the plungers and the release tips

In order to improve the reliability of the GPRM, it is proposed to electrically isolate the plungers from the release tips. This modification will require to add two additional electric lines to provide the injection voltage to the TM via the tips when in pre-release conditions. The main idea behind the electrical isolation is that, in this way, it is possible to verify if there is a TM-plunger contact before retracting the tips just by checking the electrical continuity of the related circuit. By implementing such a check in the injection procedure control algorithm, it would be possible to repeat the handover, or re-perform the hammering maneuver, until the electrical contact is no more detected. In this way, the TM release has a higher probability of being successful.

Proper testing of the release performance

In order to fully test the release performance of the GPRM, one should test it in outer space representative conditions. While some the characteristic of outer space environment can be easily reproduced on Earth (e.g., extremely low pressure or typical spacecraft temperature) the absence of gravity is difficult to achieve.
Every on-ground testing aimed at predicting the residual velocity of a released body is heavily affected by the 1-g environment. There are ways to partially overcome this problem, for example using suspended pendulums or low friction air tables, but they all have the limitation of constraining the release body motion to less

than six DOFs.
Thus, a possible way to test the GPRM performance in fairly representative way would be to separately test it on two different orthogonal planes (x−z−η and y−z−θ). A possible idea may be to utilize a setup where the TM (or a dedicated mock-up) is suspended on a floating table. In this way, its linear and angular displacements on the plane would not be constrained. Such a setup has the drawback of constraining the TM φ rotation. The φ dynamics may be studied setting the z axis orthogonal to the floating table, and performing a half release using the GPRM −z unit (the only unit that can produce a relevant ω_φ of the TM, due to the pyramidal shape of the plunger head).
Another idea, to overcome the problem of the separation of the orthogonal planes, would be to mount the GPRMs and the TM in an airplane that performs parabolic flights, which are offered by ESA to scientists to conduct particular experiments. Typically, a parabolic flight lets the users to exploit 20 seconds of micro gravity (i.e., close to 0-g environment) per parabola, which should be enough to release the TM and capture it immediately after with the plungers.

Table 5.1: Possible GPRM improvements discussed with partners from the industry.

What	**Why**	**How**	**Who**	**HW mod.**
Ensure maximum penetration of plungers when grabbing the TM	Implement a correct grabbing	Check TM φ rotation	FEE sensing readout	No
		Improve plungers position sensor precision	GPRM position sensor	Yes
		Hammering procedure	In-flight operational procedure	No
Ensure grabbing force >0 N	Avoid TM angular vel. ω_φ at pre-release after hammering	Reduce noise of force sensor readout	GPRM force sensor	yes
Ensure TM/plunger pre-release clearance	Prevent TM/plunger collision after release	Check TM/plunger relative position and attitude	FEE sensing readout	No
		Increase maximum tip stroke	GPRM tip actuator	Yes
		Re-design the pyram. plunger head to avoid stuck TM	GPRM plunger heads	Yes
		Re-design the plunger heads to increase clearance with the TM in the radii zones	GPRM plunger heads	Yes
Reduce plunger oscillation triggered by the tip retraction	Prevent TM/plunger collision at release	Slow tip release and slow plunger retraction strategies	In-flight operational procedure	No
		Improve design and materials	GPRM linear guide mechanism	Yes

Chapter 6

PhD activities

6.1 Original contributions and scientific production

The main research activity carried out by the Author during his PhD studies was conducted in the frame of a collaboration between the University of Trento and the LISA Pathfinder project partners. As a consequence, the procedures and findings discussed in this thesis up to Chapter 5 are specifically related to the mission itself rather than to a more general theoretical or experimental field. Even if the Author research was constrained to the LPF frame, original contributions of scientific interest were still developed. Most of the contributions, which were published in International Journals or Conferences, come from the following Chapters:

- In Chapter 2, in particular in Section 2.6, where the in-flight data are analyzed, a model of the impulses arising at the release is developed. The model allowed to understand that the plunger is the culprit of the un-expected TM release dynamics.
- In Chapter 4 the TM-plunger interactions are modeled exploiting an existing experimental setup. The setup was modified in order to measure the oscillations of the plunger triggered by the fast tip retraction. The experimental results are in agreement with the in-flight data.

Part of the arguments reported in this thesis have been published in the following scientific works.

Conference talks

- D. Vignotto, D. Bortoluzzi and A. Zambotti, **Object release into free-fall: a technological challenge for in-space gravity waves detection**. Oral presentation at the *Space Satellite Conference*, Rome, June 2018.
- D. Vignotto, D. Bortoluzzi and A. Zambotti, **LISA Pathfinder: A technology demonstrator mission for future in-space gravitational wave**

detection. Co-author of a presentation at the at the *Space Satellite Conference*, Rome, June 2018.

- D. Bortoluzzi, A. Zambotti, D. Vignotto, I. Köker, H. Rozemeijer, J. Mendes, P. Sarra, A. Moroni, P. Lorenzi and the LISA Pathfinder collaboration, **In-flight testing of the Injection of the LISA Pathfinder Test Mass into a Geodesic**. Co-author of a presentation at the *12th International LISA Symposium*, Chicago, July 2018.

- D. Bortoluzzi, D. Vignotto, E. Dalla Ricca and the LISA Pathfinder collaboration, **Latest development in the analysis of the grabbing positioning and release mechanism performance**. Oral presentation at the *13th International LISA Symposium Online Conference*, September 2020.

- D. Bortoluzzi, D. Vignotto, Andrea Zambotti, E. Dalla Ricca, J. Conklin, I. Köker, R. Gerndt, H. Rozemeijer, P. Sarra, A. Moroni, P. Lorenzi and the LISA Pathfinder collaboration, **A challenging technological problem: the injection of the LISA Pathfinder test mass into a geodesic**. Oral presentation at the *43rd COSPAR Scientific Assembly*, Sydney, January-February 2021.

Conference papers

- D. Bortoluzzi, D. Vignotto, A. Zambotti, I. Köker, H. Rozemeijer, J. Mendes, P. Sarra, A. Moroni, P. Lorenzi and the LISA Pathfinder collaboration, **Analysis of the in-flight injection of the LISA Pathfinder test-mass into a geodesic**. In *18th European Space Mechanisms & Tribology Symp. (ESMATS)*, Monaco, September 2019.

- D. Bortoluzzi, E. Dalla Ricca, D. Vignotto, W. J. Weber, P. Sarra, **Testing the impact dynamics of the LISA Pathfinder release mechanism**. In *19th European Space Mechanisms & Tribology Symp. (ESMATS)*, Online, September 2021.

Journal papers

- D. Bortoluzzi, D. Vignotto, A. Zambotti and the LPF collaboration, **In-flight testing of the injection of the LISA Pathfinder test mass into a geodesic**. In *Advances in Space Research*, August 2020 (Copyr. Elsevier).

- D. Bortoluzzi, D. Vignotto, E. Dalla Ricca, J. Mendes, **Investigation of the in-flight anomalies of the LISA Pathfinder Test Mass release mechanism**. In *Advances in Space Research*, May 2021 (Copyr. Elsevier).

6.2 PhD experiences

During his PhD studies, the Author had the privilege to attend several courses, school and seminars, which were of great interest and in some cases directly helped him in his main research topic. Another important experience that the author is

honored to have had was that of teaching. He firmly believes that teaching a given subject is the best way to fully understand it.

6.2.1 Courses

- Academic Writing (Prof. F. Hope).
- Basics of Reliability Engineering (Prof. M. Brunelli).
- Design of Transducers based on Smart Materials and Structures for Robotics and Energy Harvesting (Prof. M. Fontana and PhD G. Moretti).
- Numerical Optimization Algorithms and Practical Implementation (Prof. E. Bertolazzi).
- Scientific Programming (Prof. E. Bertolazzi).
- Non-linear Vibrations (Prof. D. Bortoluzzi).
- Optimization Robotics (Prof. A. Del Prete).
- Satellite Orbits: Numerical Simulation with Matlab (Prof. J. W. Conklin).
- Systems Identification (Prof. G. Panzani and S. Formentin).

6.2.2 Schools

- Data-driven Model Identification of Dynamical Systems, 2nd Spring Doctoral School, Nancy (France), March 2018.
- Multibody Dynamics Workshop 2019, 2nd International Multibody Summer School, Parma (Italy), May 2019.

6.2.3 Teaching activities

- Teaching assistant for the Master Degree course in Mechatronics Engineering of Mechanical Vibrations (main lecturer Professor D. Bortoluzzi). The author was selected as the teaching assistant for this course for three consecutive years (2018, 2019 and 2020). During the second year, he designed an experiment for the students modifying an existing setup and converting it into a Frahm absorber device.
- Main lecturer at a pre-university course of Applied Mechanics for the Istituto Tecnico Tecnologico G. Marconi (Rovereto).

6.3 Parallel research activities

Apart from the main research topic, i.e., the understanding of the GPRM release dynamics, other research activities have been carried out by the Author during his PhD studies. Those parallel research topics are briefly described in the following, since they constitute a significant part of the overall work and may constitute the basis for future journal and/or conference publications.

6.3.1 Characterization of the voltage profile of a capacitor

During the PhD course of Design of Transducers Based on Smart Materials, the Author and two other students (M. Nardello and P. Tosato) developed an experimental setup aimed at verifying an analytical model developed by PhD G. Moretti. In particular, the experiment regarded the charging dynamics of a planar circular capacitor.

Model equations

In Figure 6.1 the geometrical parameters of the circular capacitor studied are shown. Apart from the parameters in the image, other useful physical quantities that characterize the system are the electrical conductivity k_E (the reciprocal of electrical resistivity ρ_c), measured in $\mathrm{m}^{-1}\,\Omega^{-1}$, and the permittivity of the dielectric ϵ, measured in $\mathrm{F\,m}^{-1}$.

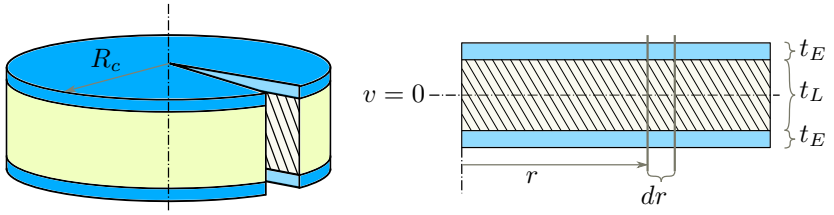

Figure 6.1: Sketch of a plane circular capacitor with the main geometrical quantities defining it.

The analytical solution of the differential equation governing the voltage profile of the capacitor surface in case a sinusoidal voltage $V(t) = V_0 \sin(\omega t)$ is applied to the boundary is expressed in Equation 6.1. To obtain the solution, the differential Equation governing the electrical equilibrium of the capacitor is solved with the method of variables separation.

$$v(r,t) = V_0 \sin(\omega t) - V_0 \sum_{n=1}^{\infty} \frac{2\alpha\beta_n^2\omega}{z_n(\alpha^2\beta_n^4+\omega^2)} \frac{J_0(\beta_n r)}{J_1(z_n)} \left(\cos(\omega t) + \frac{\omega}{\alpha\beta_n^2}\sin(\omega t) - e^{-\alpha\beta_n^2 t}\right) \quad (6.1)$$

Where J_0 and J_1 are two Bessel's functions of first type, z_n is the n-th zero of the function J_0, and β_n is defined as z_n/R_c, with R_c the external radius of the capacitor. The parameter α is defined as $\frac{k_E t_E t_L}{\epsilon}$ and is measured in $\mathrm{m^2\,s^{-1}}$. The solution contains an exponential term, $e^{-\alpha\beta_n^2 t}$, which represents the transient part of the equation. In steady state the exponential term is negligible.
In Figure 6.2 the analytical solution with a 1 MHz input voltage frequency is plotted for different time instants, expressed as function of the period of the external voltage, $T = 2\pi/\omega$. On the left, the initial time instants are plotted, showing the transitory part of the solution. On the right, the steady state is shown. An interesting consideration is that the maximum potential reached in the center of

the capacitor in not equal to V_0 but it is lower. Indeed, when the input signal has a high frequency (compared to the characteristic time of the circuit, τ) the points near the center of the capacitor have no time to reach the same voltage as the input.

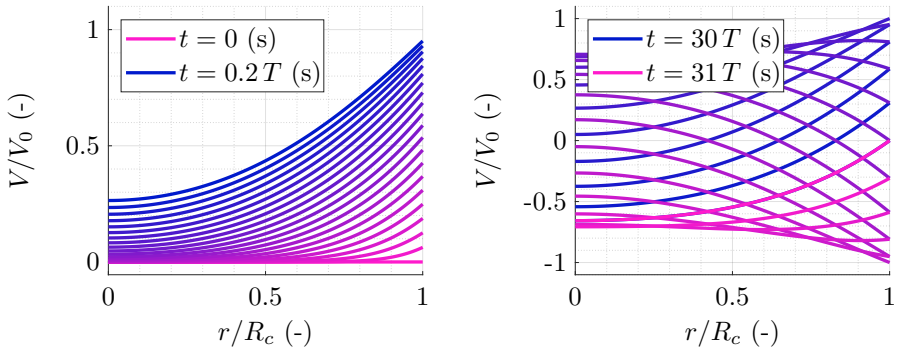

Figure 6.2: Analytical solution of the voltage profile in a circular capacitor. The excitation frequency is set to 0.125 MHz.

Experimental setup

The experimental setup comprehends the following materials:

- A copper ring, used to apply the external voltage on the boundary of the capacitor.
- A silicon film, used as the dielectric material of the capacitor.
- A carbon-black film, called elastomeric electrode, that constitutes the upper armor of the capacitor, which is attached to the silicon dielectric.
- An aluminum plate, that constitutes the lower armor, and has been grounded.

With these materials a circular elastomeric electrode was build, with a technique shown in Figure 6.3. Dielectric elastomeric transducers (DETs) are soft/deformable elastomeric capacitors composed of one or more layers of a dielectric elastomeric (DE), film coated by a conductive electrode.

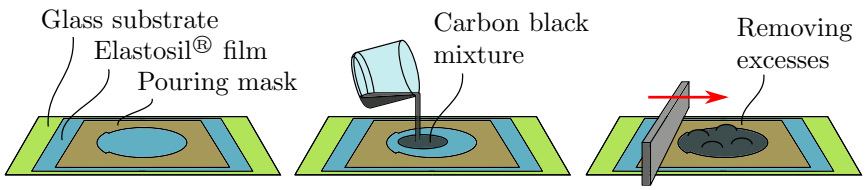

(a) Preparation (b) Pouring (c) Blading

Figure 6.3: The three phases of the preparation of the elastomeric electrode.

In this case, the DET under analysis was realized using a 100 µm thick film of Elastosil® 2030 as dielectric layer while a mixture of carbon black powder and PDMS Wacker silicone Silgel® RT625 as elastomeric electrode. In Figure 6.4 a schematic representation of the capacitor build for the experiment is depicted. NB: grounding the second armor means to analyze half of the capacitor described when introducing the analytical model and depicted in Figure 6.1.

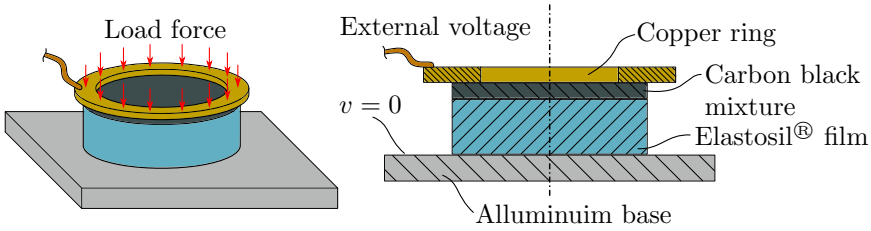

Figure 6.4: Scheme of the capacitor built for the experiment.

Before measuring the voltage profile on the capacitor surface with a 4-channel oscilloscope, the surface resistivity of the carbon black is estimated. Its value is computed by pressing two rectangular electrodes on the carbon black surface at a known distance and measuring the current generated by a given electric potential (Figure 6.5).

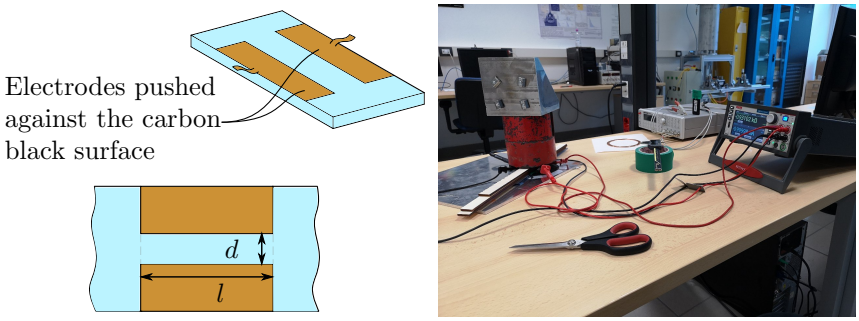

Figure 6.5: On the left, scheme of the electrodes used for the sheet resistance measurement. On the right, picture of the experimental setup to measure the surface resistivity of the carbon black.

Knowing the distance between electrodes (d) and their length (l), the surface resistivity of the carbon-black armor, R_s, is computed as $\frac{l}{d}R$.

Measure of the voltage profile

To take the voltage measurements, four probes were applied to the capacitor. The first probe was attached to the copper ring, and was used to measure the input signal, coming from a generator. The other three were attached to the upper armor

(carbon black) at different distance from the center of the capacitor, as shown in Table 6.1. Data were collected under different external voltage frequencies, listed in Table 6.2.

Table 6.1: Location of the probes where the voltage is measured across the capacitor radius.

Probe channel	Location
A	R_c
B	$2/3\,R_c$
C	$1/3\,R_c$
D	0
With R_c copper ring internal radius	

Table 6.2: values of the external voltage input frequencies with which the experiments were conducted.

Applied frequencies	Unit
67.5	
125	
250	kHz
500	
750	

Data analysis and comparison with analytical solution

In order to compare the analytical model with the collected data, the setup parameters are estimated. The values of the parameters are collected in Table 6.3. Since the experiment constitutes a preliminary study, the uncertainty associated to each measured parameter is neglected.

Table 6.3: Values of the capacitor model parameters estimated in order to compare the results with the analytical solution.

Param.	Value	Unit	Description
Physic param.			
ϵ_0	8.85×10^{-12}	$\mathrm{F\,m^{-1}}$	Vacuum permittivity
Known param.			
t_d	100×10^{-6}	m	Dielectric width
Measured param.			
R_s	11.75×10^{3}	$\Omega/\square$	Sheet resistance
C	2.15×10^{-9}	F	Capacitance
R_c	0.101/2	m	Copper ring radius
R	0.108/2	m	Membrane radius
Derived param.			
ϵ_r	$t_d\,C/(\pi R^2 \epsilon_0)$	(-)	Relative permit. coeff.
ϵ	$\epsilon_r \epsilon_0$	$\mathrm{F\,m^{-1}}$	Relative permit.
α	$t_d/(\epsilon R_s)$	$\mathrm{m^2\,s^{-1}}$	Parameter of Eq. 6.1

In order to plot the analytical solution, another parameter is needed, that is the voltage amplitude of the input (V_0). This quantity has been computed through a fitting procedure of the collected input signals in time domain. The discrete input signal s is, nominally, generated as a sinusoid with fixed angular frequency and amplitude by the instrumentation used. A parametric model of this signal is

$s_a = V_0 \sin(\omega t + \phi)$, where V_0, ω and ϕ are the parameters to be estimated. Taking the difference between s and s_a and computing the RMS (root mean square) one obtains the scalar function $F = F(V_0, \omega, \phi)$. Minimizing the function F starting from a reasonable initial guess, in the hypothesis that the actual signal s is in the form of $s_a + \delta$, with δ a *zero mean random noise*, should return a reliable estimate of the parameters V_0, ω and ϕ.
The analytical solution, build with the defined parameters, is plotted together with the experimental data in Figure 6.6. Each plot refers to one of the tested frequencies. In each plot, the experimental curve (orange) is computed averaging 32 data sets and is to be compared with the maximum envelope of the gray curves, which represents the analytical solution.

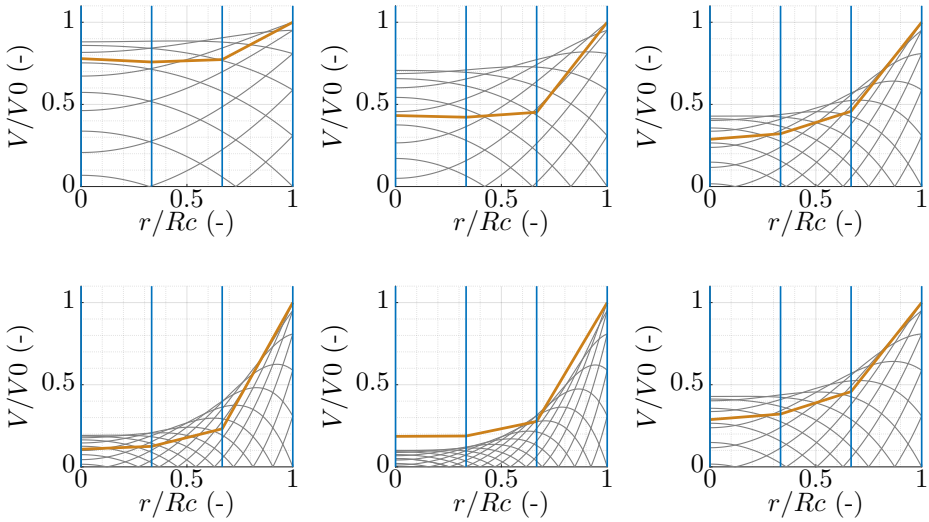

Figure 6.6: Comparison between the analytical solution in steady state (grey profile), and the mean experimental results (orange curves). The vertical line represents the location of the probes on the radius of the capacitor. The first five plots, from top to bottom and left to right, refers to 67.5 kHz, 125 kHz, 250 kHz, 500 kHz, 750 kHz external excitation frequency. Last plot shows a strange behaviour of the measured voltage that was observed during the experiment. The amplitude, sometimes collect around two or more distinct values when repeating the same test.

Discussion of experimental uncertainty and conclusions

A critical aspect of the experiment regards the estimation of the surface permittivity, from which the sheet resistance R_s is estimated. The problem is that the uncertainty on its value is high. This is due to how the quantity was estimated. Indeed, pressing the capacitor with a heavy load (approximately 6 kg) for a long time (approximately 12 hours) slightly deforms the surface of the capacitor and, furthermore, do not guarantee to have a prefect electric contact between the electrodes and the carbon black surface.

Another anomaly is visible in the last plot of Figure 6.6. At the frequency of 250 kHz, the signal amplitude is not the same for all of the 32 data tests. This is a strong evidence of the fact that the contact resistance between the probes and/or the copper ring and the carbon black capacitor surface is non negligible and time dependent.
Although one of the two groups of data produce a voltage profile which is close to the analytical model prediction, a bad electric contact, combined with the model uncertainty, can explain the non-perfect superposition of all the experimental curves to the analytical curves.
Another issue of the experiment is that the voltage amplitude measured at 500 kHz is lower than the one measured at 750 kHz, for all channels, which is unexpected. This is another hint of the bad electrical contact between the probes and the capacitor surface.
In conclusion, the experiment did not return completely satisfactory results. The fitting of the analytical model and the collected data is not perfect and strange behaviour is present in some data sets. Nevertheless, taking into account that this experiment was just a first trial, it has provided some useful information. Indeed, the presented results can be used to set up a more accurate experimental measurement. For example, it would be useful to find a more reliable method to compute the sheet resistance of the carbon black and to prepare the carbon-black surface with pre-inserted electrodes, such that a stable electric contact with low contact resistance can be achieved. Moreover, also the analytical model can be improved, taking into account the contact resistance, which is unavoidable. This last part is currently under investigation by the Author and PhD G. Moretti, under the coordination of Prof. M. Fontana.

6.3.2 Estimation of impacts on a free-falling body

In this Section it is described the state of the analysis of the impacts affecting the TMs of LPF after the release. In the in-flight tests of LPF, the very first impacts, which were the focus of this thesis, take place in a time frame of milli-seconds after the tip retraction. Those collisions gave the TM a velocity much larger than the maximum velocity set by the mission requirement ($5\,\mu m\,s^{-1}$ and $100\,\mu rad\,s^{-1}$). For this reason, in the seconds following the tip or the plunger retraction, the TM may undergo several impacts with the tips/plungers until those are retracted and the electrostatic force is activated. Such impacts, albeit being unexpected and undesired, are of scientific interest.
Indeed, the collisions taking place in this case are characterized by low relative velocities between two free-falling bodies (the TM, 2 kg, and the spacecraft, ≈500 kg). The Author is currently working on an article regarding this topic and in the following the main idea of the study will be highlighted.
The goal of the analysis is to detect impacts of the TM with the plungers in any of the releases, and observe their characteristics, such as the coefficient of restitution or the location of the collision point. Figure 6.7 shows the time intervals in which a generic release test can be subdivided, highlighting the interval of interest for this analysis. What makes the analysis complex is the low sampling frequency of the signals compared to the infinitesimal duration of the impacts. In the following,

the two main parts of the work, i.e., I) the detection of the release instant and II) the detection of constant velocity time intervals, are described. At the end, a brief discussion of the future steps is reported.

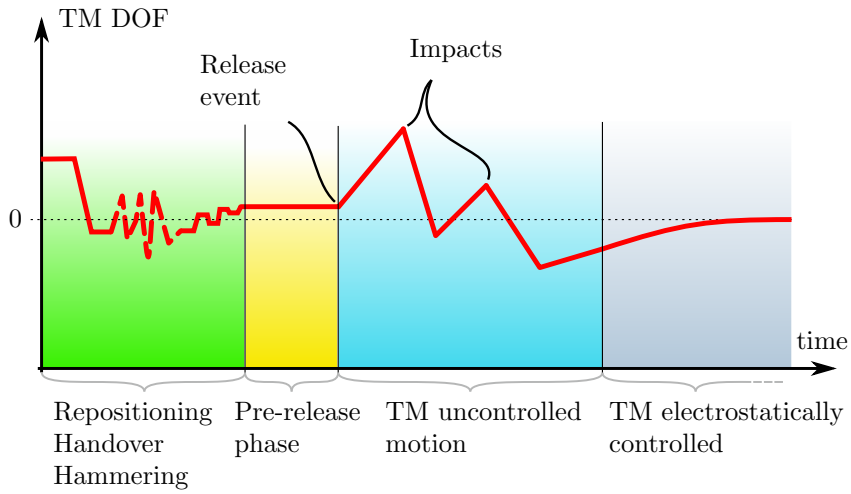

Figure 6.7: Phases of the injection procedure for a generic TM DOF. The green and yellow time intervals were the focus of the main research on the GPRM performance. The analysis presented in this section regards the time cyan interval, where the TM is free-falling in between impacts and the electrostatic force has not be activated.

Detecting the release instant

The formal analysis here presented is useful to determine when the TM starts moving, i.e., to find the first sample points after the actual release instant. For a given tests, a set of 20 pre-release sample points is used to characterize the pre-release noise. The proposed criterion defines the TM release when the measurement signal of at least one of its six DOFs violates the noise statistics. The hypotheses formulated on a generic time window are the following:

- H_0: $v = 0$ (no release)
- H_1: $v \neq 0$ (release)

Where v indicates the velocity of the TM for a generic DOF. The probability α of a type I error (H_0 rejected when true), is shown in Equation 6.2. The probability β of a type II error, i.e., missing the detection of a release, is shown in Equation 6.3.

$$\alpha = 2\left(1 - \frac{1}{2}\mathrm{erfc}\left(-\frac{\kappa}{\sqrt{2}}\right)\right)^n \tag{6.2}$$

Where $\kappa = s_{\max}/\sigma_s$, $s_{\max}$ is the maximum threshold (arbitrary), σ_s is the standard deviation of the signal noise and $\mathrm{erfc}(x)$ is the normal error function.

$$\beta(\gamma) = 1 - \prod_{i=1}^{n} \left(1 - \frac{1}{2}\text{erfc}\left(\frac{\nu(\gamma + i - 1) - \kappa}{\sqrt{2}}\right)\right) \tag{6.3}$$

Where γ identifies the time lead fraction of a sampling time of the actual release instant with respect to the sampled point $i = 1$, while $\nu = v\Delta t/\sigma_s$ is the release velocity v rescaled with respect to the reference velocity given by the ratio between the noise standard deviation σ_s and the sampling time Δt (which is equal to 0.1 s for the DOFs telemetry signals). In general, although γ is unknown, its probability density function is reasonably assumed uniform (the collision may take place in a generic time instant inside a sampling interval with equal probability). Thus, Equation 6.3 is integrated in γ, as shown in Equation 6.4.

$$\beta = \frac{1}{\gamma_{\max}} \int_0^{\gamma_{\max}} \beta(\gamma)\, d\gamma \tag{6.4}$$

where $\gamma_{\max} = 10$, since the time interval in which the release may take place is 10 sampling intervals long (the release instant is ruled from the tip command signal, which has a sampling frequency of 1 Hz).
In the case here presented, the detection of the release instant with $\kappa = 3$ and $n = 3$ along the z-axis telemetry signal (σ_s =0.02 µm) equal to the requirement (v =5 µm s^{-1}) is characterized by a probability β of a type II error of ≈1.2%.

Detecting constant velocity time intervals

After detecting the first sampling point in which the TM is in motion, named release instant, the challenge is to detect the intervals were the TM moves with constant velocity. Considering a set of n points of a signal s, and supposing they are sampled in a time interval in which the TM does not accelerate, their expression is the one shown in Equation 6.5.

$$s_i = t_i\, v + \delta_i = i\Delta t\, v + \delta_i \tag{6.5}$$

where v is the actual velocity of the TM, Δt the sampling time and δ_i the i-th realization of the post-release noise. Now, the question to answer is if, given the realization of the following sampling point (s_{n+1}), it can be included in the initial set of points, i.e., no impact occurred between points n and $n + 1$.
Similarly to what was done in for the detection of the release instant, the type I and type II error probabilities of considering the next point as part of the same set are evaluated and shown in Equations 6.6 and 6.7.

$$\alpha = \text{erfc}\left(\frac{\kappa}{\sqrt{2}\sqrt{\frac{(1+n)(2+n)}{(n-1)n}}}\right) \tag{6.6}$$

$$\beta(\gamma) = \frac{1}{2}\left(\text{erfc}\left(\frac{(\gamma-1)\Delta\nu - \kappa}{\sqrt{2}\sqrt{\frac{(n+1)(n+2)}{(n-1)n}}}\right) - \text{erfc}\left(\frac{(\gamma-1)\Delta\nu + \kappa}{\sqrt{2}\sqrt{\frac{(n+1)(n+2)}{(n-1)n}}}\right)\right) \tag{6.7}$$

Where κ is an arbitrary trees-hold with the same role played in Equation 6.2 and $\Delta\nu = \Delta v\Delta t/\sigma_s$ is the normalized velocity difference. Indeed, Δv is defined as the

difference of the TM velocity before and after a hypothetical impact taking place at $t = (n + \gamma)\Delta t$, with gamma $\in [0, 1)$.
Since the value of γ is not known a priori and in principle an impact can take place in any point in between two sample points with uniform probability, the average β probability is computed by integrating Equation 6.7 in $\gamma \in [0, 1)$. The closed form is not reported (due to its extension), but the mean probability β is plotted in Figure 6.8 for different values of n and κ.

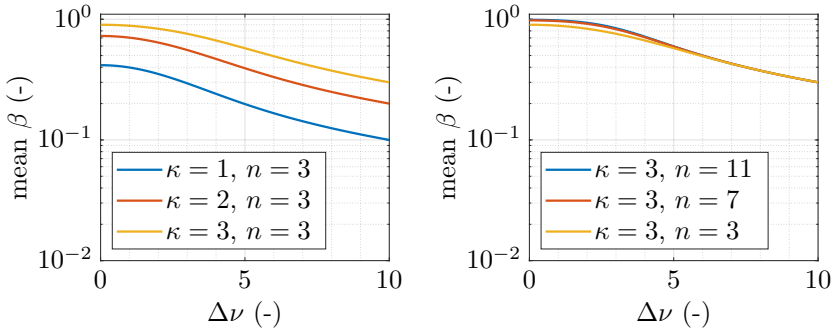

Figure 6.8: Mean β probability of impact detection as function of $\Delta\nu$, for different values of the parameters κ and n. The β probability is more dependent on κ rather than on n.

The computation of α and β probabilities of considering the point following a constant velocity interval as part of the interval or not are useful to statistically quantify the results of the search algorithm schematized in Figure 6.9.
The algorithm is designed to search for time intervals in which the TM velocity is constant with certain probabilities α and β in all the six DOFs simultaneously. An impact is detect if the vertical distance d between the fit line of a set of n points (with constant TM velocity) and the point immediately following the interval is greater than the quantity defined in Equation 6.8.

$$|d| > \epsilon(n, \alpha)\sigma_d = \epsilon(n, \alpha)\sigma_{\text{post}}\sqrt{\frac{(1+n)(2+n)}{(n-1)n}} \tag{6.8}$$

Where σ_{post} is the post-release noise std and the function $\epsilon(n, \alpha)$ is defined in Equation 6.9. This definition is useful because it permits to fix a desired value of α probability with which estimating the presence of an impact. Indeed, such a relation is found inverting Equation 6.6, expressing κ as a function of n and α.

$$\epsilon(n, \alpha) = \sqrt{2}\sqrt{\frac{(1+n)(2+n)}{(n-1)n}}\text{erfc}^{-1}(\alpha) \tag{6.9}$$

As mentioned, the checking procedure is carried out simultaneously for all the six DOFs. The presence of an impact is assumed if the condition expressed in

Equation 6.8 is not respected for at least one of the DOFs. The algorithm ends when the points to be checked are finished, i.e., when the last index (i_{end}) is reached. The index i_{end} is set close to the time instant when the plungers are retracted and/or the electrostatic actuation force is activated.

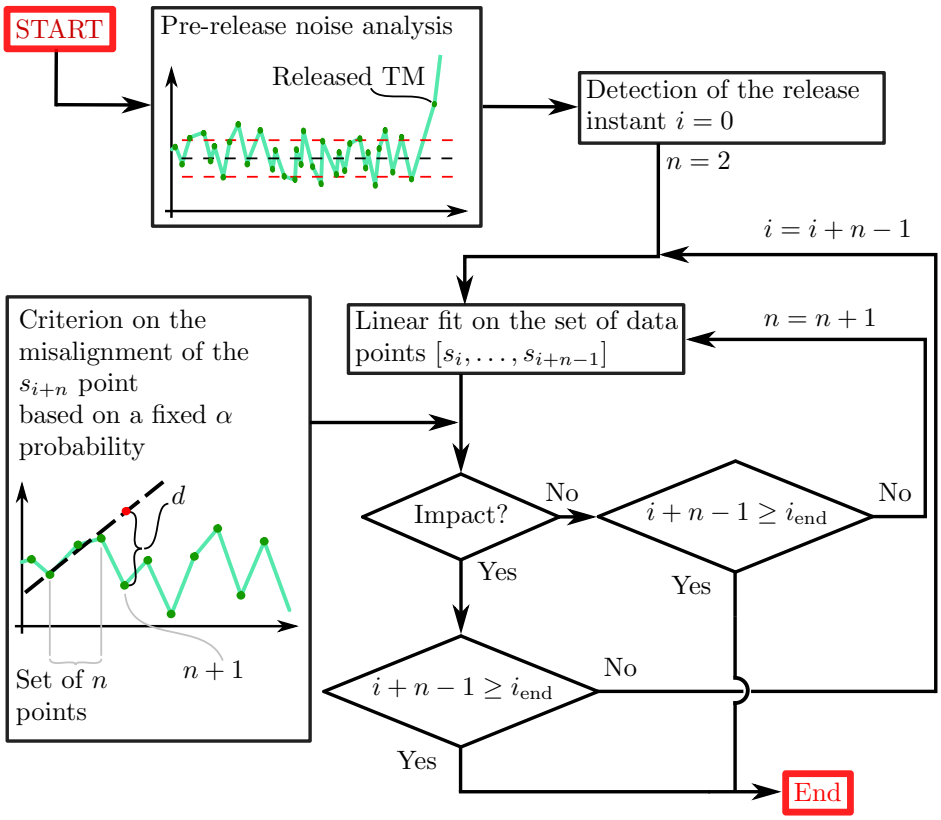

Figure 6.9: Flow-chart of the algorithm that searches for constant velocity time intervals in a generic DOF signal.

Discussion on next steps

The results of the application of the algorithm to the in-flight data of LPF are still under analysis. An example, from a TM_1 automated test, is shown in Figures 6.10a, 6.10b and 6.10c.
The future step is to compute the TM kinetic energy on any of the detected constant velocity intervals in a tests. For example, in the j-th interval, the TM kinetic energy K_j is estimated by fitting a linear model to the DOFs telemetry data. In any test where two or more constant velocity intervals are detected, the j-th impact (or set of impacts) restitution coefficient e_j is computed as shown in Equation 6.10.

$$e_j = \sqrt{\frac{K_j}{K_{j-1}}} \tag{6.10}$$

The results may be filtered considering only a couple of consecutive intervals that are close to each other and focusing on impacts producing significant variation of the kinetic energy ($\gg$ than the propagated uncertainty of the fit lines).
For example, in this way it is possible to determine if an impact taking place during the slow tip retraction is energetic (i.e., the TM kinetic energy increases) or if an impact taking place when no actuator is activated dissipates energy.
Moreover, given the state of the TM after the release, it may be possible to estimate the expected number of impacts (and seconds) which are sufficient to damp the TM kinetic energy to a level below which it is controllable by the electrostatic control force. The last point is of particular interest in view of the LISA mission, where no real time human control will be possible during the injection procedure of the six TMs.

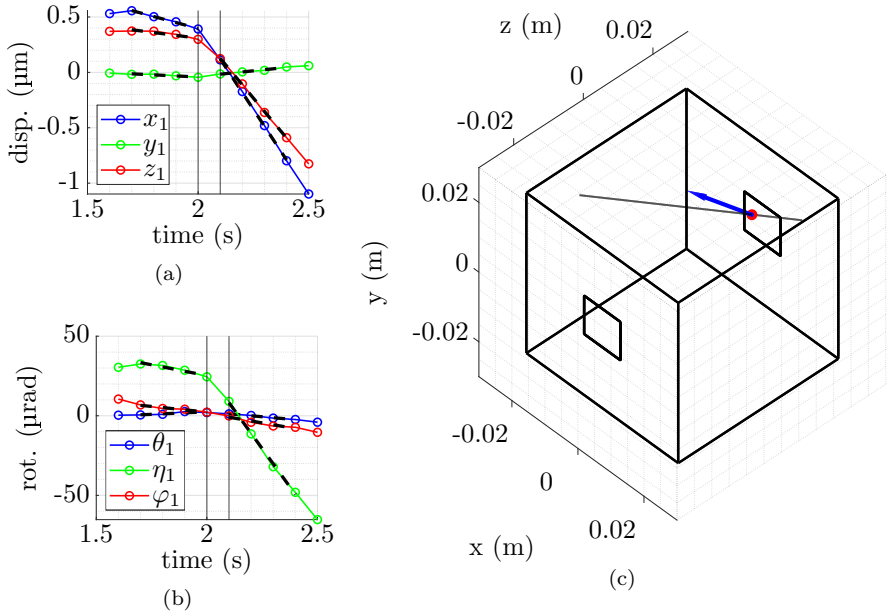

Figure 6.10: On the left, linear (top) and angular (bottom) degrees of freedom of a TM_1 automated test, plotted in a time interval approximately 2 second after the tip release (when the plungers retraction starts). An impact, probably caused by the motion of the plungers, took place in between the vertical black lines. On the right, sketch of the TM geometry showing the estimated location of the impulse generated by the same impact. The point is found intersecting the TM geometry with the line where the impulse lies. The blue arrow indicate the velocity of the collision point after the impact, showing that it is almost orthogonal to the indent surface.

6.3.3 Modeling the charge management system of LPF and LISA gravitational reference sensor

During the PhD studies, the Author started a collaboration with the Physics Department of the University of Trento (contact person Dr. V. Ferroni). Such a collaboration is aimed at developing an advanced FEM model of the GRS charge management system (CMS).
When the spacecraft is orbiting in outer space, the TMs are inevitably impacted by high energetic particles (i.e., galactic cosmic rays and solar energetic particles) and accumulate charge over time as they are electrically isolated from the rest of the SC. In fact, the spacecraft chassis and other LTP components are capable of shielding the TM only from particles with an energy below 100 MeV.
Having a non-zero charged TM negatively affects the noise measurement of LPF and the gravitational measurement of LISA, since Coulomb and Lorentz forces arise on the TM due to surrounding stray fields ([30] and [31]).
For this reason, a proper CMS is needed to maintain the TM charge close to 0 C. Since the TM, during the science phase, is not in contact with any components of the LTP, the charge control is achieved thanks to ultra violet (UV) led lamps. When a lamp is turned on, the UV light photons hit the GRS inner surfaces producing a flow of electrons thanks to the photoelectric effect. The UV lamps, located on the vertices of the EH chassis on the $-$z side, are pointed either on the TM or on the EH walls/electrodes, to produce respectively a net positive or negative charge rate on the TM.
There are several variables involved in the CMS of LISA Pathfinder (and LISA also). In general, the charge/discharge current is heavily affected by the electric fields generated by the TM charge and the sensing and actuation systems. Moreover, the quantum yield of the surfaces, the timings of light on/off cycles, the cone angle of the UV lamps, the leds power play an important role. For this reasons, combined with the fact that the geometry of the GRS is complex, a FEM model is required to properly characterize the CMS performance ([32]).

The 3D model of the GRS

The modeling of the CMS starts from the FM geometry of the GRS. The CAD model is initially cleared from harnesses and components which do not play a role in the charging or discharging of the TM. The EH chassis geometry is thoroughly simplified, removing screws, filling screw holes and deleting unnecessary geometrical details. The electrodes are re-drawn without the holes used to screw them to the EH chassis. The plungers and the CVM fingers are simplified removing the backend and keeping only the heads (i.e., the parts close to the TM). The TM geometry is kept in its original form.
The simplified components are then imported into a COMSOL model, where two physic nodes are present:

- Electrostatic: to compute the electric fields present in the GRS, given a certain charge on the TM and a certain configuration of the sensing and actuation voltages.

- Charged particle tracing: to trace a flow of electrons that are emitted from specific spots on the GRS surfaces.

The simulation is performed in two steps under the assumption that the electric fields inside the GRS are constant while the electrons flow. Indeed, considering that the minimum voltage period is 1×10^4 ns (corresponding to the injection frequency of 1×10^5 Hz) and the time needed for electrons to flow is lower than 1×10^2 ns, the assumption is reasonable.
The first step is the evaluation of the electric fields in a specific time instant. The electric fields inside the GRS depend on the values of the actuation/sensing voltages and the TM charge. Moreover, also the plunger position, the fingers position and TM position and attitude affect the electric fields. In Figure 6.11 the electric field is shown in the case of zero voltages applied to the electrodes, positive 1 V on the TM, retracted fingers and plungers close to the TM. The simulations, so far, are executed under the hypothesis that the GRS is in science mode, i.e., that the TM is centered in the EH and the GPRM end effectors are retracted. In any case, the model could be used to analyze also different scenarios, since the mentioned quantities are all parametrized.

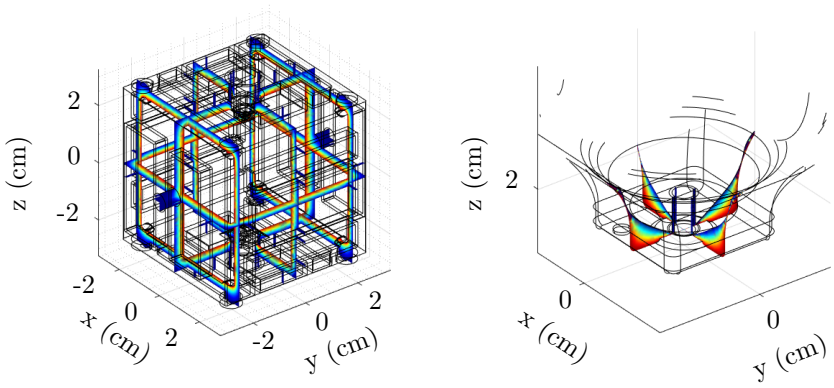

Figure 6.11: Electric field in the GRS (in the space between the TM and the surroundings) in the case on zero actuation and injection voltages and EH chassis (blue color) and a positive voltage applied to the TM (red color). The eight fingers of the CVM are retracted, while the two plungers are close to the TM (detail on the right plot).

Once the electric field is evaluated, the second step is to trace electrons, i.e., compute their trajectory. In Figure 6.12, the trajectories of the electrons emitted by the so called gap surfaces of the GRS, comprehending all the recesses between electrodes and guard-rings, the holes hosting the GPRM end-effectors, the holes inside which the lamps are mounted, are shown. Similar plots are obtained considering releasing electrons from other surfaces of the GRS (the one facing the TM) or from the TM surfaces, including the vertices and the indents of the ±z faces.

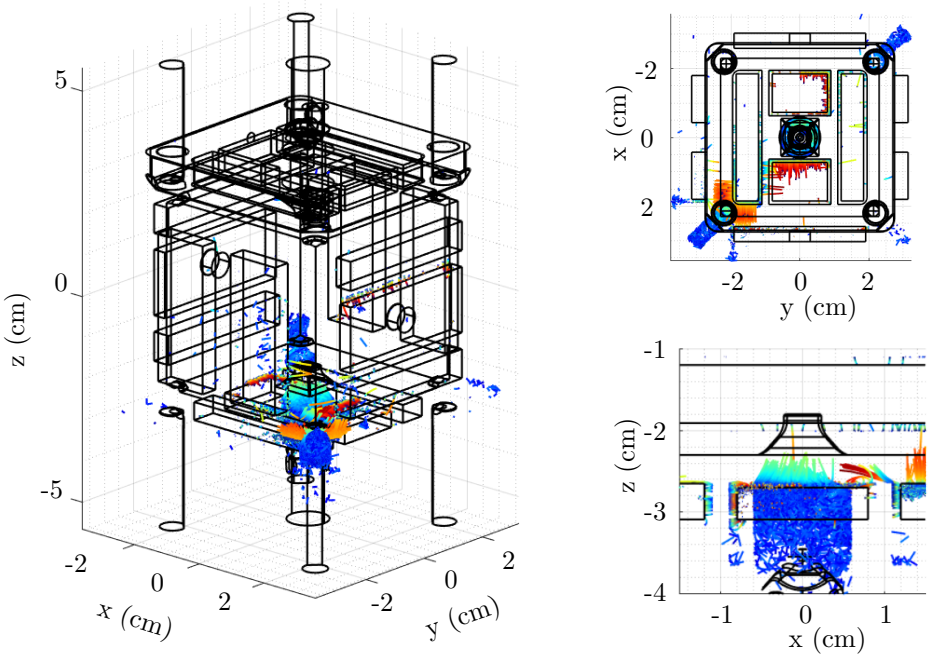

Figure 6.12: Trajectories of the electrons coming from the gaps present in the EH for one of the simulations. The plot on the left shows the complete GRS geometry with the vast majority of the emitted electrons on the bottom ($-z$ side), where the UV lamps are targeted. The colors of the trajectories represent the absolute velocity of the particles (blue means slow, red means fast).

The location from which electrons were released are defined exploiting the result of a GEANT4 simulation. The simulation propagates the photons injected by the UV lamp inside the GRS and calculates their absorption points. Simulating a large enough number of photons trajectories, the results of the simulation are assumed statistically significant for any UV power, thus the coordinates of the absorption points are fed as electron release points to COMSOL.
The tracing of the electrons allows to compute the apparent yield (AY) curves of the GRS, defined as the ratio between electrons reaching the TM and injected photons versus the electric potential of the TM, for a given configuration of the GRS and of the illumination. The apparent yield curves enclose all the discharge properties of the TM and are fundamental to build the control scheme of the TM discharge during the mission.
For example they are used to compute the time needed to bring the TM charge to equilibrium, starting from a certain initial condition, given the power of the UV lamp and can be compared with the experimental curves measured at the Department of Physics of the University of Trento (see Figure 6.13). Such a comparison is fundamental to validate the model results.

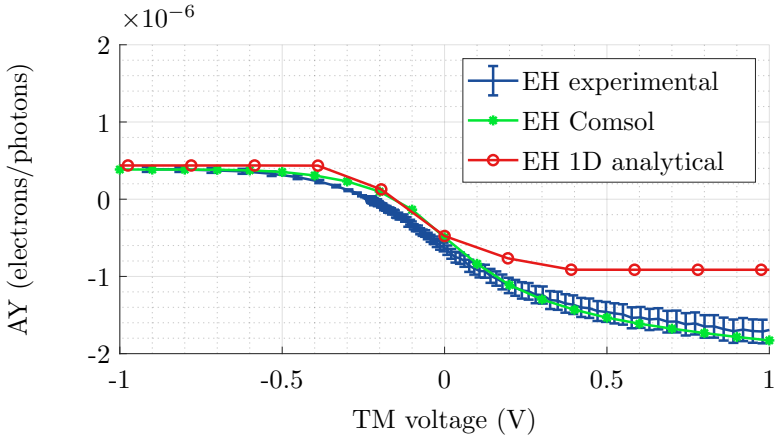

(a)

Figure 6.13: Apparent yield curves of the GRS for EH surfaces illumination. The curves computed from the COMSOL model results are compared with the experimental curves estimated with on-ground testing and with the AY predicted by a simplified 1D analytical model of the GRS. The analytical model fails to correctly predict the AY at the higher voltages.

By looking at the AY curves, the TM charge rate $\dot{Q}_{\mathrm{TM}}$, in the neighborhood of the equilibrium point (i.e., when the apparent yield is equal to zero), can be approximated fitting a negative slope line as a function of the TM charge Q_{TM} (or the TM voltage V_{TM}, since it is equal to Q_{TM}/C_0). Thus, the differential equation governing the TM charge dynamics is the one reported in Equation 6.11.

$$\dot{Q}_{\mathrm{TM}}(t) = |e^-|Pk(V_{\mathrm{eq}} - \frac{Q_{\mathrm{TM}}(t)}{C_0}) \tag{6.11}$$

Where the parameter k represents the module of the slope of the fitting line, e^- is the charge of the electron, P indicates the power of the lamp, V_{eq} is the equilibrium potential and C_0 the capacitance of the TM with respect to the all the GRS surfaces when the plungers are retracted and the mass is centered. The equation can be solved for the TM charge Q_{TM}, given a certain initial condition $Q_{\mathrm{TM},0} = V_{\mathrm{TM},0}C_0$. The AY curves are independent of the illuminating power and this means that the speed of the charging/discharging can be regulated adjusting the number of emitted photons per second.
Typical values of the model parameters in the case of EH illumination at low power are listed in Table 6.4. The solutions of the model in this case, for two different initial TM voltages ($-0.1\,\mathrm{V}$ and $0.2\,\mathrm{V}$), are plotted in Figure 6.14a. As can be observed, in this case, the time needed to reach equilibrium is approximately $1 \times 10^5\,\mathrm{s}$.
In Figure 6.14a, it is shown the effect of the illuminating power P on the time needed to reach the equilibrium potential. Increasing P allows to reach the equilibrium faster, with the drawback of generating a non-negligible noise in the TM position readings that affects the science measurement.

Table 6.4: Typical values of the parameters of the CMS model described in Equation 6.11.

Param.	Value	Unit	Description
e^-	-1.6×10^{-19}	C	Charge of the electron particle
P	1×10^9	photons/s	Typical value of the UV lamp power for slow TM discharge (1 photons/s $\approx 8 \times 10^{-19}$ W)
k	1.4×10^{-5}	electrons/photons/V	Slope of the linear fit of the AY curve near the equilibrium voltage
V_{eq}	-0.071	V	Equilibrium voltage on the AY curve
C_0	35×10^{-12}	F	Capacitance of the TM with the surroundings in science phase

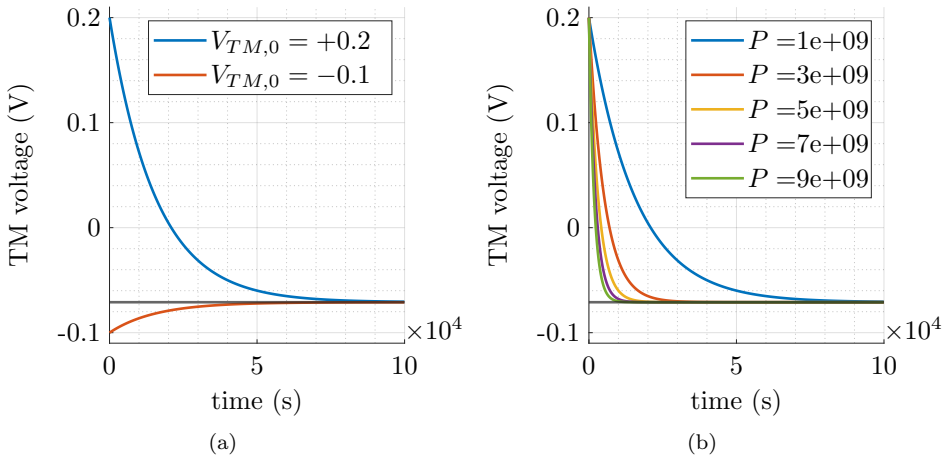

Figure 6.14: On the left, solution of Equation 6.11 for two different initial condition on the TM voltage, in the case of EH illumination with no actuation or injection voltages. On the right, effect of the variation of the illuminating power P (expressed in photons/s) on the time needed to reach the equilibrium under the same GRS configuration.

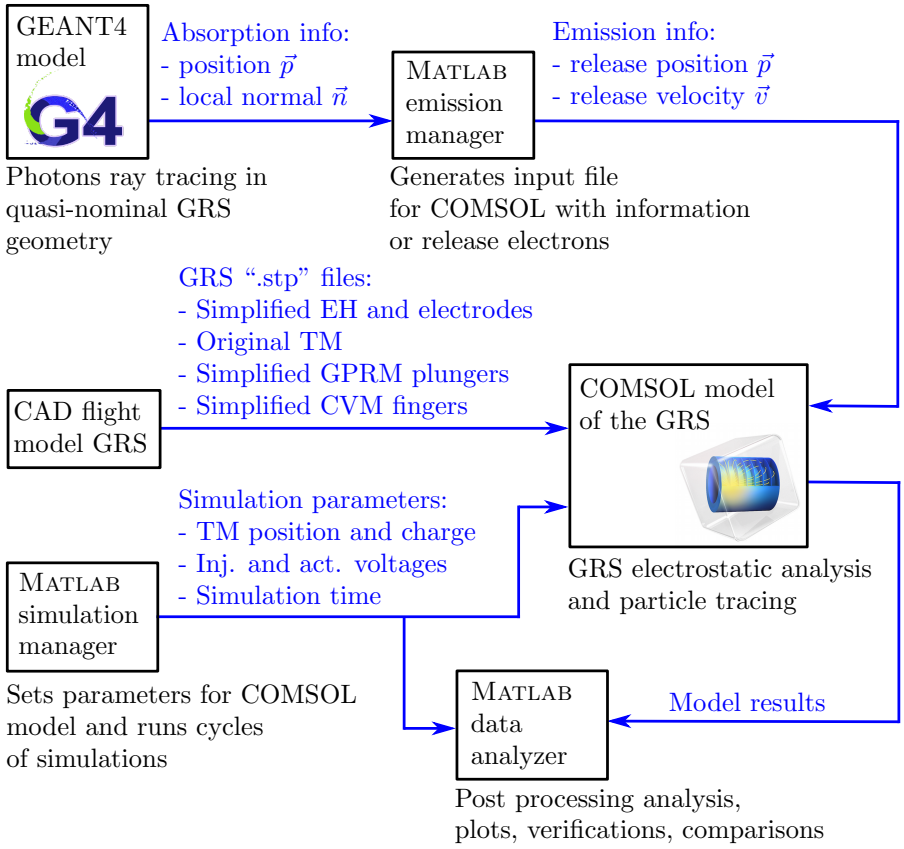

Figure 6.15: Scheme of the different files (black rectangles) used to model the CMS of the GRS. The blue arrows link different files, carrying the information highlighted in blue.

Appendices

Appendix A

Simultaneous fitting of vibration signals

The function f_j used to fit the $\bar{x}_j$ signal consists in a sum of two damped vibration modes. In particular, the first mode describes the energy concentrated around the frequency peaks at 2 kHz, while the second mode the frequency peak at 17 kHz. The analytical expression of f_j is reported in Equation A.1, where t is the time (s), $A_{i,j}$ represents the mode amplitude (µm), $\phi_{i,j}$ represents the mode phase (rad), d_i represents the damping parameter (1/s) and f_i represents the frequency (Hz). The subscript i refers to the modes ($i \in \{1, 2\}$), while the subscript j refers to the position on the plunger lateral surface at which the laser was pointed ($j \in \{1, 2, \ldots, 6\}$). In the model, given the superposition principle, the frequency and damping parameters of each mode do not depend on the test nor on the position at which the laser was pointed. Conversely, the phase of each mode depends on the duration of the excitation, which is produced by the retraction of the release tip. Assuming that the time duration of the retraction is characterized by some randomness, the phase of the mean signals measured at different locations might be different because they were observed in different realizations of the experiment. As a consequence, each mean signal is fitted with a different phase parameter. The variable β in the model represents the vector containing all the parameters, that are briefly summarized in Table A.1. It is worth noting that the function $f_j(t, \beta)$ depends only on a subset of the parameters, i.e., that strictly related to the j-th laser position, defined as β_j. The modal expansion expressed by Equation A.1 neglects modes with frequencies larger than 17 kHz. Even though the inclusion of more modes would increase the theoretical accuracy of the model, oscillations with larger frequencies would also be characterized by smaller amplitudes and a limited contribution to the impact dynamics.

$$f_j(t, \beta) = \sum_{i=1}^{2} A_{i,j} \cdot e^{-d_i t} \cdot \sin(2\pi f_i t + \phi_{i,j}) \tag{A.1}$$

The fitting procedure is based on the weighted least squares method ([33]), here applied simultaneously to the six lateral displacement mean signals. The target function $\chi(\beta)$ quantifies the closeness between the mean signals and their paramet-

Table A.1: Parameters describing the model used for the fitting.

Param.	Unit	Description
$A_{i,j}$	µm	Amplitude of the i-th mode ($i \in \{1,2\}$) in the j-th signal ($j \in \{1,2,\ldots,6\}$)
$\phi_{i,j}$	rad	Phase of the i-th mode ($i \in \{1,2\}$) in the j-th signal ($j \in \{1,2,\ldots,6\}$)
f_i	Hz	Frequency of the i-th mode ($i \in \{1,2\}$)
d_i	1/s	Damping of the i-th mode ($i \in \{1,2\}$)

ric model and is defined in Equation A.2, where the variable t_k represents the k-th sampling instant and N is the total number of sampling points composing the j-th signal. The numerator of the function corresponds to the difference between the mean signal $\bar{x}_j$ evaluated at the k-th time instant and the value provided by the model $f_j(t_k, \beta)$ at the same time instant. The denominator represents the standard deviation σ_j of the j-th signal, computed at t_k.

$$\chi(\beta) = \sum_{j=1}^{6} \sum_{k=1}^{N} \left(\frac{x_j(t_k) - f_j(t_k, \beta)}{\sigma_j(t_k)} \right)^2 \tag{A.2}$$

The initial guess for the amplitudes, phases and damping parameters are deduced by observing the signals in the time domain (Figure 4.7a), while for the frequencies they are estimated by extracting the peaks in the PSD plot (Figure 4.7b). Since the target function has several minima, the fitting is performed varying the initial guess 300 times (in the range ±25%), in order to increase the probability of finding the global minimum.

Appendix B

Planar collision model

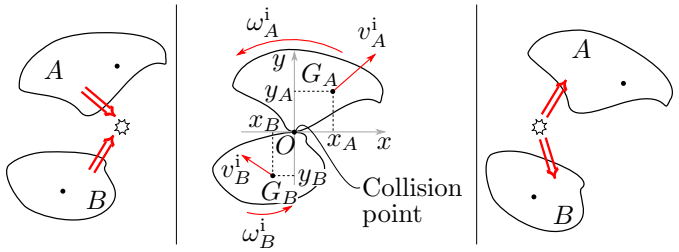

Figure B.1: Graphical representation of two colliding rigid bodies. In the center, the instant immediately before the collision is depicted and the instantaneous velocities of the bodies are shown.

The solution of the planar collision model described in Section 4.3.2 is reported in the System of Equations B.1 and the physical quantities mentioned are described in Table B.1. The actual Equations that lead to the presented solution described in [28]. The subscripts A and B identify the two colliding bodies. The superscripts i and f identify the instants before and after the impact respectively.

$$
\begin{cases}
I_T & = 0 \\
I_N & = \frac{2m_A m_B I_{A,g} I_{B,g}\left(-v^i_{A,y}+v^i_{B,y}+x_A\omega^i_A-x_B\omega^i_B\right)}{m_A x_A^2 m_B I_{B,g}+m_A m_B x_B^2 I_{A,g}+(m_A+m_B) I_{A,g} I_{B,g}} \\
V^i_N & = v^i_{A,y} - v^i_{B,y} - x_A\omega^i_A + x_B\omega^i_B \\
V^f_N & = V^i_N \\
v^f_{A,x} & = v^i_{A,x} \\
v^f_{A,y} & = \frac{I_{A,g}\left(-m_B I_{B,g}\left(v^i_{A,y}-2\left(v^i_{B,y}+x_A\omega^i_A-x_B\omega^i_B\right)\right)+m_A I_{B,g} v^i_{A,y}+m_A m_B x_B^2 v^i_{A,y}\right)+m_A x_A^2 m_B I_{B,g} v^i_{A,y}}{m_A x_A^2 m_B I_{B,g}+m_A m_B x_B^2 I_{A,g}+(m_A+m_B) I_{A,g} I_{B,g}} \\
\omega^f_A & = \frac{I_{B,g}\left(m_B\omega^i_A I_{A,g}+m_A x_A m_B\left(2v^i_{A,y}-2v^i_{B,y}-x_A\omega^i_A+2x_B\omega^i_B\right)+m_A\omega^i_A I_{A,g}\right)+m_A m_B x_B^2\omega^i_A I_{A,g}}{m_A x_A^2 m_B I_{B,g}+m_A m_B x_B^2 I_{A,g}+(m_A+m_B) I_{A,g} I_{B,g}} \\
v^f_{B,x} & = v^i_{B,x} \\
v^f_{B,y} & = \frac{I_{A,g}\left(m_A I_{B,g}\left(2v^i_{A,y}-v^i_{B,y}-2x_A\omega^i_A+2x_B\omega^i_B\right)+m_A m_B x_B^2 v^i_{B,y}+m_B I_{B,g} v^i_{B,y}\right)+m_A x_A^2 m_B I_{B,g} v^i_{B,y}}{m_A x_A^2 m_B I_{B,g}+m_A m_B x_B^2 I_{A,g}+(m_A+m_B) I_{A,g} I_{B,g}} \\
\omega^f_B & = \frac{I_{A,g}\left(m_A\omega^i_B I_{B,g}+m_A m_B x_B\left(-2v^i_{A,y}+2v^i_{B,y}+2x_A\omega^i_A-x_B\omega^i_B\right)+m_B\omega^i_B I_{B,g}\right)+m_A x_A^2 m_B\omega^i_B I_{B,g}}{m_A x_A^2 m_B I_{B,g}+m_A m_B x_B^2 I_{A,g}+(m_A+m_B) I_{A,g} I_{B,g}}
\end{cases}
\tag{B.1}
$$

Table B.1: Parameters appearing in the collision model. Subscript k refers to the bodies A or B.

Param.	Unit	Description
$I_{k,g}$	$\mathrm{kg\,m^2}$	Body moment of inertia computed with respect to its center of mass
m_k	kg	Mass of the body
I_T	N s	Impulse tangential to the colliding surfaces
I_N	N s	Impulse normal to the colliding surfaces
x_k, y_k	m	Coordinates of the body center of mass in the collision reference frame
V_N	$\mathrm{m\,s^{-1}}$	Normal relative velocity
$v_{k,x}, v_{k,y}$	$\mathrm{m\,s^{-1}}$	Linear velocity components of the body
ω_k	$\mathrm{rad\,s^{-1}}$	Angular velocity of the body

Bibliography

[1] LIGO laser interferometer gravitational-waves observatory. `https://www.ligo.caltech.edu/page/vibration-isolation`. Accessed: 2021-07-24.

[2] J. M. Weisberg, J. H. Taylor, and L. A. Fowler. Gravitational waves from an orbiting pulsar. *Scientific American*, 245(4):74–83, 1981.

[3] R. S. Shankland. Michelson and his interferometer. *Physics Today*, 27(4):36–43, 1974.

[4] M. Pitkin, S. Reid, S. Rowan, and J. Hough. Gravitational wave detection by interferometry (ground and space). *Living Reviews in Relativity*, 14(1):5, 2011.

[5] D. V. Martynov, E. D. Hall, B. P. Abbott, R. Abbott, et al. Sensitivity of the advanced LIGO detectors at the beginning of gravitational wave astronomy. *Physical Review D*, 93(11):112004, 2016.

[6] R. N. Manchester. The international pulsar timing array. *Classical and Quantum Gravity*, 30(22):224010, 2013.

[7] LISA space mission. `https://sci.esa.int/web/lisa`. Accessed: 2021-07-22.

[8] M. Armano, M. Benedetti, J. Bogenstahl, D. Bortoluzzi, P. Bosetti, et al. LISA Pathfinder: the experiment and the route to LISA. *Classical and Quantum Gravity*, 26(9):094001, 2009.

[9] G. Wanner. Space-based gravitational wave detection and how LISA Pathfinder successfully paved the way. *Nature Physics*, 15(3):200–202, 2019.

[10] D. Bortoluzzi, B. Foulon, C. G. Marirrodriga, and D. Lamarre. Object injection in geodesic conditions: in-flight and on-ground testing issues. *Advances in Space Research*, 45(11):1358–1379, 2010.

[11] R. F. Tylecote. The solid phase bonding of gold to metals. *Gold Bulletin*, 11(3):74–80, 1978.

[12] N. Gane, P. F. Pfaelzer, and D. Tabor. Adhesion between clean surfaces at light loads. *Proceedings of the Royal Society of London. Series A, Mathematical and Physical Sciences*, 340(1623):495–517, 1974.

[13] C. Zanoni and D. Bortoluzzi. Experimental-analytical qualification of a piezoelectric mechanism for a critical space application. *IEEE/ASME Transactions on Mechatronics*, 20(1):427–437, 2014.

[14] D. Bortoluzzi, D. Vignotto, A. Zambotti, et al. In-flight testing of the injection of the LISA Pathfinder test mass into a geodesic. *Advances in Space Research*, 67(1):504–520, 2021 (Copyr. Elsevier).

[15] B. Zahnd, M. Zimmermann, and R. Spörri. LISA-Pathfinder cage and vent mechanism development and qualification. *15th ESMATS proc., Noordwijk*, 2013.

[16] D. Bortoluzzi, J. W. Conklin, and C. Zanoni. Prediction of the LISA-Pathfinder release mechanism in-flight performance. *Advances in Space Research*, 51(7):1145–1156, 2013.

[17] D. Bortoluzzi, P. A. Mäusli, R. Antonello, and P. M. Nellen. Modeling and identification of an electro-mechanical system: the LISA grabbing positioning and release mechanism case. *Advances in Space Research*, 47(3):453–465, 2011.

[18] D. Bortoluzzi, M. Armano, H. Audley, G. Auger, J. Baird, P. Binetruy, M. Born, et al. Injection of a body into a geodesic: lessons learnt from the LISA Pathfinder case. *43rd AMS proc., NASA Ames Research Center*, 2016.

[19] I. Köker, H. Rozemeijer, F. Stary, and K. Reichenberger. Alignment and testing of the GPRM as part of the LTP caging mechanism. *15th ESMATS proc., Noordwijk*, 2013.

[20] M. Armano, H. Audley, J. Baird, P. Binetruy, M. Born, D. Bortoluzzi, E. Castelli, A. Cavalleri, A. Cesarini, et al. Precision charge control for isolated free-falling test masses: LISA Pathfinder results. *Physical Review D*, 98(6):062001, 2018.

[21] C. Zanoni and D. Bortoluzzi. Estimation of the electrostatic effects in the LISA-Pathfinder critical test mass dynamics via the method of moments. *IEEE/ASME Transactions on Mechatronics*, 2021.

[22] M. Armano, H. Audley, G. Auger, J. Baird, P. Binetruy, M. Born, D. Bortoluzzi, N. Brandt, A. Bursi, et al. A strategy to characterize the LISA-Pathfinder cold gas thruster system. In *Journal of Physics: Conference Series*, volume 610, page 012026. IOP Publishing, 2015.

[23] M. Armano, H. Audley, J. Baird, P. Binetruy, M. Born, D. Bortoluzzi, E. Castelli, et al. Temperature stability in the sub-millihertz band with LISA Pathfinder. *Monthly Notices of the Royal Astronomical Society*, 486(3):3368–3379, 2019.

[24] D. Bortoluzzi, M. Benedetti, L. Baglivo, M. De Cecco, and S. Vitale. Measurement of momentum transfer due to adhesive forces: on-ground testing of in-space body injection into geodesic motion. *Review of Scientific Instruments*, 82(12):125107, 2011.

[25] H. J. M. T. A. Adriaens, W. L. De Koning, and R. Banning. Modeling piezoelectric actuators. *IEEE/ASME Transactions on Mechatronics*, 5(4):331–341, 2000.

[26] IEEE standard on piezoelectricity. *ANSI/IEEE Std*, pages 176–1987, 1988.

[27] S. Wolfram. *The Mathematica Book, Wolfram Research Inc.* Cambridge Univ. Press, Cambridge, 2003.

[28] A. G. Zabuga. Modeling the collision with friction of rigid bodies. *International Applied Mechanics*, 52(5):557–562, 2016.

[29] D. Bortoluzzi, D. Vignotto, E. Dalla Ricca, and J. Mendes. Investigation of the in-flight anomalies of the LISA Pathfinder test mass release mechanism. *Advances in Space Research*, 68(6):2600–2615, 2021 (Copyr. Elsevier).

[30] T. J. Sumner, G. Mueller, J. W. Conklin, P. J. Wass, and D. Hollington. Charge induced acceleration noise in the LISA gravitational reference sensor. *Classical and Quantum Gravity*, 37(4):045010, 2020.

[31] H. M. Araújo, P. J. Wass, D. Shaul, G. Rochester, and T. J. Sumner. Detailed calculation of test-mass charging in the LISA mission. *Astroparticle Physics*, 22(5):451–469, 2005.

[32] T. Ziegler, P. Bergner, G. Hechenblaikner, N. Brandt, and W. Fichter. Modeling and performance of contact-free discharge systems for space inertial sensors. *IEEE Transactions on Aerospace and Electronic Systems*, 50(2):1493–1510, 2014.

[33] T. Strutz. *Data fitting and uncertainty.* Springer, 2010.

[34] J. B. Hartle. Gravity: An introduction to Einstein's general relativity, 2003.

[35] A. Einstein. Die grundlage der allgemeinen relativitätstheorie. In *Das Relativitätsprinzip*, pages 81–124. Springer, 1923.

[36] B. P. Abbott, R. Abbott, T. D. Abbott, et al. Observation of gravitational waves from a binary black hole merger. *Physical Review Letters*, 116(6):061102, 2016.

[37] M. Armano, H. Audley, G. Auger, J. Baird, M. Bassan, P. Binetruy, M. Born, et al. Sub-femto-g free fall for space-based gravitational wave observatories: LISA Pathfinder results. *Physical Review Letters*, 116(23):231101, 2016.

[38] M. Armano, H. Audley, J. Baird, P. Binetruy, M. Born, D. Bortoluzzi, et al. Beyond the required LISA free-fall performance: new LISA Pathfinder results down to 20μHz. *Physical review letters*, 120(6):061101, 2018.

[39] S. Anza, M. Armano, E. Balaguer, M. Benedetti, C. Boatella, P. Bosetti, D. Bortoluzzi, N. Brandt, et al. The LTP experiment on the LISA Pathfinder mission. *Classical and Quantum Gravity*, 22(10):S125, 2005.

[40] A. Neukom, R. Romano, and P. M. Nellen. Testing and lessons learnt of LISA GPRM. *13rd ESMATS proc., Vienna*, 2009.

[41] D. Bortoluzzi, L. Carbone, A. Cavalleri, M. Da Lio, R. Dolesi, C. D. Hoyle, M. Hueller, S. Vitale, and W. J. Weber. Measuring random force noise for LISA aboard the LISA Pathfinder mission. *Classical and Quantum Gravity*, 21(5):S573, 2004.

[42] M. Armano, H. Audley, G. Auger, J. Baird, M. Bassan, P. Binetruy, M. Born, D. Bortoluzzi, N. Brandt, et al. Capacitive sensing of test mass motion with nanometer precision over millimeter-wide sensing gaps for space-borne gravitational reference sensors. *Physical Review D*, 96(6):062004, 2017.

[43] R. Dolesi, D. Bortoluzzi, P. Bosetti, L. Carbone, A. Cavalleri, I. Cristofolini, M. Da Lio, G. Fontana, V. Fontanari, et al. Gravitational sensor for LISA and its technology demonstration mission. *Classical and Quantum Gravity*, 20(10):S99, 2003.

[44] C. Zanoni, D. Bortoluzzi, J. W. Conklin, I. Köker, C. G. Marirrodriga, P. M. Nellen, and S. Vitale. Testing the injection of the LISA-Pathfinder test mass into geodesic conditions. *15th ESMATS proc., Noordwijk*, 2013.

[45] M. Benedetti, D. Bortoluzzi, and S. Vitale. A momentum transfer measurement technique between contacting free-falling bodies in the presence of adhesion. *Journal of Applied Mechanics*, 75(1), 2008.

[46] D. Bortoluzzi, M. De Cecco, S. Vitale, and M. Benedetti. Dynamic measurements of impulses generated by the separation of adhered bodies under near-zero gravity conditions. *Experimental Mechanics*, 48(6):777–787, 2008.

[47] D. Bortoluzzi, L. Baglivo, M. Benedetti, F. Biral, P. Bosetti, A. Cavalleri, M. Da Lio, et al. LISA Pathfinder test mass injection in geodesic motion: status of the on-ground testing. *Classical and Quantum Gravity*, 26(9):094011, 2009.

[48] M. De Cecco, D. Bortoluzzi, L. Baglivo, M. Benedetti, and M. Da Lio. Measurement of the momentum transferred between contacting bodies during the LISA test-mass release phase—uncertainty estimation. *Measurement Science and Technology*, 20(5):055101, 2009.

[49] D. Bortoluzzi, M. Benedetti, L. Baglivo, and S. Vitale. A new perspective in adhesion science and technology: testing dynamic failure of adhesive junctions for space applications. *Experimental Mechanics*, 50(8):1213–1223, 2010.

[50] M. Benedetti, D. Bortoluzzi, L. Baglivo, and S. Vitale. An optimal two-input approach for impulse measurements in the nanon·s range produced by contact forces. *Mechanical Systems and Signal Processing*, 25(5):1646–1660, 2011.

[51] C. Zanoni, D. Bortoluzzi, J. W. Conklin, I. Köker, B. Seutchat, and S. Vitale. Summary of the results of the LISA-Pathfinder test mass release. *Journal of Physics: Conference Series*, 610(1):012022, 2015.

[52] D. Bortoluzzi, C. Zanoni, and J. W. Conklin. On-ground testing of the role of adhesion in the LISA-Pathfinder test mass injection phase. *Advances in Space Research*, 59(10):2572–2582, 2017.

[53] M. Benedetti, D. Bortoluzzi, P. Bosetti, M. Da Lio, and V. Fontanari. The role of adhesion and sub-Newton pull-off forces on the test mass release for the LISA experiment. In *World Tribology Congress*, volume 42029, pages 911–912, 2005.

[54] D. Bortoluzzi, M. Benedetti, and J. W. Conklin. Indirect measurement of metallic adhesion force as a function of elongation under dynamic conditions. *Mechanical Systems and Signal Processing*, 38(2):384–398, 2013.

Acknowledgments (Ringraziamenti)

English version (versione Inglese)

Personally, I believe that interpersonal interactions are fundamental in the performance of such an important and long-lasting activity as a PhD, and that these can be basically divided into two types. The first type concerns the strictly technical aspect, directly related to the daily activities carried out in the workplace. The second type concerns the no less important social and emotional aspect, which, although not directly related to work itself, is undoubtedly a fundamental part of daily life without which no work activity could be carried out efficiently.
As a consequence of the above, the people whom I have dealt with and who have supported me during this long journey necessarily fall into one or both of these categories.

I would like to begin my thanks by addressing the people who fall into both categories at the same time, although I would like to point out that there is no order of importance in the following list.
So, let me start by thanking Professor Daniele Bortoluzzi. Professionally, I met Professor Bortoluzzi while studying for my Master's degree in Mechatronics Engineering at the University of Trento. I was immediately struck by the meticulousness and precision with which he taught his courses, so much so that I decided to write my Master's thesis under his supervision. Moreover, it was Professor Bortoluzzi who also directed me towards the PhD, proposing to be my tutor during this course. During my PhD, I got to know Professor Bortoluzzi better, even in contexts that were not strictly related to the professional field. He has been extremely helpful on several occasions when I was faced with choices that put me in difficulty, and I can say without a shadow of a doubt that I would not be where I am now if it were not for him.
Next I would like to thank my former colleague Andrea Zambotti. First of all, his help was fundamental in the first part of my PhD. He taught me a lot about scientific research and was also a mentor for the preparation of the Mechanical Vibrations lessons, a course for which I was assistant lecturer for the following three years. I also had a great time with Andrea outside of work, given our shared passion for a famous film saga.
I would also like to thank my colleague Edoardo Dalla Ricca. When we met, he

was a student whom I had the pleasure of following in the writing of his Master's thesis. He later became a colleague of mine, having enrolled in the PhD course. Our professional and friendly relationship, especially during the pandemic, has helped us both in carrying out our scientific research.
Giacomo Moretti is another person who has contributed to shaping me and whom I feel it is essential to thank. Although he and I shared a workspace for a relatively short period, Giacomo has often been helpful thanks to his vast multidisciplinary knowledge. I see him as a mentor, given his dedication to research and his amazing ability to solve engineering problems of different kinds. I also had the pleasure of living in Giacomo's flat while I was looking for long-term accommodation, and it was there that we discovered our common passion for the piano.

Among the people who fall into the purely professional category, I would like to thank the members of OHB Italia, in particular Paolo Sarra and Andrea Moroni, for their valuable support in interpreting the LISA Pathfinder mission documentation.
I would also like to thank Professor Wiliam Joseph Weber, and the other members of TIFPA at the University of Trento. Professor Weber has been helpful to me several times, especially in questions related to the capacitive measurement of the GRS.
Sincere thanks are also due to Valerio Ferroni, who made it possible to develop the FEM model to simulate the discharge curves of the test mass. With Valerio, although the lockdown did not allow us to meet in person, I am carrying out work that I am proud of.
I would like to thank Professor John W. Conklin of the University of Florida. My collaboration with Professor Conklin was very short, as the global situation this past year prevented me from travelling to America to work directly with him. However, I still hope to visit his laboratory in the future.
I would like to thank Jacopo Antonini, for his collaboration on the characterization of the impacts affecting the test masses of LISA Pathfinder at the release.
Two other people who have been indispensable thanks to their expertise and willingness to help have been Carlo Zanoni and Jose Mendes, whom I would like to thank for their support.

Thank must also go to all the people who, although they have not contributed directly to my journey, have been fundamental to its success thanks to the emotional bond that unites us.
Firstly, my parents Flavio and Vincenza, my sister Anna and my brother Leonardo. To them I simply say the most spontaneous and sincere thanks, for the continuous and constant support they have given me over the years.
I am also grateful to the rest of my large family, my grandparents Aldo and Corrado and my grandmothers Elsa and Giuseppina. Of course, the family also includes all my uncles, aunts and cousins. Many thanks to everyone.
Then there are the unfailing thanks to my long-standing friends Alberto, Antonio, Carlo C., Carlo G., Emiliano, Francesco, Francisco, Filippo, Giorgio, Marco, Matteo and Nicola. You were, are and will always be a shoulder to lean on.
I would also like to thank the friends I met here in Trento, namely Aurora, Eleonora, Emilio, Giulia, Giuseppe, Lorenzo, Marco, Nicolangelo and Stefano, followed by two

special people, Gemma and Vittorio.
Obviously, all my colleagues and ex-colleagues in the office also deserve due thanks, as they have shared this (sometimes) difficult path with me.
Among the people with whom I have shared most of my experiences here in Trento, and who deserve to be thanked for this, are my room mates (past and present), in particular Alessandro, Andrea F., Andrea G., Antonio, Damiano, Gabriele and Luca.
To an important person in my life, Elisa, I dedicate special thanks.

Finally, I would like to conclude by mentioning the companies/institutes that supported the different phases of this work. Much of the main research reported in this work was supported and/or made possible thanks to ESA (European Space Agency), ASI (Italian Space Agency), INFN (National Institute of Nuclear Physics), OHB Italia, Thales Alenia Space and Airbus Defence and Space (Friedrichshafen, Germany).

Davide Vignotto

Versione Italiana (Italian version)

Personalmente, ritengo che nello svolgimento di una attività importante ed estesa nel tempo qual è il Dottorato di Ricerca siano fondamentali le interazioni interpersonali e che queste possano dividersi sostanzialmente in due tipologie. La prima tipologia riguarda l'aspetto strettamente tecnico, direttamente collegato con le attività svolte quotidianamente sul luogo di lavoro. La seconda tipologia riguarda il non meno importante aspetto sociale e affettivo, che, sebbene non sia direttamente collegato al lavoro in sé, è indubbiamente una parte fondamentale nella vita quotidiana in assenza della quale non sarebbe possibile svolgere in modo efficiente alcuna attività lavorativa.
In conseguenza di quanto esposto, le persone con le quali mi sono confrontato e che mi hanno supportato durante questo lungo percorso ricadono forzatamente in una o in entrambe queste categorie.

Desidero iniziare i miei ringraziamenti rivolgendomi alle persone che rientrano contemporaneamente in entrambe le categorie anche se tengo a precisare che non vi è alcun ordine di importanza nell'elenco seguente.
Dunque, parto dal ringraziare il Professor Daniele Bortoluzzi. Professionalmente, ho conosciuto il Professor Bortoluzzi durante gli studi di Laurea Magistrale in Ingegneria Meccatronica all'università di Trento. Sin da subito mi hanno colpito la meticolosità e la precisione con le quali impartiva le lezioni dei suoi corsi, tant'è che ho deciso di scrivere sotto la sua supervisione la mia tesi di Laurea Magistrale. Inoltre, è stato sempre il Professor Bortoluzzi ad indirizzarmi verso il Dottorato di Ricerca, proponendomi di essere il mio Tutor durante questo percorso. Proprio durante il Dottorato, ho potuto conoscere più a fondo il Professor Bortoluzzi anche in contesti non strettamente legati all'ambito professionale. Più volte mi è stato di estremo aiuto di fronte a scelte che mi mettevano in difficoltà e posso dire senza ombra di dubbio che non sarei dove sono ora se non fosse per lui.

Proseguo con il ringraziare il mio ex-collega Andrea Zambotti. Innanzitutto, il suo aiuto è stato fondamentale nella prima parte del mio Dottorato. Lui mi ha insegnato molto riguardo alla ricerca scientifica ed è stato un mentore anche per quanto riguarda la preparazione delle lezioni di Mechanical Vibrations, corso di cui sono poi stato assistente esercitatore per i tre anni seguenti. Con Andrea ho passato dei bei momenti anche al di fuori dell'ambito lavorativo, vista la passione per una famosa saga cinematografica che ci accomuna.
Sento di dover ringraziare anche il mio collega Edoardo Dalla Ricca. Ci siamo conosciuti quando ho avuto il piacere di seguirlo nella scrittura della sua tesi di Laurea Magistrale ed in seguito è diventato un mio collega, essendosi iscritto al corso Dottorato. Con lui ho fin da subito avuto un rapporto sia professionale che di amicizia. Mi sento di dire che questo rapporto ha aiutato entrambi nel portare avanti la nostra ricerca scientifica.
Giacomo Moretti è un'altra persona che ha contribuito a formare la mia persona e che ritengo indispensabile ringraziare. Sebbene io e lui abbiamo condiviso lo spazio lavorativo per un periodo relativamente breve, Giacomo è stato spesse volte di aiuto grazie alla sua vastissima conoscenza multidisciplinare. Posso dire che lo vedo come un mentore, vista la sua dedizione all'attività di ricerca e la sua strabiliante abilità di risolvere problemi ingegneristici di diversa natura. Ho anche avuto il piacere di vivere nell'appartamento di Giacomo mentre cercavo una sistemazione a lungo termine, ed è lì che abbiamo scoperto la comune passione per il pianoforte.

Tra le persone che rientrano nella categoria legata all'ambito puramente professionale, desidero ringraziare i membri dell'azienda OHB Italia, in particolare Paolo Sarra e Andrea Moroni, per il loro prezioso supporto nell'interpretazione della documentazione della missione LISA Pathfinder.
Ringrazio inoltre il Professor Wiliam Joseph Weber, e gli altri membri del TIFPA dell'Università di Trento. Il Professor Weber mi è stato diverse volte di aiuto, soprattutto nelle questioni relative alla misura capacitiva del GRS.
Anche Valerio Ferroni rientra tra le persone che ringrazio vivamente. Infatti, il modello FEM per simulare le curve di scarica della massa di prova è frutto di una collaborazione con lui. Con Valerio, nonostante il lockdown non ci abbia permesso di incontrarci di persona, sto portando avanti un lavoro di cui vado fiero.
Sento di dover ringraziare il Professor John W. Conklin, dell'University of Florida. La mia collaborazione con il Professor Conklin è stata molto breve, questo a causa della situazione globale di quest'ultimo anno, che mi ha impedito di trasferirmi in America per lavorare direttamente con lui. Tuttavia, conservo la speranza di poter visitare il suo laboratorio in futuro.
Ringrazio Jacopo Antonini, per l'aiuto che mi sta dando nel formalizzare la sua tesi di Laurea Magistrale con l'obiettivo di pubblicare un lavoro in merito alla caratterizzazione degli urti subiti al rilascio dalla massa di prova in LISA Pathfinder.
Altre due persone che sono state indispensabili grazie alla loro competenza e disponibilità sono state Carlo Zanoni e Jose Mendes, che desidero ringraziare per il supporto fornitomi.

In seguito, proseguo ringraziando tutte le persone che, pur non avendo contribuito direttamente a questo mio percorso, sono state fondamentali per la sua riuscita

grazie al legame affettivo che ci unisce.
Comincio quindi con i miei genitori Flavio e Vincenza, mia sorella Anna e mio fratello Leonardo. A loro dico semplicemente il più spontaneo e sincero grazie, per il supporto continuo e costante che hanno saputo darmi in questi anni.
Proseguo con il ringraziare il resto della mia numerosa famiglia, i miei nonni Aldo e Corrado e le mie nonne Elsa e Giuseppina. La famiglia comprende ovviamente anche tutti gli zii, le zie, i cugini e le cugine. Grazie di cuore a tutti.
Seguono gli immancabili ringraziamenti ai miei amici di infanzia/gioventù Alberto, Antonio, Carlo C., Carlo G., Emiliano, Francesco, Francisco, Filippo, Giorgio, Marco, Matteo e Nicola. Eravate, siete e sarete sempre delle spalle su cui contare.
Desidero anche ringraziare gli amici che ho conosciuto qui a Trento, ovvero Aurora, Eleonora, Emilio, Giulia, Giuseppe, Lorenzo, Marco, Nicolangelo e Stefano, seguiti da due persone speciali, Gemma e Vittorio.
Ovviamente, anche tutti i numerosi miei colleghi ed ex-colleghi di ufficio meritano un doveroso ringraziamento, poiché hanno condiviso con me questo percorso, a volte impervio come ben sanno.
Tra le persone con cui ho condiviso la maggior parte delle mie esperienze qui a Trento, e che per questo meritano di essere ringraziate, ci sono i miei coinquilini (passati e presenti), in particolare Alessandro, Andrea F., Andrea G., Antonio, Damiano, Gabriele e Luca.
Ad una persona importante nella mia vita, Elisa, dedico un ringraziamento speciale.

Infine, concludo menzionando le aziende/istituti che hanno supportato le diverse fasi di questo lavoro. Buona parte della ricerca principale riportata in questo lavoro è stata supportata e/o resa possibile grazie all'ESA (European Space Agency), all'ASI (Agenzia Spaziale Italiana), all'INFN (Istituto Nazionale di Fisica Nucleare), ad OHB Italia, a Thales Alenia Space e ad Airbus Defence and Space (Friedrichshafen, Germania).

Davide Vignotto